

**Interfacing Light and a Single Quantum
System with a Lens**

Tey Meng Khoon

A THESIS SUBMITTED FOR THE DEGREE OF PhD

**DEPARTMENT OF PHYSICS
NATIONAL UNIVERSITY OF SINGAPORE**

**SINGAPORE
2008**

Acknowledgements

Special thanks goes first and foremost to Christian Kurtsiefer, my research advisor, who taught me everything from atomic physics, electronics, to milling and lathing, not forgetting the good food and beer he always bought us.

Thanks to Gleb Maslennikov, a great friend who never failed to lend his support through my Phd years. From sniffing toluene and watching deaths of semiconductor quantum dots to measuring the extinction of light by a single atom, he has always been a great partner despite the fact that he did throw a clean vacuum chamber into the workshop dustbin.

Thanks also to Syed Abdullah Aljunid who has always been a great helping hand in our single atom experiment. He is the most easy-going and patient person I have ever met. Many thanks to Brenda Chng for taking pains to proof-read my thesis, Zilong Chen for his contributions during the earlier phase of the single atom experiment and Florian Huber for educating me on numerical integrations. It is my honour and pleasure to be able to work together with them.

Special thanks to Prof. Oh Choo Hiap for agreeing to be my temporary scientific advisor before Christian joined NUS, and to Prof. Sergei Kulik from Lomonosov Moscow State University whom I have the privilege to work with before I started the quantum dot experiment.

I would also like to express my gratitude to Mr. Koo Chee Keong from the Electrical & Computer Engineering Department for helping us with focused-ion-beam milling. He spent a lot of effort and time on our samples even after a few failures due to our mistakes, expecting nothing in return and declining our gratitude in the form of a bottle of wine.

Thanks also goes to Keith Phua from the Science Dean's office who gave

me the access to a multi-processor computer farm. Many thanks to Dr. Han Ming Yong from Institute of Materials Research & Engineering, and Dr. Zheng Yuangang from the Institute of Bioengineering and Nanotechnology for providing us with quantum dot samples.

Of course, there are many more people who have helped make all this possible: Chin Pei Pei, our procurement manager; Loh Huanqian, for her kind words and encouragement; the machine workshop guys, for their unfailing help; the cleaning lady who used to mop my office, and who kept asking me when I would finish my phd... It is simply not possible to name all. Thank you!

Last but not least, thanks goes to many scientists with whom I have the pleasure of working with, namely: Antia Lamas-Linares, Alexander Ling, Ivan Marcikic, Valerio Scarani, Alexander Zhukov, Liang Yeong Cherng, Poh Hou Shun, Ng Tien Tjue, Patrick Mai, Matthew Peloso, Caleb Ho, Ilja Gerhardt, and Murray Barrett.

Contents

Acknowledgements	i
Summary	vi
1 Introduction	1
2 Investigation of single colloidal semiconductor quantum dots	5
2.1 Introduction to colloidal QDs	6
2.2 Energy structure of CdSe QDs	8
2.2.1 Electron-hole pair in an infinitely-deep 'crystal' potential well	9
2.2.2 Confinement-induced band-mixing	13
2.2.3 Emission properties of CdSe QDs	14
2.2.4 Multiple excitons and Auger relaxation	18
2.3 Experiments on bulk colloidal QDs	18
2.3.1 Spontaneous decay rates of colloidal QDs	18
2.3.2 Absorption cross sections of CdSe QDs	21
2.4 Experiments on single colloidal QDs	23
2.4.1 Confocal microscope setup	23
2.4.2 Sample preparation	26
2.4.3 Observing single quantum dot	27
2.4.4 Estimation of absorption cross section by observing a single QD	28
2.4.5 Fluorescence from a single QD	31
2.4.6 The $g^{(2)}(\tau)$ function	32

2.5	Conclusion	33
3	Interaction of focused light with a two-level system	35
3.1	Interaction strength	36
3.2	Interaction of a focused radiation with a two-level system . . .	38
3.2.1	Reverse process of spontaneous emission	39
3.2.2	Scattering cross section	40
3.2.3	Scattering probability from first principles	41
3.3	Calculation of field after an ideal lens	43
3.3.1	Cylindrical symmetry modes	43
3.3.2	Focusing with an ideal lens	45
3.3.3	Focusing field compatible with Maxwell equations . . .	49
3.3.4	Field at the focus	51
3.3.5	Obtaining the field at the focus using the Green theorem	55
3.4	Scattering Probability	56
3.5	Conclusion	59
4	Strong interaction of light with a single trapped atom	60
4.1	Setup for extinction measurement	62
4.2	Technical details of the setup	64
4.3	Trapping a single atom	71
4.4	Influence of external fields on the trapped atom	74
4.5	Measuring the transmission	76
4.6	Results	79
4.7	Losses and interference artefacts	81
4.8	Comparison with theoretical models	83
4.9	Conclusion	87
5	Outlook and open questions	88
A		91
A.1	A two-level system in monochromatic radiation	91
A.2	Numerical Integration of κ_μ	95
A.3	Energy levels of the ^{87}Rb atom	98

A.4	The D1 and D2 transition hyperfine structure of the ^{87}Rb atom	99
A.5	AC Stark shift	100
A.6	Measuring the oscillator strengths of the Rubidium atom . . .	103
A.7	Effects of atomic motion on the scattering probability	105
A.8	Setup photos	108
A.9	Band gaps of various semiconductors	109
A.10	Conservation of energy	110

Bibliography		113
---------------------	--	------------

Summary

We investigate both experimentally and theoretically the interaction of a quantum system with a coherent focused light beam. The strength of this interaction will determine the viability of implementing several quantum information protocols such as photonic phase gates and quantum information transfer from a ‘flying’ photon to a stationary quantum system. We started with the investigation of colloidal semiconductor nanocrystals (or quantum dots (QDs)) such as CdSe/ZnS, CdTe/ZnS, and InGaP/ZnS. We set up a confocal microscope to observe the optical properties of individual QDs at room temperature. Our measurements showed that these QDs have absorption cross sections about a million times smaller than that of an ideal two-level system, indicating that this physical system can only interact weakly with light. The most deterring property of colloidal QDs is that they are chemically unstable under optical excitation. The QDs were irreversibly bleached within a few seconds to a few hours in all our experiments. The short coherent time and low absorption cross section of these QDs render them difficult candidate for storage of quantum information.

The second quantum system we investigated was the Rubidium alkaline atoms having a simple hydrogen-like energy structure. We set up a far-off-resonant optical dipole trap using a 980 nm light to localize a single ^{87}Rb atom. The trapped atom is optically cooled to a temperature of $\sim 100 \mu\text{K}$, and optically pumped into a two-level cycling transition. Under these conditions, the atom can interact strongly with weak coherent light tightly focused by a lens. We quantified the atom-light interaction strength by measuring the extinction of probing light by a single ^{87}Rb atom. The measured extinction sets a lower bound to the percentage of light scattered

by the single atom (scattering probability). A maximal extinction of 10.4% has been observed for the strongest focusing achievable with our lens system. Our experiment thus conclusively shows that strong interaction between a single atom and light focused by a lens is achievable.

We also performed a theoretical study of the scattering probability by computing the field at the focus of an ideal lens, and thereby obtaining the power scattered by a two-level system localized at the focus. Our calculations were based on a paper by van Enk and Kimble [1] except that we dropped two approximations used in their original model, making the model applicable to strongly focused light. The predictions of our model agree reasonably well with our experimental results. In contrary to the conclusion of the original paper, our results show that very high interaction strength can be achieved by focusing light onto a two-level system with a lens.

Chapter 1

Introduction

The past two decades have witnessed the emergence of the quantum information science (QIS), which is a synthesis of quantum physics, information theory, and computer science. It was recognized very early since the establishment of quantum theory about 80 years ago that information encoded in quantum systems has weird and counterintuitive properties. However, the systematic study of quantum information has only become more active recently due to a deeper understanding of classical information, coding, cryptography, and computational complexity acquired in the past few decades, and the development of sophisticated new laboratory techniques for manipulating and monitoring the behavior of single quanta in atomic, electronic, and nuclear systems [2, 3].

While today's digital computer processes classical information encoded in bits, a quantum computer processes information encoded in quantum bits, or *qubits*. A qubit is a quantum system that can exist in a coherent superposition of two distinguishable states. The two distinguishable states might be, for example, internal electronic states of an individual atom, polarization states of a single photon, or spin states of an atomic nucleus [3]. Another special property of quantum information is *entanglement*. Entanglement is a quantum correlation having no classical equivalent, and can be roughly described by saying that two systems are entangled when their joint state is more definite and less random than the state of either system by itself

[2, 3, 4, 5]. These special properties of quantum information bestow upon a quantum computer abilities to perform tasks that would be very difficult or impossible in a classical world. For examples, Peter Shor [6] discovered that a quantum computer can factor an integer exponentially faster than a classical computer. Shor's algorithm is important because it breaks a widely used public-key cryptography scheme known as RSA, whose security is based on the assumption that factoring large numbers is computationally infeasible. Another potential capability of a quantum computer is to simulate the evolution of quantum many-body systems and quantum field theories that cannot be performed on classical computers without making unjustified approximations.

Currently, a number of quantum systems are being investigated as potential candidates for quantum computing. They include trapped ions [7, 8], neutral atoms [9], photons [10, 11], cavity quantum electrodynamics (CQED) [12], superconducting qubits [13], color centers in diamond [14], semiconductor nanocrystals [15, 16], etc. Analogous to classical information processing, any quantum system used for quantum information processing must allow efficient state initialization, manipulation and measurement with high fidelity, and efficient operation by a quantum gate [17]. Some of the above listed candidates have already fulfilled these requirements, but none have overcome the obstacle of scalability for constructing a useful quantum computer.

One of the proposals to scale up a quantum information processing system is by constructing a quantum network, in which each qubit stores information and is manipulated locally at a node on the network, and quantum information is transferred from one node to another at a distant location [18, 19, 20]. However, transferring quantum information with high fidelity is a non-trivial task. Unlike classical information, quantum information cannot be read and copied without being disturbed. This property is called the non-cloning theorem of quantum information, which follows from the fact that all quantum operations must be unitary linear transformations on the state [21]. Therefore, one cannot measure a qubit, and transfer the measured information classically to another qubit. Instead, the transfer of quantum information requires (i) interaction between the information-sending quantum

system with an auxiliary quantum system (messenger), (ii) transportation of the messenger to the information-receiving quantum system, and (iii) interaction between the messenger with the receiver. Furthermore, to ensure efficient information transfer, every step in the information transfer process must be carried out with high fidelity and low loss.

For quantum information transfer, photons are usually adopted as the messenger due to its robustness in preserving quantum information over long distances [18, 19, 20]. The requirement of lossless information transfer implies that a messenger photon must be absorbed by the receiver with a probability close to unity. A common approach to enhance the absorption probability of a photon by a quantum system is by placing the quantum system in a high finesse cavity [22, 23, 24, 25].

Here, instead of a cavity, we employ a different approach. We attempt to answer the question whether high absorption probability is achievable by focusing a photon onto a quantum system with a lens. The reason for asking such a question is twofold. First, it is not always possible to place a high finesse cavity around a quantum system. In the few cases where it is possible, ensuring that every cavity on the network is locked to the same frequency can be resource demanding. A lens system, on the other hand, is much simpler to setup. Second, it is of fundamental interests to find the maximum achievable absorption probability by focusing light onto a single quantum system, especially since there are opposing opinions in the community on the feasibility of such a scheme.

As a first step toward the answer, we started by studying the absorption probability of weak *coherent* light by single quantum systems instead of preparing real single photon pulses. Our first attempt was carried out on colloidal semiconductor quantum dots at room temperature. We observed that these quantum dots have very small absorption cross sections compared to an atom, and they are photo-chemically unstable. For these reasons, we switched our focus to a cleaner quantum system – ^{87}Rb atoms. With this system, we showed experimentally that strong atom-light interaction can be achieved by simply focusing light to an atom.

The layout of this dissertation is organized in the following manner.

Chapter 2 reports our investigation on individual colloidal semiconductor nanocrystals (CdSe, CdTe, etc) at room temperature. Chapter 3 gives a theoretical overview of the interaction strength between a focused coherent light field and a two-level system in free space. Chapter 4 presents an experiment in which we measured the extinction of a light beam due to a single trapped ^{87}Rb atom. In this experiment, we optically pump the ^{87}Rb atom into a two-level cycling transition and measured an extinction of more than 10%. In fact, such a high extinction violates the predictions by S. J. van Enk and H. J. Kimble [1], who suggested that absorption of light by a single atom in free space would not be efficient. We later realized that approximations made in their original work greatly underestimated the potential of such a coupling scheme. An extension of their model was subsequently performed (Chapter 3). Our new model explains our experimental results reasonably well and suggests the possibility of achieving much higher interaction strength than what we currently observe. The results of this study are published in [26, 27].

Chapter 2

Investigation of single colloidal semiconductor quantum dots

A number of quantum systems have been identified as potential candidates for future quantum information processing. They include ions [7, 8], cavity quantum electrodynamic systems [12], nuclear magnetic resonance ¹ [28], photons [10, 11], superconducting quantum bits [29], semiconductor QDs [16], etc. Among these, the solid state system has the advantage of allowing one to tap into the resource and technology of the solid-state fabrication industry. It has been speculated that a scalable, and economically feasible quantum computing device will be created with a solid-state system. Despite the fact that one has less control over semiconductor QDs compared other quantum systems due to its stronger coupling to the environment and more complicated energy structure, many groups are pursuing research on QDs in the hope of taming these dots for use in quantum computation.

This chapter documents our efforts to characterize single colloidal semiconductor quantum dots (QDs) (CdSe/ZnS, CdTe/ZnS) at room temperature for the purpose of quantum information processing. The main aim is to measure the absorption cross section of a single QD at room temperature so as to quantify the interaction strength between light and a single QD. We set up

¹Braunstein et al. showed that there was no quantum entanglement in any bulk NMR experiment, implying that the NMR device is at best a classical simulator of a quantum computer.

a confocal microscope to observe the fluorescence from single colloidal QDs embedded in a transparent matrix. We observed clear photon-antibunching effect in the fluorescence, showing that a single QD can be used as a single photon source. However, the dense energy levels of colloidal QDs and their strong coupling to phonons lead to a very short quantum-state coherence time of picoseconds. Our measurements show that the absorption cross sections of these dots are a million times smaller than that of a simple two-level system exposed to a weak resonant field. The fluorescence quenching effects and the chemical instability of colloidal QDs under photoexcitation will also be discussed.

2.1 Introduction to colloidal QDs

A semiconductor nanocrystal is a nanoscale crystalline particle that is characterized by the same crystal lattice structure as the corresponding bulk semiconductor. Due to the small size of the system, the charge carriers within a nanocrystal experience strong quantum confinement effect, resulting in a discrete energy structure similar to that of an atom. Therefore, such a system is also called a quantum dot. One way of growing semiconductor QDs is by using molecular beam epitaxy where the QDs are embedded in a bulk semiconductor. Another way uses wet chemical synthesis [30, 31, 32, 33, 34], resulting in colloidal QDs soluble in various solvents. Our study focuses on the commercially available colloidal heterostructure QDs.

Figure 2.1(i) shows the typical structure of a colloidal heterostructure semiconductor QD. Such QDs are made up of a core nanocrystal which is passivated by a shell of a different semiconductor, and a coating of organic molecules that enables the QDs to dissolve in the solvent. The core typically consists of 100 to 10,000 atoms. It is generally made up of a semiconductor with a direct band gap in order to enhance the quantum yield ² of the dots. Among the large varieties of semiconductors, only a few semiconductors like

²The quantum yield of a QD is defined as the probability that the decay of an exciton in the QD is carried out by emission of a photon.

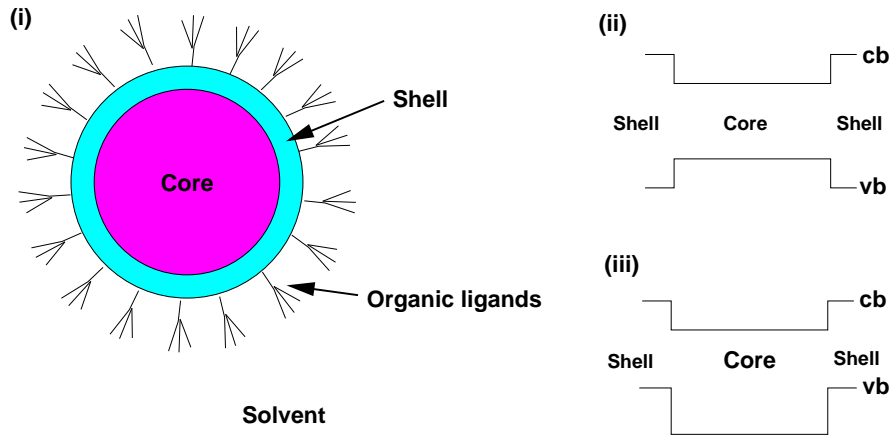


Figure 2.1: (i) A typical heterostructure colloidal quantum dot in a solvent. (ii) and (iii): Plots of the bottom of the conduction band (cb) and the top of the valence band (vb) versus the cross-section of the type I (ii) and type II (iii) heterostructure QDs.

CdSe, CdTe, InP, GaAs, etc., have band-gap transitions in the near infrared to visible regime where efficient detectors, light sources and optics are readily available (see Appendix A.9 for the band gaps of various semiconductors).

As QDs have a very large surface-to-volume ratio, their optical and structural properties are strongly influenced by the properties of their surface. Passivating the core nanocrystal with a few monolayers of a second semiconductor can greatly enhance the quantum yield and the chemical stability of the QD [31, 32, 35, 36, 37]. To maintain the chemical stability of colloidal QDs and ensure that they do not aggregate or disintegrate in the solvent, certain organic ligands are dissolved in copious amount in the solvent. The functions of such ligands are twofold. One end the ligands passivates the dangling bonds of the shell, making the shell more stable. The other end of the ligands has functional groups that are attractive to the solvent, enabling the QDs to be soluble. These organic ligands can also influence the optical properties of the QDs significantly, signaling the strong coupling of quantum dots to its environment.

Heterostructure QDs are classified into two types. Figure 2.1(ii)/(iii) shows the spatial variations of the bottom of the conduction band and the

top of the valence band in a type-I/type-II heterostructure QD. In type-I heterostructure QD, both the excited electrons and holes are confined within the core rather than in the shell, thereby leading to stronger exchange interaction³ between the two charges compared to the type-II QDs. For the particular type-II band structure shown in Fig. 2.1(iii), the excited electrons would be confined within the core but the holes would be confined within the shell. The spatial separation of electron and hole, which is a fundamental feature of type-II QDs, leads to longer radiative lifetimes, lower exciton binding energy and unusual dynamic and recombination properties of charge carriers as compared to type-I QDs [38, 39, 40]. Therefore, type-I QDs are expected to be more suitable for quantum information processing where efficient interaction between light and the quantum system is essential.

The colloidal QDs we have investigated include toluene soluble (core/shell) CdSe/ZnS, CdTe/ZnS QDs capped by trioctylphosphine oxide (TOPO), and water soluble CdTe QD capped by glutathione [41]⁴. These colloidal dots can be fabricated with very high quality. They are almost spherical, and have a wurtzite (hexagonal) lattice structure. Their diameters can be varied from 12 to 110 Å with very narrow diameter distribution (< 5% rms) within each sample [30].

2.2 Energy structure of CdSe QDs

Much experimental and theoretical effort has been spent in the past few decades to understand the energy structure of various semiconductor QDs. CdSe is one of the most well understood semiconductor nanocrystals because these dots can be fabricated in various sizes with high quality [30]. This section summarizes the main electronic and optical properties of the CdSe QDs. The models presented here represent the results of a large number

³The exchange interaction between two quantum objects is proportional to the overlap of the their wavefunctions.

⁴The core/shell QDs were obtained from Evident Technologies, Inc. The glutathione-capped CdTe QDs were kindly provided by Dr. Yuangang Zheng from the Institute of Bioengineering and Nanotechnology, Singapore.

of experimental and theoretical studies performed over the past 30 years. Therefore, it is not possible to go into detailed descriptions of experimental evidences for every property stated herein. Two excellent reviews on the energy structure of CdSe QDs are provided by Norris et al. [42] and Klimov [43].

2.2.1 Electron-hole pair in an infinitely-deep 'crystal' potential well

In a bulk semiconductor, absorption of a photon promotes an electron to the conduction band and leaves a hole in the valence band. The electron and the hole form an exciton which is a hydrogen-like system with a Bohr radius a_{exc} ($a_{\text{exc}} = 5.6$ nm for CdSe). If the mean nanocrystal radius \bar{a} is greater than $3a_{\text{exc}}$, one is in the weak-confinement regime [44]: the confinement kinetic energy is smaller than the Coulomb interaction energy between the electron and the hole, and the Wannier exciton is confined as a whole. When \bar{a} is a few times smaller than a_{exc} , one is in the strong-confinement regime, in which both carriers are independently confined [45].

One of the simplest Hamiltonians modeling an exciton in a spherical nanocrystal, within the effective mass theory and in the absence of band mixing effect [44], is given by [45, 46, 47]

$$H = \frac{p_e^2}{2m_e} + \frac{p_h^2}{2m_h} - \frac{e^2}{4\pi\epsilon|\vec{r}_e - \vec{r}_h|} + V(r_e) + V(r_h). \quad (2.1)$$

Here the first two terms describe the kinetic energies of the electron and the hole respectively, where $m_e(m_h)$ represents the effective mass of the electron(hole) [48]; the third term describes the Coulomb interaction between the electron and the hole, where the ϵ is the dielectric constant of the semiconductor; and the last two terms describe a spherical infinite potential well of radius a :

$$V(r_{e(h)}) = \begin{cases} 0 & \text{if } r_{e(h)} \leq a, \\ \infty & \text{if } r_{e(h)} > a. \end{cases} \quad (2.2)$$

If one ignores the Coulomb interaction in the strong confinement regime,

then the electron and hole become two independent particles confined in a spherical infinite potential well (the Coulomb interaction can be considered as a perturbation later). Their energy eigen-wavefunctions are given by [49, 50]

$$\begin{aligned}\Psi_{n,l,m}^{e(h)}(r, \theta, \phi) &= f_{n,l,m}(\vec{r}) u_{e(h)}(\vec{r}) \\ &= [A_{n,l} j_l(k_{n,l}r) Y_l^m(\theta, \phi)] u_{e(h)}(\vec{r}),\end{aligned}\quad (2.3)$$

where $f_{n,l,m}(\vec{r})$ is the envelope function, $u_{e(h)}(\vec{r})$ the cell periodic function of the conduction(valence) band ⁵ [48, 50], $A_{n,l}$ the normalization constant, $Y_l^m(\theta, \phi)$ the spherical harmonics, $j_l(k_{n,l}r)$ the l th order spherical Bessel function, and

$$k_{n,l} = \frac{\alpha_{n,l}}{a} \quad (2.4)$$

with $\alpha_{n,l}$ the n th zero of j_l . The eigen-energies of the electron are given by

$$E_{n,l}^e = \frac{E_g}{2} + \frac{\hbar^2 \alpha_{n,l}^2}{2m_e a^2}, \quad (2.5)$$

and those of the hole are given by

$$E_{n,l}^h = -\frac{E_g}{2} - \frac{\hbar^2 \alpha_{n,l}^2}{2m_h a^2} \quad (2.6)$$

with E_g being the band gap of the bulk semiconductor. Due to the symmetry of the system, the eigenfunctions of the electron(hole) are labelled by quantum numbers $n(1, 2, 3\dots)$, $l(s, p, d\dots)$, and m , similar to that describing the atomic electronic configurations. Here only the transitions that conserve n and l are dipole-allowed, with an oscillator strength proportional to $(2l+1)$.

Figure 2.2 shows a few lowest energy levels obtained using this simplified model. The model captures the essential facts that the exciton energy in a QD is quantized, and that the transition band gap of a QD increases when

⁵The wavefunction of a particle in a periodic potential satisfies the form $\psi_{n\vec{k}}(\vec{r}) = u_{n\vec{k}}(\vec{r}) \exp(i\vec{k} \cdot \vec{r})$ (Bloch's theorem), where $u_{n\vec{k}}(\vec{r})$ is the cell periodic function, and n the energy-band index. $u_{e(h)}(\vec{r})$ is the cell periodic function of the conduction(valence) band at $\vec{k} = 0$. Here it is assumed that the cell period function has a weak \vec{k} dependence near the bottom(top) of the conduction(valence) band.

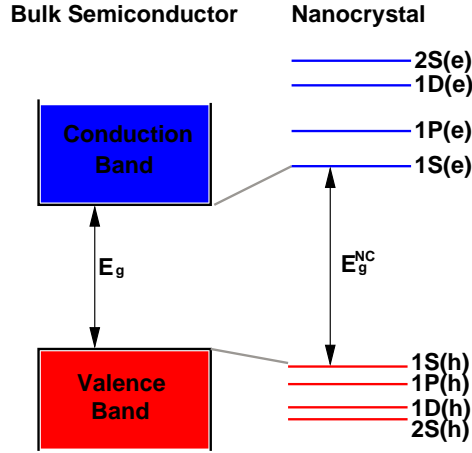


Figure 2.2: Transformation from the continuous conduction and valence bands of the bulk semiconductor to the discrete energy structure in a QD. Using Eqns. 2.5 and 2.6, the band gap of the nanocrystal is related to the band gap of the bulk semiconductor by $E_g^{\text{NC}} = E_g + \pi^2 \hbar^2 / 2m_r a^2$, where $m_r = (m_e^{-1} + m_h^{-1})^{-1}$.

the radius of the QD gets smaller. However, the model overestimates the band gap for smaller nanocrystals [30] and is not able to fully explain the absorption spectra of these dots [51].

There are two major assumptions that go into this model:

1. The wavefunction of the electron(hole) can be expressed as a linear superposition of the conduction(valence)-band Bloch functions [48], and it satisfies the boundary condition imposed by the infinite potential well. This results in the electron(hole) wavefunction being finally expressed as the product of an envelope function $f_{n,l,m}(\vec{r})$, and the cell periodic function $u_{e(h)}$, which is sometimes called the envelope approximation [52]. This assumption should work when the diameter of the dot is much larger than the lattice constant of the material.
2. Only the lowest(highest) conduction(valence) band near $k = 0$ contributes to the lowest(highest) energy levels of the electron(hole) in the QDs. It is further assumed that these bands are twofold degenerate (including spin) and isotropic. As it turns out, these assumptions are not suitable for describing the CdSe crystal. The conduction band of

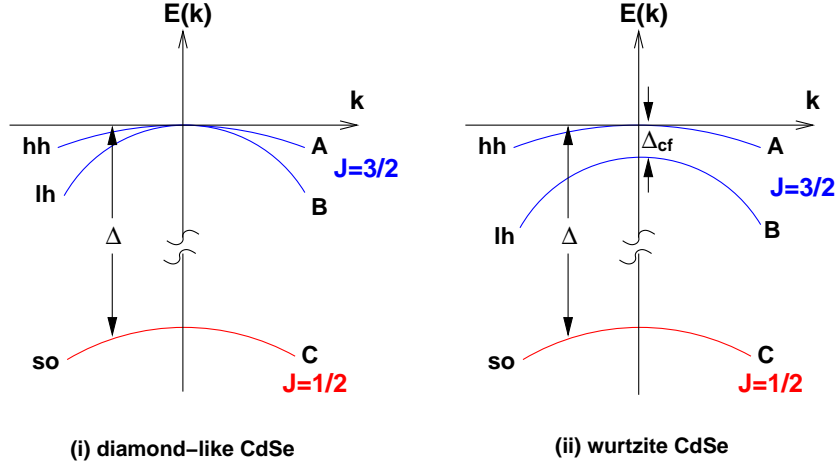


Figure 2.3: Simplified illustration of the valence band structure for (i) diamond-like CdSe and (ii) wurtzite CdSe near $k = 0$. Details of the structure are explained in the text.

CdSe arises from the Cd 5S orbitals and is twofold degenerate at $k = 0$. The valence band, on the other hand, arises from the Se 4p atomic orbitals and has an inherent sixfold degeneracy at $k = 0$. Due to strong spin-orbit coupling (Δ), this degeneracy is split into a fourfold degenerate $J = 3/2$ band and a twofold degenerate $J = 1/2$ split-off (so) band in a diamond-like CdSe, where J denotes the total unit cell angular momentum. Away from $k = 0$ the $J = 3/2$ band splits further into the $J_m = \pm 3/2$ heavy-hole (hh) and $J_m = \pm 1/2$ light-hole (lh) bands, both doubly-degenerate (Fig. 2.3(i)). For a wurtzite CdSe crystal, the degeneracy of the lh and hh band at $k = 0$ is further lifted by the crystal field (Fig. 2.3(ii)). Since the spin-orbit splitting ($\Delta = 0.42$ eV) and the crystal-field splitting ($\Delta_{cf} = 25$ meV) are small compared to the band gap of the CdSe ($E_g = 1.84$ eV at 10 K), all of the three valence bands (hh, lh, and so) must be included in the modeling Hamiltonian in order to explain the absorption spectra of the CdSe dots [44, 49].

2.2.2 Confinement-induced band-mixing

A more accurate model that describes the absorption spectra of CdSe QDs has two main improvements over the previous model:

1. The Hamiltonian modeling the electron still takes the same form as in Eqn. 2.1, but adopts a more realistic spherical finite potential well [44, 50, 51]. Such an improvement is necessary because the effective mass of the electron is much smaller than that of the holes. Adopting an infinite potential well for the electron overestimates the transition band gap for QDs with smaller diameters [53].
2. The hole is modeled using the ‘spherical’ Luttinger’s Hamiltonian ⁶ together with an infinite potential well [44, 49]. The wave functions of the hole is assumed to have the following form:

$$\Psi_h = \sum_{\mu=-3/2}^{3/2} f_{3/2,\mu}(\vec{r})u_{3/2,\mu} + \sum_{\mu=-1/2}^{1/2} f_{1/2,\mu}(\vec{r})u_{1/2,\mu}, \quad (2.7)$$

where $u_{3/2,\mu}$ and $u_{1/2,\mu}$ are the periodic cell functions of the fourfold degenerate (hh, lh) and twofold degenerate (so) valence bands, and $f_{3/2,\mu}$ and $f_{1/2,\mu}$ are their corresponding envelope functions ⁷. The hole states are now characterized by the total angular momentum $\vec{F} = \vec{J} + \vec{L}$, where \vec{J} is the angular momentum of the periodic cell function, and \vec{L} is the orbital angular momentum of the hole envelope function.

The band mixing effect leads to a more complex energy structure of the hole states and a different set of transition selection rules [44] (Fig. 2.4). The new model is able to explain the absorption spectra of the CdSe QDs

⁶For bulk diamond-like semiconductor, the 6-fold degenerate valence band is described by the Luttinger Hamiltonian [54, 55]. This expression, a 6 by 6 matrix, is derived within the context of degenerate $\vec{k} \cdot \vec{p}$ perturbation theory [56]. The Hamiltonian is commonly simplified further using the spherical approximation, in which the terms that have strict cubic symmetry are neglected, saving the term that is spherically symmetric [57, 58].

⁷As CdSe is wurtzite, use of the Luttinger Hamiltonian for CdSe QDs is an approximation. It does not include the crystal field splitting that is present in wurtzite CdSe.

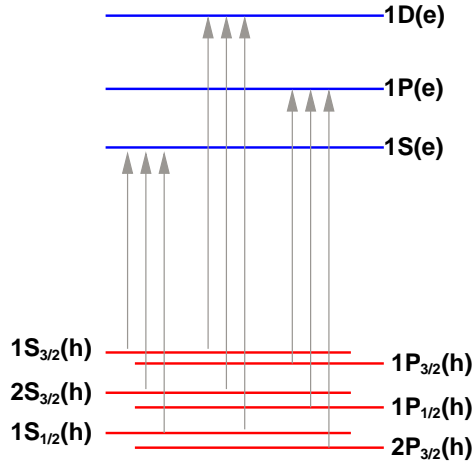


Figure 2.4: Mixing between different valence subbands due to the quantum confinement effect leads to more complex energy structure of the hole states compared to those shown in Fig. 2.2. Arrows indicate dipole-allowed interband transitions.

quantitatively when the electron-hole Coulomb interaction is included as a first order energy correction [44, 51]. The success of the model, i.e. the fact that the quantum state of the charges depends strongly on the band structure of the bulk material, suggests that a nanocrystal inherits much of its properties from the bulk. Although such a result may not be too surprising, it can be undesirable if one would like to use such a system for quantum information processing. This point will become clearer when we further discuss the properties of these dots.

2.2.3 Emission properties of CdSe QDs

The absorption spectrum and the emission spectrum of a CdSe QD are different. The absorption spectrum shows a number of absorption peaks that can be explained well by the model discussed in Section 2.2.2. The emission spectrum, on the other hand, shows none of the absorption features, independent of the excitation light frequency. It only shows an emission peak red shifted from the band edge absorption, together with the bulk longitudinal-optical (LO) phonon replicas of this peak (Fig. 2.5). Such differences are due to the rapid (< 1 ps) decay of the exciton into the photo-emitting states even at

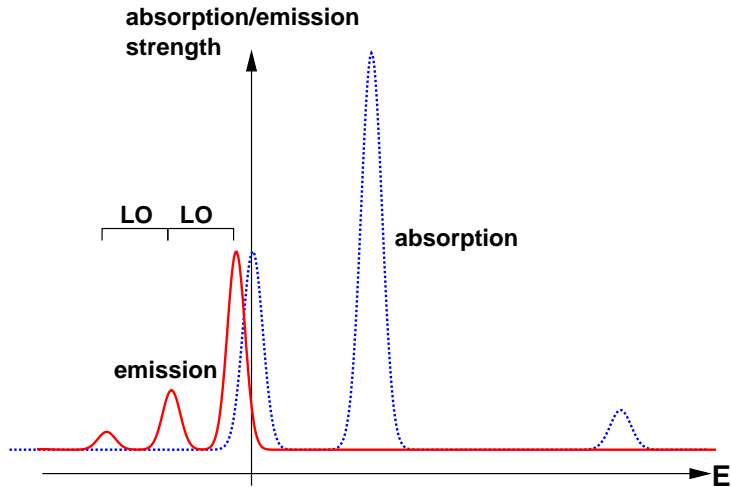


Figure 2.5: Simplified illustration of the emission spectrum of a CdSe QD at liquid He temperatures. The main emission peak is always red shifted from the lowest energy absorption peak. The highest-energy emission peak is separated from other lower-energy emission peaks by integer numbers of the bulk LO phonon's energy (25.4 meV). The LO replicas of the absorption peaks are not shown for simplicity.

liquid He temperatures [59, 60].

The rapid relaxation of a high energy hole to the $1S_{3/2}$ ground state is facilitated by acoustic phonons. This is possible because of the small energy separation among the hole levels. On the other hand, the separation of the lower electron levels are much larger than the energy of the LO phonon, therefore rapid relaxation of a higher lying electron is unexpected. Efros et al. [61] proposed that a higher energy electron can jump to the $1S$ ground state by transferring its energy to the hole using the Coulomb interaction between the charges, a process termed electron-hole Auger collision. Another relaxation route is through the coupling of an excited electron to the nanocrystal's surface states that act as an efficient heat bath. Both explanations were supported by a number of experiments [62, 63, 64].

The origin of the red-shifted emission is more controversial because the luminescence properties of nanocrystals are highly dependent on the sample preparation methods. Some nanocrystals can exhibit a very broad (up to few hundred meV) and strongly red-shifted emission spectrum [65, 66]. The emission states are generally thought to be related to the surface/interface-

related states of the nanocrystals [65, 66]. High quality CdSe nanocrystals, on the other hand, emit with high quantum yield (0.1 to 0.9 at 10 K) near the band edge with a line width of less than a few meV at liquid He temperatures [30, 67, 68] (Fig. 2.5). The fact that the emission peak is accompanied by strong LO phonon replicas suggests that radiative relaxation is dipole-forbidden. Furthermore, the radiative lifetime of CdSe dots is strongly temperature dependent, changing from hundreds of nanoseconds to approximately 1 μ s at liquid He temperatures, to 20 ns at room temperature [69, 70, 71]. The emission properties of the high quality CdSe nanocrystals can be explained by the dark/bright-exciton model [69, 72], which accounts for the splitting of the band-edge exciton produced by the combined effect of the electron-hole exchange interaction and anisotropies associated with the crystal field and non-spherical shape of the nanocrystals.

In the spherical model (Section 2.2.2), the band edge exciton ($1S(e)1S_{3/2}(h)$) is 8-fold degenerate. The degeneracy is broken by the electron-hole exchange interaction. As the exchange interaction is proportional to the overlap between the electron and hole wave functions, it is greatly enhanced, up to tens of meV, in QDs compared with bulk materials. In the presence of the strong exchange interaction, the electron and hole cannot be considered independently and are described by the total angular momentum quantum number N . The 8-fold degenerate band edge exciton is split into a higher energy 3-fold degenerate, optically active, $N = 1$ bright exciton, and a lower energy 5-fold degenerate, optically passive, $N = 2$ dark exciton (Fig. 2.6). These states are further split into five sublevels because of the anisotropy of the wurtzite lattice and the nonspherical nanocrystal shape (CdSe nanocrystals are usually slightly prolate [30]), forming two manifolds of upper (U) and lower (L) substates, which are labeled according the projection of the total exciton angular momentum N along the unique crystal axis, N_m (Fig. 2.6). The lowest-energy state is labelled $N_m = 2$ and is optically passive. It is separated from the next higher energy bright state ($N_m = \pm 1^L$) by ~ 1 meV to more than 10 meV, depending on the size of the nanocrystal [69]. The energy separation, typically referred to as the resonant Stokes shift, can be measured experimentally [73, 74].

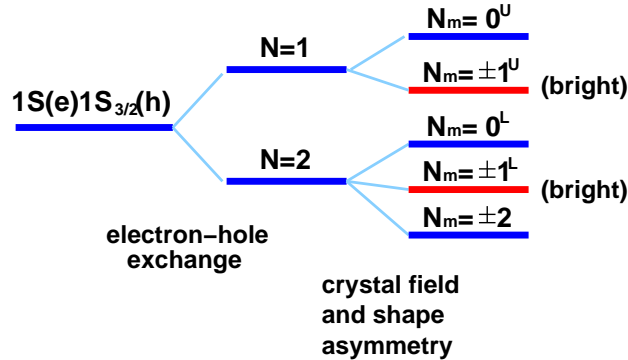


Figure 2.6: Schematic diagram of splitting of band-edge ($1S(e)1S_{3/2}(h)$) exciton in CdSe nanocrystals induced by the electron-hole exchange interaction and anisotropies associated with the crystal field in the hexagonal lattice and nanocrystal shape asymmetry.

The thermal redistribution of excitons between the $N_m = 1^L$ (bright) and $N_m = 2$ (dark) states is the major factor that leads to the strong dependence of the recombination dynamics in CdSe dots on sample temperature. At low temperatures, only the $N_m = 2$ dark state is populated. Therefore the recombination is slow and is typically assisted by the LO phonons. As the temperature increases, the excitons are thermally excited from the dark to the $N_m = 1^L$ bright state, which produces faster recombination. At sufficiently high temperature, the population of the exciton is equally distributed between the bright and the dark states, resulting in a decay lifetime twice the bright-exciton lifetime (~ 20 ns for CdSe nanocrystals).

To summarize, the rapid relaxation of an exciton to the $N_m = 2$ ground state sets an upper limit to the exciton's coherent time of 1 ps in CdSe nanocrystals. Such a short coherent time is undesirable if one is to use the exciton states for the purpose of quantum information processing. In fact, short coherent times pose a problem common to all solid state quantum systems even though they might have a different electronic structure from that of colloidal CdSe nanocrystals. It would be one of the main obstacles to overcome before such system can be used for quantum information processing.

2.2.4 Multiple excitons and Auger relaxation

So far, we have discussed the electronic and optical properties of CdSe nanocrystals under the assumption of a single exciton. This is rather incomplete because many optical properties of these dots are in fact caused by the excitation of multiple excitons.

When there is more than one exciton in a CdSe nanocrystal, the decay of the excitons are dominated by the nonradiative Auger recombination [75, 76]. Auger recombination is a process in which the electron-hole recombination energy is not emitted as a photon but is instead transferred to a third particle (an electron or a hole) that is re-excited to a higher-energy state. The Auger recombination lifetime is shorter than 1 ns in CdSe nanocrystals. It gets shorter when there are more excitons in the nanocrystals [75]. During the multi-exciton Auger recombination process, an energy-receiving electron or hole may be ejected out of the CdSe interior, leaving the QD in an ionized state. When this happens, the QD gets into the “dark” state and it no longer fluoresces. This is because subsequent electron-hole pair excitations of the ionized QD will relax nonradiatively due to efficient three-body Auger recombination [77]. The QDs only returns to the “bright” state when it is neutralized again. Therefore, the fluorescence signal of a single CdSe QD exhibits a blinking effect under light excitation.

2.3 Experiments on bulk colloidal QDs

This section discusses two experiments we performed on bulk colloidal QDs in solution. One experiment measures the spontaneous decay rates of these dots. Another measures the emission spectra and absorption cross sections of these dots.

2.3.1 Spontaneous decay rates of colloidal QDs

Figure 2.7 shows the schematic setup used for measuring the spontaneous decay rate of colloidal QDs in solution. The main idea of the experiment is to excite the QDs with a short (femtosecond) pulse, and to observe the

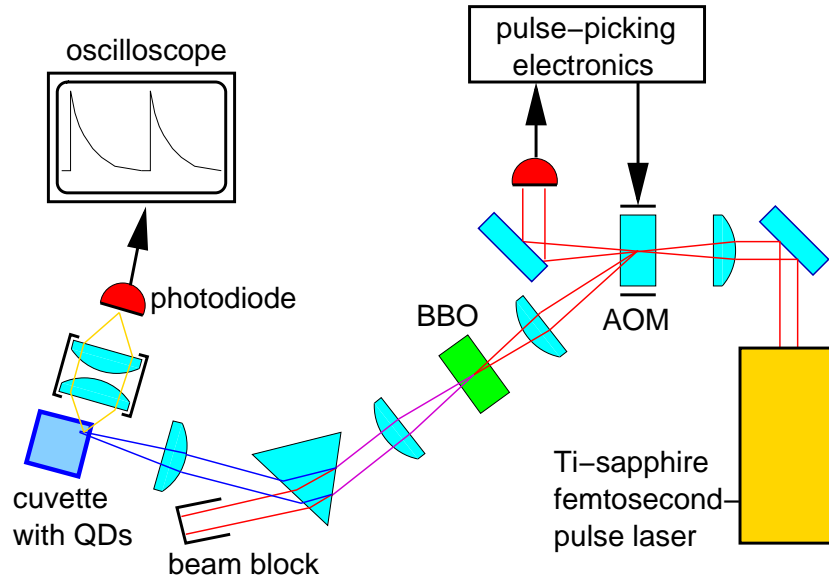


Figure 2.7: Schematic setup for measuring the spontaneous decay rate of QDs in water/toluene. AOM: acousto-optic modulator, BBO: Beta Barium Borate crystal for second harmonic generation.

decay of the QD's fluorescence intensity after the pulse excitation. We use a Ti-sapphire laser that generates light pulses with a width of 120 fs and a center wavelength of 780 nm. Since the original pulse separation (13 ns) is smaller than the spontaneous decay time of the QDs (> 20 ns), we use an acousto-optic modulator (AOM) to pick a pulse out of every M pulses to ensure that the QDs to relax back to their ground states before being excited again by the consecutive pulse. After passing the AOM, the pulses are focused into a BBO (Beta Barium Borate) crystal, where part of the 780 nm light is up-converted to 390 nm light⁸. This up-conversion process is necessary because the QDs we used absorb 390 nm but not 780 nm light⁹. The 390 nm light is then separated from the 780 nm light with a prism, and is focused into a QD solution in a fused-silica cuvette. The fluorescence from the QDs is detected with a fast Si-photodiode¹⁰, whose signal is recorded by

⁸Note that the sequence of AOM to BBO (instead of BBO to AOM) gives a better on/off ratio for the picked pulses due to the nonlinearity of the frequency doubling process.

⁹CdSe QDs have a band gap larger than 1.73 eV (Appendix A.9).

¹⁰Hamamatsu S5973 (cut-off frequency 1 GHz).

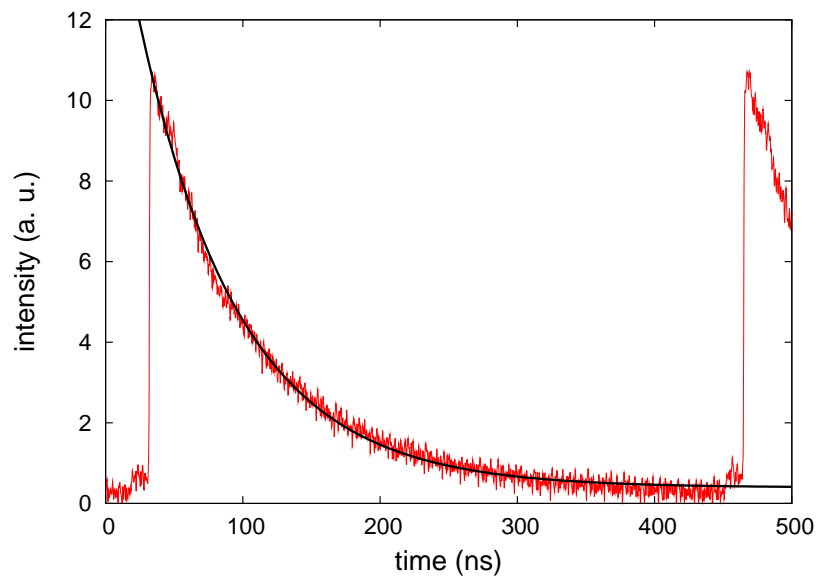


Figure 2.8: Fluorescence intensity of InGaP/ZnS QDs exposed to femtosecond excitation pulses (emission wavelength: 650 nm). The decay curve of the fluorescence is fitted to $A \exp(-t/\tau)$ where $\tau = 73.5 \pm 0.3$ ns.

Table 2.1: Excitation lifetimes of various colloidal QDs.

QD Type	Emission wavelength	Solvent	Lifetime (ns)
CdSe/ZnS	560 nm	toluene	23.1 ± 0.3
CdSe/ZnS	580 nm	toluene	23.7 ± 0.2
CdSe/ZnS	615 nm	toluene	19 ± 1
InGaP/ZnS	650 nm	water	73.5 ± 0.3

an oscilloscope with a 2 GHz bandwidth.

Figure 2.8 shows the fluorescence decay of InGaP/ZnS QDs after pulse excitations. The excitation lifetime of the QD is obtained from the fit of the QD fluorescence decay curve to an exponential function with a single exponent. Table 2.1 shows the excitation lifetimes of various QDs we have measured.

2.3.2 Absorption cross sections of CdSe QDs

Figure 2.9 shows typical absorption and emission spectra of CdSe/ZnS QDs in toluene at room temperature. The absorption spectrum (more precisely, absorptivity $A = \log(1/T)$) is measured with a PerkinElmer spectrophotometer. The transmission T is related to the absorption cross section σ of a single QD by the Beer-Lambert law:

$$T = e^{-\sigma l N}, \quad (2.8)$$

where N is the number density of the QDs in the solution, and l the thickness of the sample. Therefore, we can convert the absorptivity into the absorption cross section of a QD, using the QD concentrations given by the manufacturer. The absorption cross sections so obtained are consistent with the estimations based on our observations on single QDs (Section 2.4.4). On the other hand, the emission spectrum of the QDs is measured using a home-built spectrometer. The QDs in toluene/water are excited by 405 nm radiation from a diode laser during the measurement.

Both the absorption and emission spectra in Fig. 2.9 are greatly broadened by the size inhomogeneity of the QDs, and by acoustic and LO phonons¹¹. The absorption spectrum reveals a band edge absorption ($1S(e) - 1S_{3/2}(h)$ transition) at 586 nm, and a few other lowest energy transitions. However, the origin of the background continuum in the absorption spectrum cannot be explained by the simple exciton in a box model (Section 2.2.2). Leatherdale et al. demonstrated that the absorption continuum may instead be modeled using off-resonant light scattering by small particles [78, 79]. The absorption cross section of a CdSe QD, dominated by the small-particle scattering cross section, is on the order of the physical cross section of the nanocrystals. For example, at the excitation wavelength of 405 nm, the absorption cross sections of single CdSe QDs are less than 1 nm² for various QD sizes. This value is about a million times smaller than $\sigma_{\max} = 3\lambda^2/2\pi$, the resonant scattering cross section of a two-level system exposed to a plane wave.

¹¹The LO phonons have a single phonon energy of 25.4 meV (6.13 THz)

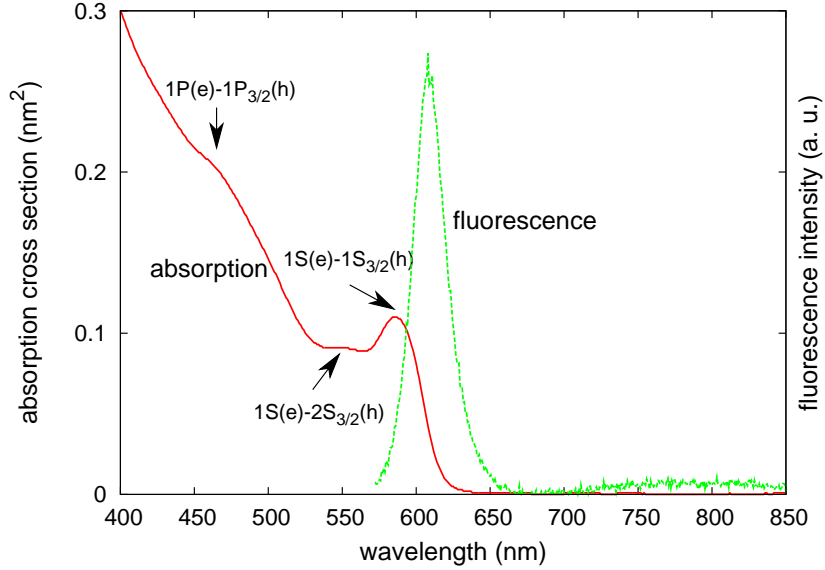


Figure 2.9: Absorption and emission spectra of CdSe/ZnS QDs in toluene (QDs' emission wavelength: 605 nm). The fluorescence spectrum shows a single strong emission peak, and a broad but weak emission tail at longer wavelengths. The broad emission tail could be due to surface state-related recombination [65, 66].

At liquid He temperatures, the absorption cross section of a colloidal CdSe QD is expected to be much higher. However, it would still be a few orders of magnitude smaller than σ_{\max} due to the spectral diffusion of the QDs. Empedocles and Bawendi [67, 68] observed that the emission spectrum of a single CdSe QD diffuses spontaneously over a few meVs (~ 1 THz) within a time scale of seconds to minutes. Such an effect could be caused by the Stark shift resulting from the variation of local electric fields, possibly due to QD photoionization and trapping of charges in the surrounding matrix [67, 80]. The variation of local electric fields is expected to affect the absorption spectrum in the same manner as it does to the emission spectrum. One would thus expect the absorption spectral width of a single colloidal QD to be broadened by approximately 1 THz, resulting in a greatly reduced absorption cross section even at liquid He temperatures.

2.4 Experiments on single colloidal QDs

2.4.1 Confocal microscope setup

We set up a confocal microscope to observe individual QDs. The main part of the setup consists of a Nikon Plan Fluorite microscope objective (MO) of 0.9 NA (Fig. 2.10(i)). The MO focuses a 405 nm light beam, that is delivered through a single mode fiber from a laser diode, onto single QDs. Red-shifted fluorescence from the dot is collected by the same MO. It passes through a longpass filter used to remove the 405 nm excitation light reflected by the MO, and is coupled into a single mode fiber. Either a Si-avalanche photodiode D1 or a Hanbury-Brown-Twiss setup (Fig. 2.10(ii)) is connected to the output end of the single mode fiber. The Hanbury-Brown-Twiss setup is used for measuring the second order correlation function $g^{(2)}(\tau)$ of the QD fluorescence. A 5 nm bandpass filter centered at the QD emission wavelength is placed between the two Si-avalanche photodiode detectors, D2 and D3, to prevent optical cross-talk between the two detectors ¹².

The nanocrystals under study are embedded in a transparent polymer sandwiched between a fused silica cover slip and a glass slide. The sample is placed on a 3D-nanopositioning unit ¹³ that has nanometer resolution and a translational range of 80 μm in three orthogonal directions. The nanopositioning unit is itself mounted to a 3D-mechanical translational stage to facilitate larger sample movement.

The setup has an estimated fluorescence detection efficiency of 2.6% if the output of the fluorescence collection fiber is directly connected to a Si-APD. The detection efficiency is obtained by considering the collection efficiency of the MO ($\simeq 10\%$), reflection losses due to optical elements (15%), coupling efficiency into the single mode fiber (76%), and the quantum efficiency of the Si-avalanche photodiode ($\simeq 40\%$). If the output of the fluorescence collection

¹²An avalanche photodiode used for single photon detection in Geiger mode emits a non-negligible amount of light [81]. The emitted light can be detected by another detector in the Hanbury-Brown-Twiss setup, resulting in artefacts in the measured $g^{(2)}(\tau)$ function.

¹³Tritor 103 CAP, Piezosystem Jena GmbH.

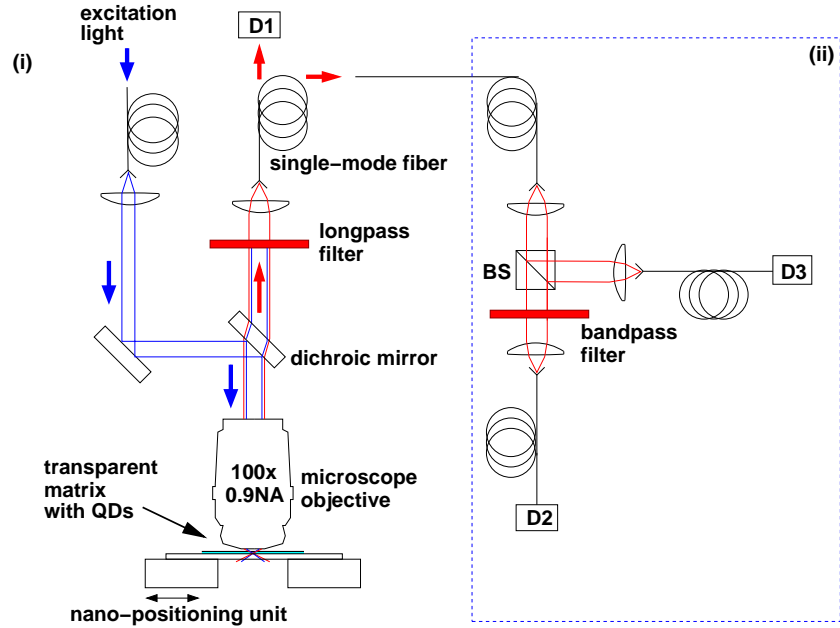


Figure 2.10: (i) The confocal-microscope setup for observing single colloidal quantum dots. (ii) A Hanbury-Brown-Twiss setup for measuring the $g^{(2)}$ function of the fluorescence from the quantum dots. BS: 50/50 beam splitter, D1, D2, D3: Si-avalanche photodiodes.

fiber is connected to the Hanbury-Brown-Twiss setup (Fig. 2.10(ii)), the fluorescence detection efficiency is about 0.8% per detector.

Alignment of the confocal microscope

The two single mode fibers used in the confocal microscope function as spatial mode selectors. They reduce the targeted excitation and fluorescence collection volumes, thus leading to high spatial resolution of the setup. Since the polymer in the sample fluoresces under UV excitation light, using single mode fibers also reduces the background noise contribution to the fluorescence detection. However, the small focal volumes of the excitation and the fluorescence target modes also make overlapping the focal volumes more challenging.

To align the confocal microscope, 590 nm light ¹⁴ is sent into the confocal setup through the fluorescence collection fiber to model the propagation of the fluorescence beam. This beam is collimated and has a Gaussian waist of $\simeq 2$ mm before entering the MO (slightly overfilling the aperture of the MO). The excitation light is collimated with a smaller Gaussian waist of 1.4 mm to avoid scattering by the MO. The excitation beam joins the fluorescence beam at the dichroic mirror. The two beams are then made coaxial within 0.2 mm over a distance of 4 meters before the MO is installed. With such pre-alignment, the two foci after the MO should overlap within $0.2 \mu\text{m}$ ¹⁵ in the direction transverse to the propagation axis. In the longitudinal direction, however, the two foci could be separated up to $15 \mu\text{m}$ because the chromatic aberration of the MO ¹⁶. The fluorescence beam is then removed and a Si-avalanche photodiode is connected to the fluorescence collection fiber instead. Ideally, at this stage, one can effectively overlap two foci transversely and longitudinally by maximizing the detected fluorescence from a single stable light emitter. Unfortunately, CdSe QDs do not fluoresce stably (Section 2.4.5), and thus cannot be used for such alignment. One stable point-like emitter is the nitrogen-vacancy (NV) centers in diamonds. However, as the emission wavelength of diamond-NV centers is different from that of the CdSe QDs, using diamond-NV centers for overlapping the foci is not ideal due to chromatic aberration of the MO.

To overcome this problem, we cut a circular 100 nm-diameter through hole using ion beam milling in a $1 \mu\text{m}$ thick gold film coated on a fused silica cover slip. We then illuminated the hole with 405 nm and 590 nm light to mimic a point source (Fig. 2.11(left)). Here, both the excitation and fluorescence-path-simulating light sources connected to the single mode fibers

¹⁴The wavelengths of the CdSe QD's fluorescence range from 500 to 620 nm, depending on the dot's diameter. Depending on the QD under studies, 632 nm light may also be used to model the propagation of the fluorescence.

¹⁵Nikon adopts a tube-lens focal length of 200 mm. A magnification of $100\times$ thus translates into an effective MO focal length of 2 mm. The transverse overlap of the foci is estimated to be $\Delta = 2 \times \frac{0.2 \text{ mm}}{4 \text{ m}} \times 2 \text{ mm} = 0.2 \mu\text{m}$.

¹⁶The foci separation of $15 \mu\text{m}$ in the longitudinal direction is observed by using the 100 nm-hole alignment method that would be mentioned shortly.

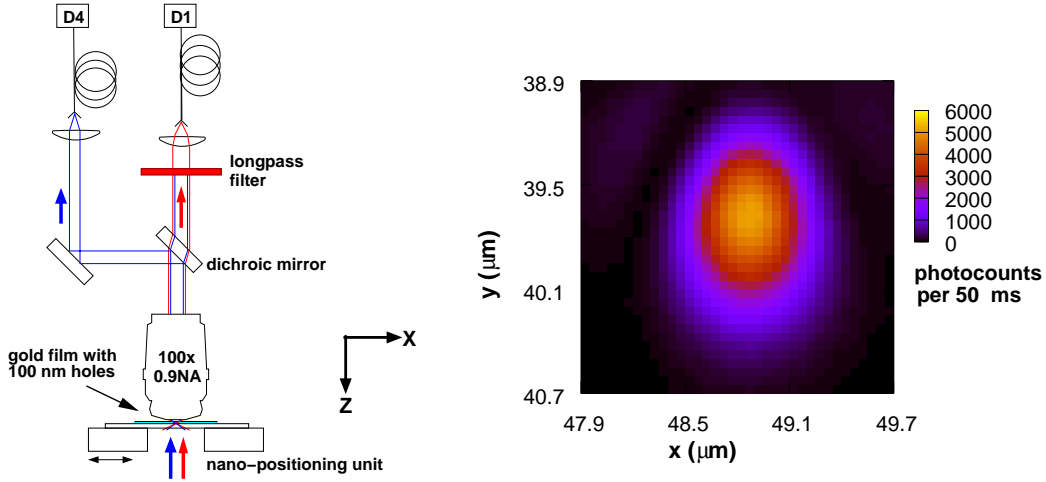


Figure 2.11: (Left) Schematic setup during alignment of the confocal microscope. D1 and D4 are two Si-avalanche photodiode. The 590 nm and 405 nm light are incident upon the gold film from below. (Right) Photocounts of detector D1 when rastering the nano-positioning unit in the XY plane.

are replaced by two single photon detectors (Fig. 2.11(left)). To overlap the excitation and ‘fluorescence’ foci, we first illuminate the hole with 590 nm light and find the position of the ‘fluorescence’ focus by rastering the nano-positioning unit. When the position of the hole (point-source) coincides with the ‘fluorescence’ focus, the photocount rate of detector D1 is at its maximum (Fig. 2.11(right)). We then illuminate the hole with 405 nm light. This time, the hole is fixed at the position of the ‘fluorescence’ focus, and the optical elements in the excitation arm is adjusted such that the photocount rate at detector D4 is optimized. With such an alignment scheme, we can overlap the excitation and fluorescence foci to less than 30 nm uncertainties in the transverse direction, and 0.4 μm in the longitudinal direction.

2.4.2 Sample preparation

In order to observe individual QDs, we sparsely embed the QDs into a transparent matrix that is sandwiched between a 110 μm thick fused silica cover

slip and a normal glass slide ¹⁷. The cover slips and glass slides are first washed with methanol, and then rinsed with plenty of distilled water. After that, they are baked at 150 °C in a glove box filled with pure nitrogen for about an hour to remove water molecules and other chemical species absorbed on the glass surface ¹⁸. We then prepare a CdSe or CdTe QD-toluene solution with a concentration of $\simeq 10^{-2}$ nmol/ml. This solution is further diluted a hundred times using a toluene solution containing 3% (by weight) of poly(methyl methacrylate) (PMMA) or polystyrene (PS). The QD-polymer-toluene solution is finally spin-coated on the glass slide and sealed with the cover slip, forming a polymer layer of about 10 μm thick.

For water-soluble glutathione-capped CdTe QDs that do not dissolve in toluene, we dilute the QDs in a $\text{SiO}_2 \cdot \text{NaOH}$ water solution (liquid glass) ¹⁹ before spin-coating. The fluorescence behaviours of the colloidal QDs, be it CdSe, CdTe, or InGaP embedded in the PMMA, PS or the liquid glass, do not differ significantly. Therefore, we only report our observations of CdSe/ZnS QDs embedded in the PMMA matrix in the following sections.

2.4.3 Observing single quantum dot

Figure 2.12 shows the photocounts of detector D1 (Fig. 2.10(i)) in a XY scan of a CdSe/ZnS-PMMA sample ²⁰. The figure clearly reveals the blinking behaviour of the fluorescence from a single QD. The dark stripe at the center of the ‘dot’ occurs because the QD goes into the dark state temporarily. Note that a QD has a size of 1–2 nm, the bright dot with a FWHM of $\simeq 400$ nm in the XY scan represents the resolution of the confocal setup. Occasionally, a number of QDs may cluster within the resolution limit and appear as a single dot. However, since it is unlikely that all the QDs fall into the dark

¹⁷Fused silica cover slips are used because normal glass cover slips fluoresce under UV light. As the matrix is thicker than 10 μm , fluorescence from the glass slide is not collected by the MO.

¹⁸With baked cover slips and glass slides, we observed longer active times of the QDs before they are bleached by excitation light.

¹⁹The liquid glass forms a transparent matrix after water in the solution evaporates.

²⁰The XY plane is perpendicular to the lens axis (Fig. 2.11(left)).

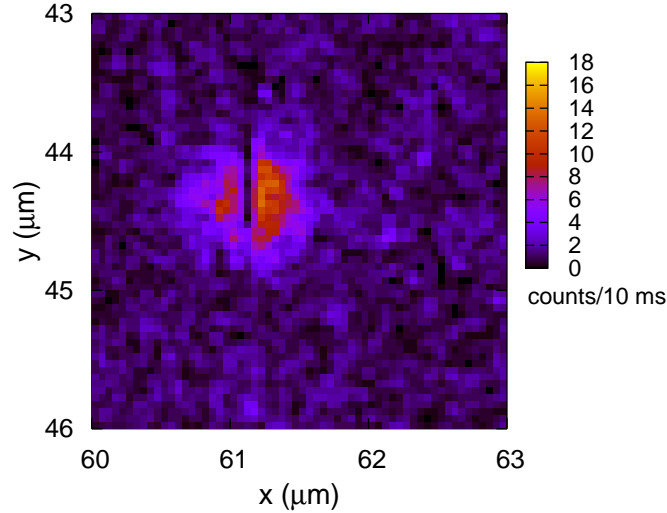


Figure 2.12: A XY scan showing a single CdSe/ZnS quantum dot embedded in a PMMA thin film. The dark stripe at the center of the bright dot is due to the QD falling into the dark state.

state simultaneously, the observation of a completely dark stripe during the XY scan is a convenient criterion for picking out real single QDs.

2.4.4 Estimation of absorption cross section by observing a single QD

Figure 2.13 is another XY scan showing two single QDs. The power of the 405 nm excitation light is about $1 \mu\text{W}$ before entering the MO. This power corresponds to a photon flux of $\simeq 2 \times 10^{12}$ photons per second. However, the largest photocount rate in this scan is about 2500 s^{-1} (Dot A). This number corresponds to a fluorescence rate of only $\simeq 1 \times 10^5 \text{ s}^{-1}$ if we assume a fluorescence detection efficiency of 2.6% (Section 2.4.1). Such a large ratio of the excitation to fluorescence photon numbers is caused by the small absorption cross section of the dots at room temperature.

To estimate the absorption cross section σ of a single QD, we note that

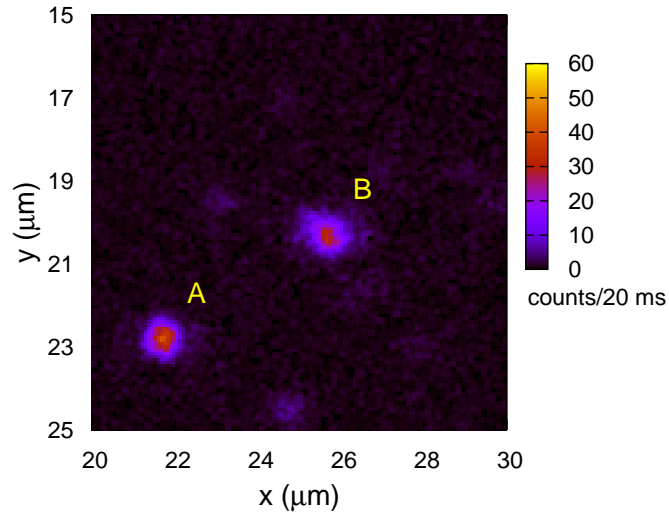


Figure 2.13: A XY scan showing two single CdSe/ZnS QDs embedded in a PMMA thin film.

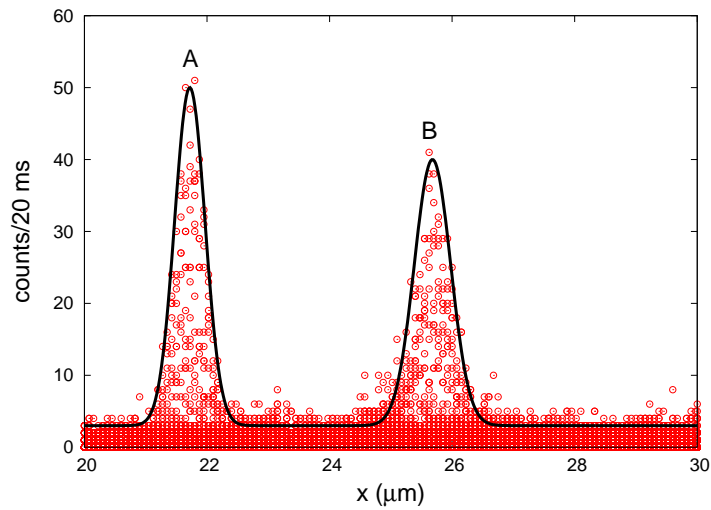


Figure 2.14: The ‘cross-sectional view’ of Fig. 2.13. The solid line is fitted using two Gaussian functions, $h \exp\left[-\frac{2(x-x_0)^2}{w^2}\right]$. Peak **A** has a width w of $0.50 \mu\text{m}$. Peak **B** has a lower fluorescence counts and a larger width w of $0.60 \mu\text{m}$, because QD B is 2 to $3 \mu\text{m}$ off the focal plane.

the detected fluorescence photocount rate R_d is given by

$$R_d = I_e \sigma \eta_q \eta_d / \hbar \omega, \quad (2.9)$$

where I_e is the intensity of excitation light at the focus, η_q the quantum yield of the QD, η_d the fluorescence detection efficiency, and $\hbar \omega$ the single photon energy at the excitation wavelength.

The excitation field intensity at the focus can be estimated using the intensity distribution at the focal plane. Figure 2.14 shows the ‘cross-sectional view’ of Fig. 2.13. Fitting the spatial distribution of the photocounts with a Gaussian function gives a waist of $w = 0.5 \mu\text{m}$ for dot A that lies in the focal plane. Note however that the so obtained waist is not identical to the focal waist of the excitation beam. For a confocal microscope, the spatial profile of the photocounts in a XY scan is determined by both the spatial distributions of the excitation and fluorescence collection efficiencies. More explicitly, if we assume the intensity distributions of the 405 nm excitation light and the 590 nm fluorescence-simulating light are Gaussian in the focal plane, then the normalized spatial distribution of the observed fluorescence is given by ²¹

$$\Psi(\rho) = \exp\left(-\frac{2\rho^2}{w_e^2}\right) \exp\left(-\frac{2\rho^2}{w_f^2}\right), \quad (2.10)$$

where ρ is the distance from the center of the dot in the focal plane, w_e and w_f are the focal waists of the excitation and ‘fluorescence’ light respectively. As a result, if we assume that $w_e \simeq w_f$ for simplicity, the focal waist of the excitation beam is given by $\sqrt{2} \times 0.5 \mu\text{m} = 0.7 \mu\text{m}$. This leads to a focal excitation intensity of $I_e \simeq \frac{2 \times 1 \mu\text{W}}{\pi(0.7 \mu\text{m})^2} = 1.3 \times 10^6 \text{ W/m}^2$.

By substituting $R_d \simeq 2500 \text{ s}^{-1}$, $\eta_q \simeq 0.5$ ²², $\eta_d \simeq 2.6\%$ and I_e into Eqn. 2.9, we estimate the absorption cross section of a single CdSe QD to be 0.1 nm^2 . This value is in good agreement with the absorption cross section measured in the bulk experiment (Section 2.3.2). We emphasize that the

²¹Here, we implicitly assume that the confocal microscope is well aligned, such that the excitation beam and the fluorescence collection beam coincides.

²²The quantum yield of the CdSe QDs is above 0.5 according to the supplier. This value is also supported by other reports [31, 32, 35, 36, 37].

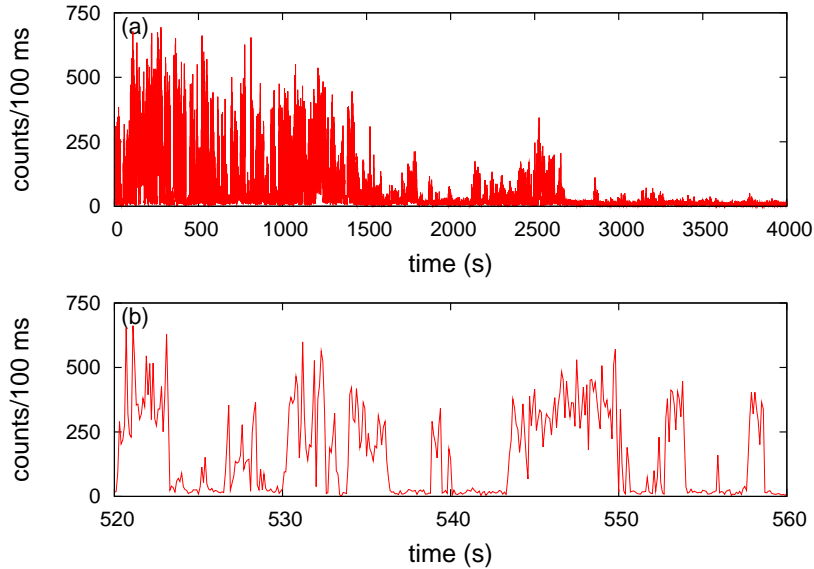


Figure 2.15: (a) Typical fluorescence observed from a single CdSe/ZnS QD. The QD is irreversibly photobleached after one hour. (b) A zoom-in of (a) showing the QD going into the dark state intermittently. The dot also goes into a fluorescence quenching state very briefly when it is ‘bright’, resulting in non-uniform photocounts which are integrated over 100 ms in this case.

QD is not saturated by the excitation light in this experiment, thus the small absorption cross section is not due to over-saturation. Instead, it is due to the broadening of the transition lines by the phonons.

2.4.5 Fluorescence from a single QD

Figure 2.15 shows typical photocounts of detector D1 (Fig. 2.10(i)) when the focus of the confocal microscope is fixed on a single QD. Under light excitation, the fluorescence of a QD exhibits an on/off behaviour when it transits between the bright and dark states (Fig. 2.15(b)). The transitions are believed to be related to the random ionization and neutralization of the QD (Section 2.2.4). Overall, the fluorescence intensity of single QDs decreases over time. All QDs are photobleached irreversibly after a number of seconds to at most a few hours. We have spent a considerable amount of effort in trying to extend the active times of the QDs. However, as the active

times of different QDs within the same sample can vary significantly (from seconds to hours), it is difficult to clearly identify the effects of different sample preparation techniques. Nevertheless, we observed that removing oxygen and water contaminations in the sample increases the active time of the QDs in general.

2.4.6 The $g^{(2)}(\tau)$ function

To show conclusively that we are observing single QDs, we measure the second order correlation function $g^{(2)}(\tau)$ of a QD's fluorescence using the Hanbury-Brown-Twiss setup shown in Fig. 2.10(ii) (see Section 4.3 for definition of $g^{(2)}(\tau)$). Figure 2.16 shows the $g^{(2)}(\tau)$ obtained from the fluorescence of a CdSe/ZnS QD in PMMA. The signal-to-noise ratio in this figure is poor because the QD was photobleached after 50 minutes. Nevertheless, the dip to zero at delay $\tau = 0$ is a signature of fluorescence from a single quantum system. In the case of a single ^{87}Rb atom (Section 4.3), emission of a photon signifies that the atom is in its ground state and cannot immediately emit a consecutive photon, therefore resulting in an anti-bunching behaviour in the fluorescence. The fluorescence of a CdSe nanocrystal, on the other hand, shows anti-bunching behaviour for a slightly different reason. The main difference is that there is only one outer electron in a Rb atom, whereas there can be multiple excitons in a single CdSe nanocrystal. Therefore, emission of a photon from a CdSe nanocrystal does not guarantee that the nanocrystal is in its ground state (zero exciton). The observation of a strong anti-bunching effect in CdSe QDs is assisted by the fact that the dots do not fluoresce when there is more than one exciton in the QDs. That is, multi-exciton relaxation is always carried out by the much more efficient Auger recombination process (Section 2.2.4). This effect suppresses the contribution of multi-photon emission [82].

Another feature of the $g^{(2)}(\tau)$ of fluorescence from a single CdSe QD is the lack of Rabi oscillations [82] as compared to that of an atom (Fig. 4.5). This feature is to be expected because of the short (< 1 ps) intraband relaxation time of the electron and hole in the nanocrystal that destroys the coherence

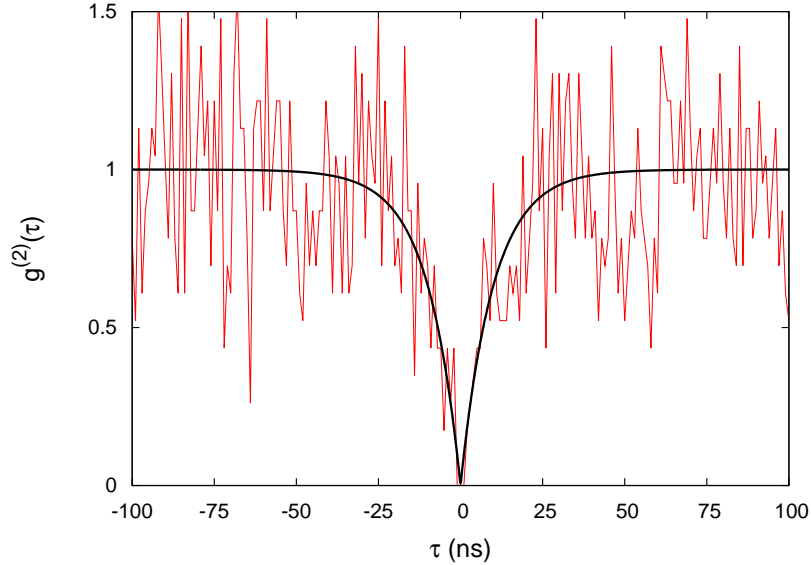


Figure 2.16: Normalized histogram of the time delays τ between photodetection events at detectors D2 and D3, obtained from the fluorescence of a single CdSe/ZnS QD (not corrected for background counts). The smooth black line is a fit to the data points using $g^{(2)}(\tau) = 1 - \exp(-|\tau|/\tau_0)$ with $\tau_0 = 10.0 \pm 1.2$ ns.

necessary to observe the Rabi oscillations.

2.5 Conclusion

In this chapter, we reviewed the properties of colloidal QDs (CdSe/ZnS, CdTe/ZnS) and documented our attempt to characterize these dots for the purpose of quantum information processing. The main electronic properties of these dots can be described by modeling the excited electron and hole as particles in a spherical box using the effective mass approximation. To fully explain the low temperature absorption and emission spectra of these dots, one must take into account (i) quantum-confinement induced band mixing of the bulk CdSe valence bands, (ii) exchange interaction between the electron and hole, and (iii) anisotropy of the nanocrystal due to the hexagonal crystal field and prolated shape of the nanocrystal.

The excitons in the colloidal QDs have a coherent time of less than 1 ps.

This phenomenon is due to the rapid intraband relaxation assisted by the acoustic phonons and the closely-spaced energy levels of the hole. At room temperature, the transition linewidths of these QDs are greatly broadened by the acoustic and LO phonons. We consistently found that the absorption cross section of a CdSe/ZnS QD to be on the order of 0.1 nm^2 . This value is a million times smaller than that of a dipole-allowed non-broadened transition. Even at liquid He temperatures, the absorption cross section of these dots is expected to be a few orders of magnitude smaller than the maximum allowed due to random spectral diffusion of a few meV (1 THz) wide.

In order to observe single QDs individually, we set up a confocal microscope, and prepared samples where colloidal QDs (CdSe/ZnS, CdTe/ZnS, InGaP/ZnS) were sparsely embedded in transparent matrices such as PMMA, PS, and liquid glass. Like other quantum systems, colloidal QDs can be used to generate single photons. However, these dots fall into the dark state intermittently when ionized and thus its fluorescence intensity is not stable. The biggest problem with colloidal QDs is that they are chemically unstable under optical excitation. They become irreversibly bleached after an excitation period ranging from a few seconds to a few hours.

In short, we conclude that the short coherent time and low absorption cross section of the colloidal QDs render them a very difficult candidate for storage of quantum information. Until the photobleaching problem is overcome, using these QDs for quantum information processing remains untenable.

Due to the aforementioned problems of colloidal QDs, we switched our focus to a ‘cleaner’ system – a single atom. We again tried to quantify the interaction strength between light and a single atom in free space. Our results, which include an experiment (Chapter 4) and a theoretical study (Chapter 3), show conclusively that efficient atom-light interaction is achievable by focusing light onto an atom without a cavity.

Chapter 3

Interaction of focused light with a two-level system

Atom-light interaction at the single quanta level plays an important role in many quantum communication and computation protocols [2]. While spontaneous emission allows a simple transfer of atomic states into ‘flying’ qubits, strong interaction of light with an atom is needed to transfer a photonic qubit into internal atomic degrees of freedom (stationary qubit). This process is essential to implement quantum light-matter interfaces [18, 19, 83], unless post-selection techniques are used [84]. A useful measure of interaction strength for a variety of physical configurations is the excitation probability of an atom by a single photon, independent of any particular scheme of information transfer from a photon to an atom.

The common approach to achieve this strong interaction is to use a high finesse cavity around the atom, in which the electrical field strength of a single photon is enhanced by multiple reflections between two highly reflective mirrors, resulting in a high probability of absorption [22, 23, 24, 25].

Another approach is to increase the excitation probability of an atom due to a single photon simply by focusing the light field of a single photon down to a diffraction limited area, motivated by the fact that the absorption cross section of an atom is on the order of the square of the optical wavelength. Recent theoretical research in this direction predicts that the absorption

probability may reach the maximal value of 100% [85]. There, the authors suggested placing an atom at the focus of a large ¹ parabolic mirror, and focusing a ‘radially’ polarized light beam onto the atom [85]. However, such a coupling scheme is challenging to realize experimentally. A simpler scheme would be to use a lens to tightly focus light to the position of the atom.

Such a system has been theoretically investigated by van Enk and Kimble [1] and they concluded that one can expect only low absorption (scattering) probability for lenses with realistic focal lengths. However, our recent experimental results [27] showed that the predictions given in their work greatly underestimate the scattering probability of a tightly focused coherent light beam by a single atom. In this chapter, we extend the model used in [1] so that it is applicable to the strong focusing regime. We find that, by dropping two of their approximations, the interaction of a coherent light field with a single atom can be very strong even for realistic lenses. By presenting this theoretical extension before the experiment, we hope not only to clarify the key parameters in optimizing the interaction strength between strongly focused light and an atom, but also to highlight the properties of strongly focused fields used in our experiment. This should provide the readers with greater clarity and insights when we discuss our experimental setup, its limitations, and our experimental results in Chapter 4. The main results of this theoretical work are published in [26].

3.1 Interaction strength

A good measure of interaction strength between an atom and light in terms of quantum information transfer is the excitation probability of an atom by a single photon. Single photons can be readily generated from spontaneous emission of single quantum systems like atoms [86], molecules [82, 87], quantum dots [88, 89], color centers [90], etc. They can also be created from single quantum systems with the assistance of cavity [91, 92, 93]. In our experiment, however, we do not create single photon wave packets and use these

¹Such parabolic mirror should ideally extend to infinity so as to create a focusing field covering a full solid angle 4π .

packets to excite an atom. For simplicity, we use a weak narrow bandwidth radiation to excite a single atom.

When a single atom isolated in free space is exposed to weak monochromatic radiation (probe), it releases the ‘absorbed’ energy by emitting radiation that is phase-coherent with the incident radiation (coherent scattering) [94, 95]. An excited semiconductor nanocrystal embedded in a transparent matrix, on the other hand, can emit radiation with a lower frequency (incoherent scattering) and create phonons carrying the remaining energy into the surrounding matrix (heat absorption). Studying the interaction strength between radiation and the quantum system in the latter case is more complicated. Here, we consider the previous scenario only. In this case, the interaction strength between the light beam and a single atom (excitation probability) is equivalent to the scattered probability, which is defined as the ratio of the scattered light power P_{sc} to the total incident power P_{in} . However, it is experimentally challenging, if not impossible, to measure P_{sc} directly since the detection area must cover the whole solid angle, including that subtended by the probe beam. Thus, a common method for quantifying the scattered power is to infer it from a transmission measurement. For the system under investigation, a simple transmission setup is illustrated in Fig. 3.1. There, a second lens collects all the excitation power if no atom is present at the focus. The measured transmission is defined as the ratio of the outgoing power P_{out} to the incident power P_{in}

$$T \equiv \frac{P_{\text{out}}}{P_{\text{in}}} = \frac{P_{\text{in}} - P_{\text{sc}} + \alpha P_{\text{sc}}}{P_{\text{in}}}, \quad (3.1)$$

where α represents the fraction of scattered light collected by the transmission power detector. It can be estimated from the overlap of the emission profile of the scattered light and the detection target mode. The scattering probability is related to the measured transmission by

$$p_{\text{sc}} \equiv \frac{P_{\text{sc}}}{P_{\text{in}}} = \frac{\epsilon}{1 - \alpha}, \quad (3.2)$$

where $\epsilon = 1 - T$ is the extinction of the probe beam. The scattering prob-

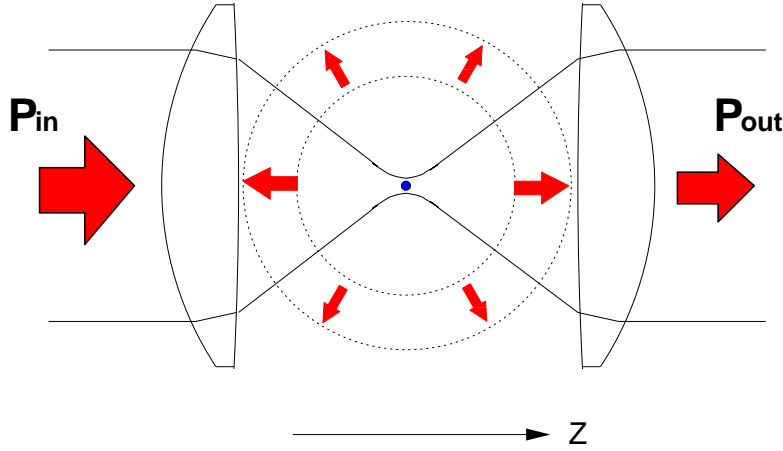


Figure 3.1: A transmission measurement setup with an atom at the focus of a lens. The transmitted power consists of light that is not scattered by the atom, and part of the scattered light.

ability is always larger than the measured extinction and becomes almost equal only for small α . Note that although Eqn. 3.2 is obtained by simple consideration of optical power, it is fully consistent with a more complete model that takes into account the interference between the scattered field and the probe field [26].

3.2 Interaction of a focused radiation with a two-level system

In this section we consider a scenario where a circularly polarized Gaussian beam is focused by an ideal lens onto a two-level atom located at the focus of the lens. Our purpose is to derive an expression for the scattering probability assuming weak on-resonant excitation. The reasons why we consider a circularly polarized Gaussian beam are:

1. We use circularly polarized light to optically pump a ^{87}Rb atom into a two-level cycling transition in our experiment (Chapter 4);
2. In the original proposal for a quantum network [18] and in most experiments (including our experiment in Chapter 4), information carrying

photons are transported using a single mode fiber. As the output field from a single mode fiber has a Gaussian spatial mode, considering a Gaussian beam is thus useful.

There are different approaches to obtain the scattering probability. To give a more complete picture, we will discuss three approaches and point out their possible limitations. The first approach considers absorption as the reverse process of spontaneous emission to obtain the scattering (absorption) probability. The second approach compares the scattering cross section of the atom and the ‘size’ of the focused beam to obtain the scattering probability. The third approach requires knowledge of the field at the focus, and uses semi-classical approximation to obtain the scattering probability. We adopt the third approach.

3.2.1 Reverse process of spontaneous emission

In free space, the spontaneous emission of a single photon is characterized by an exponential decay of the upper state population of the emitter [96], which is due to the interaction of the emitter with an infinite number of vacuum field modes. As these modes can be considered as a heat bath [97], the process of spontaneous emission in free space is often regarded as an irreversible process. However, Sondermann et. al [85] argued that this irreversibility is to be understood in a thermodynamical sense, but not as a violation of time reversal symmetry. They argued that the reversibility of the spontaneous emission process can be inferred from the fact the Schrödinger equation is invariant under time reversal for a closed system with a Hamiltonian without any explicit time dependence. The implication of such a conclusion is that: if one is able to artificially create the time reversed version of the dipole wave that is emitted by an atom, one would find that this wave would be absorbed by the atom with a probability of one. To be more explicit, one needs to create a wave (a single photon), moving towards the atom, whose spatial and temporal profiles match the respective atomic dipole emission [98]. To calculate the absorption probability, one typically evaluates the overlap between the incoming field and that of the dipole emission. Although

the above picture is intuitively simple, it cannot be easily applied to our system to quantify the scattering probability. This is because our setup uses monochromatic light instead of single photon pulses to excite the atom.

3.2.2 Scattering cross section

Another common approach to estimate the scattering probability is by comparing the ‘cross sectional area’ of the focused field to σ_{\max} – the scattering cross section of a two-level system exposed to a weak resonant monochromatic plane wave, given by [95, 99, 100] (Appendix A.1)

$$\sigma_{\max} = 3\lambda^2/2\pi. \quad (3.3)$$

For an optical wavelength of say 780 nm, this scattering cross-section is approximately $0.3 \mu\text{m}^2$, even though the diameter of an atom is only a few angstroms. If σ_{\max} is interpreted as the cross-section of a classical object such that all of the light that falls onto this object is scattered, one could estimate the scattering probability p_{sc} by

$$p_{\text{sc}} = \frac{\sigma_{\max}}{A}, \quad (3.4)$$

where A is the area of the beam. In particular, as the diffraction limited focal spot area of a radiation with wavelength λ is on the order of $\sim \lambda^2$, Eqn. 3.4 points to the possibility of achieving substantial scattering by focusing light onto a two-level system. Nevertheless, it should be emphasized that Eqn. 3.4 does not reflect the actual scattering probability. In fact, an atom interacts only with the field within the size of the atom. It is the polarization and the amplitude of the field within the size of the atom that determines the power of the field scattered by the atom. In the case of strong focusing, the polarization and intensity of the focused field can vary appreciably within a distance smaller than a wavelength (Section 3.3.4). Over-focusing a field pushes some field energy to side-lobes near the focus, and thus decreases the field strength at the focus (Section 3.3.4). As a result, a beam with a smaller focal area A does not necessarily create a field that interacts more

strongly with an atom. Furthermore, as the definition of the focal area A is quite arbitrary, Eqn. 3.4 is therefore not accurate in predicting the scattering probability of a focused light field by a single atom.

3.2.3 Scattering probability from first principles

In order to predict the scattering probability of a light beam by an atom accurately, it is necessary to know the properties of the field at the location of the atom. Consider again the setup shown in Fig. 3.1 where a monochromatic Gaussian beam is focused by a lens onto a two-level atom. We assume that the incident light is circularly polarized and the waist of the Gaussian beam coincides with the focusing lens. The electric field strength before the lens is given by

$$\vec{E}(t) = \frac{E_L}{\sqrt{2}} [\cos(\omega t)\hat{x} + \sin(\omega t)\hat{y}] e^{-\rho^2/w_L^2}, \quad (3.5)$$

where ρ is the radial distance from the lens axis, w_L the waist of the beam, \hat{x}, \hat{y} are the unit vectors in X and Y directions respectively, and E_L is the field amplitude. The power carried by the incident beam is given by

$$P_{\text{in}} = \frac{1}{4}\epsilon_0\pi c E_L^2 w_L^2, \quad (3.6)$$

where ϵ_0 is electric permittivity in vacuum. Due to the symmetry of the system, the field on the lens axis is always circularly polarized. So for an atom that is stationary on the z-axis at the focus of the lens, the electric field can be written as

$$\vec{E}(t) = \frac{E_A}{\sqrt{2}} [\cos(\omega t)\hat{x} + \sin(\omega t)\hat{y}], \quad (3.7)$$

where E_A denotes the amplitude of the field at the focus. A two-level system exposed to such a classical field is a well studied system [95, 99, 100]. Neglecting spontaneous decay of the excited state, a two-level system exposed to a resonant classical field undergoes Rabi oscillation in which the state of the atom oscillates between the ground state and the excited state with a Rabi frequency Ω (Appendix A.1). With spontaneous emission, the popula-

tion of the excited state ρ_{22} (the probability that the atom is in the excited state) reaches a dynamic equilibrium. The average power scattered by the two-level system can be shown to be

$$P_{\text{sc}} = \rho_{22}\Gamma\hbar\omega, \quad (3.8)$$

where Γ is the spontaneous decay rate of the two-level system. To maximize the scattering probability, one needs to optimize ρ_{22} for a fixed incident power. This is achieved only when the intensity of the external field is weak ($\Omega \ll \Gamma$) and the field resonates with the two-level system. Under these conditions, the power scattered by a two-level atom is given by (see Appendix A.1)

$$P_{\text{sc}} = \frac{3\epsilon_0 c \lambda^2 E_A^2}{4\pi}, \quad (3.9)$$

leading to a scattering probability of

$$p_{\text{sc}} = \frac{P_{\text{sc}}}{P_{\text{in}}} = \frac{3\lambda^2}{\pi^2 w_L^2} \left(\frac{E_A}{E_L} \right)^2. \quad (3.10)$$

Eqn. 3.10 is exact under the conditions of weak and on-resonant excitation. The remaining task now is to obtain the ratio, $(E_A/E_L)^2$. For a weakly focused field where the paraxial approximation holds one finds that

$$(E_A/E_L)^2 = (w_L/w_f)^2, \quad (3.11)$$

where w_f is the Gaussian beam waist at the focus. This leads to the following expression for the scattering probability:

$$p_{\text{sc}} = \frac{3\lambda^2}{\pi^2 w_f^2} = \frac{2\sigma_{\text{max}}}{\pi w_f^2}. \quad (3.12)$$

Comparing Eqn. 3.4 and Eqn. 3.12, we see that Eqn. 3.4 gives the correct scattering probability when we define the ‘area’ of the Gaussian focal spot A as $\pi w_f^2/2$. However, for strongly focused light, the paraxial approximation breaks down, and we require other methods to find $(E_A/E_L)^2$.

3.3 Calculation of field after an ideal lens

In the last section, we found that the scattering probability of a light beam by an atom is proportional to $(E_A/E_L)^2$ (Eqn. 3.10). This means that, to achieve optimal scattering probability, one would need to maximize E_A for a given E_L by tightly focusing the incident field. As there is no analytical expression for a tightly focused field, the scattering probability can only be calculated numerically. Given the properties of the incident field and the lens, the field at the focus can be fully determined by Maxwell equations. In principle, we can compute the field at the focus, and thus the scattering probability for any lens. However, our purpose here is not to design a perfect lens that creates the tightest focus. Instead, we start by considering an ideal lens and assuming a focusing field after the lens. We then propagate the focusing field to the location of the atom and compute the properties of the field around the focus exactly.

Our approach follows closely a paper by S. J. van Enk and H. J. Kimble [1]. The main idea of their method is to expand the outgoing field after a lens in a complete set of modes that satisfies the source-free Maxwell equations. In principle, one can choose any complete set of modes as the basis for the expansion, such as multipole waves [101, 102], plane waves, etc. Van Enk and Kimble adopted a set of modes that takes on a simple form in cylindrical coordinates, making use of the symmetry of the system. Once the contribution of each mode is known, the properties of the field at any location after the lens can be determined with certainty and the scattering probability can be obtained. Here, we extend their model to the strong focusing regime. The extension is done by modeling the lens action such that the focusing field has a spherical wave front after the lens and is compatible with Maxwell equations.

3.3.1 Cylindrical symmetry modes

We briefly outline the main properties of the cylindrical modes, directly following [1]. The complete orthogonal set of modes \vec{F}_ν is defined such that an electric field that satisfies the source-free Maxwell equations can be expanded

in these modes as

$$\vec{E}(t) = 2\Re \left[\sum_{\nu} a_{\nu} \vec{F}_{\nu} e^{i\omega t} \right], \quad (3.13)$$

where the summation over ν is a short-hand notation for

$$\sum_{\nu} \equiv \int dk \int dk_z \sum_s \sum_m, \quad (3.14)$$

and a_{ν} are arbitrary complex amplitudes. The modes are characterized by four indices $\nu \equiv (k, k_z, m, s)$, where $k = \frac{2\pi}{\lambda}$ is the wave vector modulus, $k_z = \vec{k} \cdot \hat{z}$ the wave vector component in z -direction, m an integer-valued angular momentum index, and $s = \pm 1$ the helicity.

Since the electrical field has to satisfy Maxwell equations, the mode function should be transverse, i.e., $\nabla \cdot \vec{F}_{\nu} = 0$. The dimensionless mode functions \vec{F}_{ν} in cylindrical coordinates (ρ, z, ϕ) are defined in [103] as

$$\begin{aligned} \vec{F}_{\nu}(\rho, z, \phi) &= \frac{1}{4\pi} \frac{sk - k_z}{k} G(k, k_z, m + 1) \hat{e}_- + \frac{1}{4\pi} \frac{sk + k_z}{k} \\ &\times G(k, k_z, m - 1) \hat{e}_+ - i \frac{\sqrt{2} k_t}{4\pi k} G(k, k_z, m) \hat{z}, \end{aligned} \quad (3.15)$$

where $k_t = \sqrt{k^2 - k_z^2}$ is the transverse part of the wave vector, $\hat{e}_{\pm} = (\hat{x} \pm i \hat{y}) / \sqrt{2}$ are the two circular polarization vectors, and

$$G(k, k_z, m) = J_m(k_t \rho) \exp(ik_z z) \exp(im\phi), \quad (3.16)$$

with J_m the m th order Bessel function. The mode functions satisfy the orthogonality relations

$$\int dV \vec{F}_{\nu}^*(\vec{r}) \cdot \vec{F}_{\nu'}(\vec{r}) = \delta(k - k') \delta(k_z - k'_z) \delta_{mm'} \delta_{ss'} / k, \quad (3.17)$$

where the integration extends over all space.

As we are interested in a monochromatic beam with a fixed value of $k = 2\pi/\lambda$ propagating in the positive z direction ($k_z > 0$), the set of mode indices is reduced to $\mu \equiv (k_t, m, s)$ where, for convenience, k_t is taken as a

mode index instead of k_z . Now, we introduce the notation

$$\sum_{\mu} \equiv \int dk_t \sum_s \sum_m \quad (3.18)$$

for a complete summation over all possible modes. For a fixed k the modes \vec{F}_{μ} are orthogonal in planes perpendicular to the z axis:

$$\int dS \vec{F}_{\mu}^*(\vec{r}) \cdot \vec{F}_{\mu'}(\vec{r}) = \delta(k_t - k'_t) \delta_{mm'} \delta_{ss'} / (2\pi k_t), \quad (3.19)$$

where dS is a surface element on such a plane.

3.3.2 Focusing with an ideal lens

Similar to [1] we model an ideal lens by multiplying a local phase factor $\varphi(\rho)$ to the incoming field \vec{F}_{in} . As in Section 3.2.3, we consider a collimated circularly polarized Gaussian beam which is focused by an ideal lens in the plane $z = 0$. In the new notation, the dimensionless incoming field is given by

$$\vec{F}_{\text{in}} = \exp\left(-\frac{\rho^2}{w_L^2}\right) \hat{e}_+, \quad (3.20)$$

and the output field right after the lens is modeled by

$$\vec{F}_{\text{out}}(\rho, \phi, z = 0) = \varphi(\rho) \exp\left(-\frac{\rho^2}{w_L^2}\right) \hat{e}_+. \quad (3.21)$$

The complete output field is then obtained by

$$\vec{F}_{\text{out}}(\vec{r}) = \sum_{\mu} \kappa_{\mu} \vec{F}_{\mu}(\vec{r}), \quad (3.22)$$

with

$$\kappa_{\mu} = 2\pi k_t \int_{z=0} dS \vec{F}_{\text{out}}(\vec{r}) \cdot \vec{F}_{\mu}^*(\vec{r}). \quad (3.23)$$

Now one has to choose an appropriate phase factor $\varphi(\rho)$ to describe the action of the lens on the incoming field. Our aim is to select a $\varphi(\rho)$ that gives rise to the strongest possible focusing, with the condition that the field after

the lens should be physical, i.e. it satisfies the source-free Maxwell equations. One would guess that a $\varphi(\rho)$ that gives strongest focusing should create a spherical wave front after the lens, because a light field emitted from a small object has a spherical wave front.

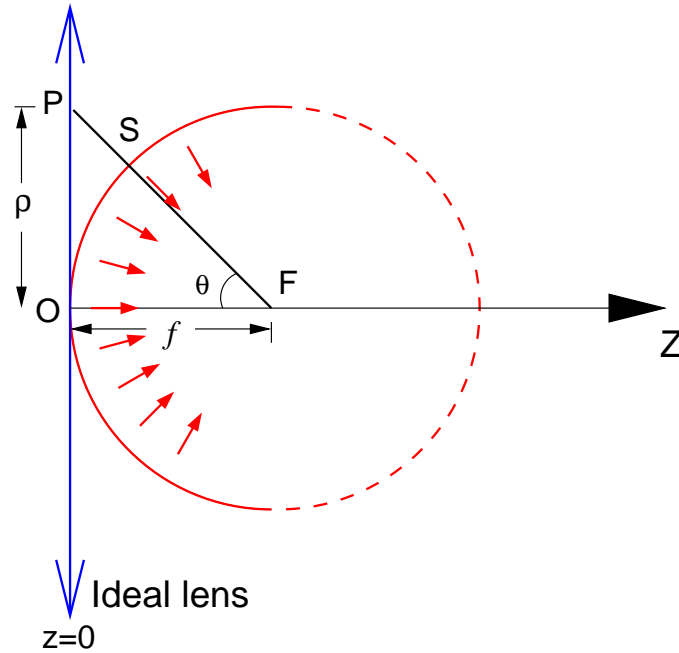


Figure 3.2: A spherical wave front (half of the sphere) formed after passing an ideal thin lens. Here F is the focal point of the lens, f is the focal length, S is the intercept point of line PF and the wave front.

In van Enk and Kimble's paper [1] the local phase factor was chosen to be

$$\varphi_{\text{pb}}(\rho) = e^{-ik\rho^2/2f}, \quad (3.24)$$

where f is the focal length of the lens. This phase factor gives rise to a parabolic wave front after the lens². The choice of this phase factor allows an analytical integration for obtaining the coefficients κ_μ . However, as a parabolic wave front approaches a spherical wave front only for $\rho \ll f$, this phase factor is not expected to give the strongest focusing. As it turns out,

²The wave front of the field resembles an elliptical paraboloid for small $\rho \ll f$. However, it is not parabolic for large ρ .

$\varphi_{\text{pb}}(\rho)$ greatly underestimates the field strength at the focus especially in the case of strong focusing, and thus is not applicable for describing lenses with high numerical aperture. Moreover, in our experiment (Chapter 4) much higher values of scattering probabilities than that predicted with the help of Eqn. 3.24 were directly measured [27]. In view of the large discrepancies, we describe the lens with a different local phase factor

$$\varphi_{\text{sp}}(\rho) = e^{-ik(\sqrt{\rho^2+f^2}-f)}, \quad (3.25)$$

which is expected to create a focusing field with a spherical wave front after the lens ³. With phase factor φ_{sp} , the expansion coefficient κ_μ becomes

$$\kappa_\mu = \delta_{m1} \pi k_t \frac{sk + k_z}{k} \int_0^\infty d\rho \rho J_0(k_t \rho) \exp \left[-ik(\sqrt{\rho^2 + f^2} - f) - \frac{\rho^2}{w_L^2} \right]. \quad (3.28)$$

This integration has no analytical solution and is thus computed numerically. As one of the mode indices k_t is a continuous variable, a sufficiently large number of k_μ must be first computed and then interpolated in order to correctly construct the output field (see Appendix A.2 for more details). The largest component of the output field (Eqn. 3.22) is the \hat{e}_+ component, which is given by

$$F_+(\rho, \phi, z) = \sum_{s=\pm 1} \int_0^k dk_t \frac{1}{4\pi} \frac{sk + k_z}{k} J_0(k_t \rho) \times e^{ik_z z} \kappa_{\mu=(k_t, 1, s)}, \quad (3.29)$$

³ **Creating spherical wave front with φ_{sp} :** The main function of the local phase factor

$$\varphi_{\text{sp}}(\rho) = e^{-ik(\sqrt{\rho^2+f^2}-f)} \quad (3.26)$$

is to introduce a phase advancement of $\eta(\rho) = k(\sqrt{\rho^2 + f^2} - f)$ to the field at point P($\rho, \phi, z = 0$). Referring to Fig. 3.2 where we show a spherical wave front formed after passing an ideal thin lens, one can easily show that the distance between point P and point S is given by

$$PS = \sqrt{\rho^2 + f^2} - f. \quad (3.27)$$

Therefore, when a wave that originates from point P arrives at point S, it would have a phase equal to that at point O. As this conclusion is true for all point P($\rho, \phi, z = 0$) of different ρ . The local phase factor $\varphi_{\text{sp}}(\rho)$, therefore, creates a spherical wave front after the lens.

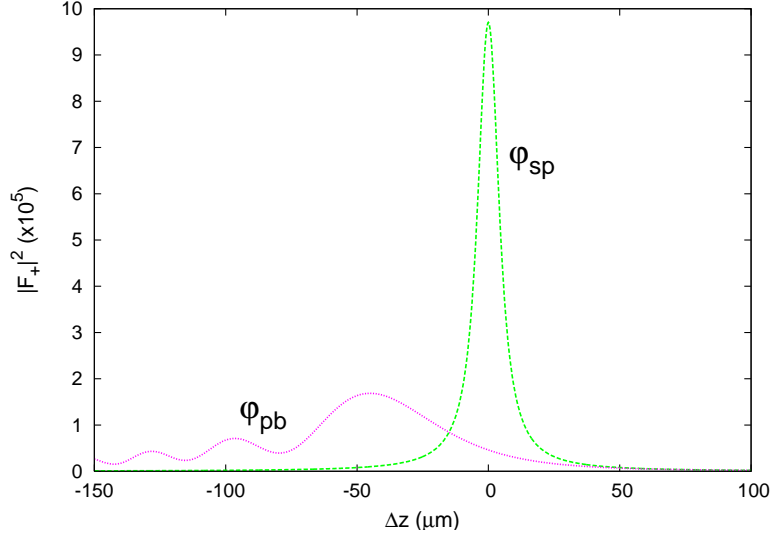


Figure 3.3: $|F_+|^2$ along the lens axis obtained with the spherical phase factor φ_{sp} and the parabolic phase factor φ_{pb} for the parameters mentioned in the text.

where $F_+ \equiv \vec{F}_{\text{out}} \cdot \hat{\epsilon}_+^*$, and $\hat{\epsilon}_+^*$ is the complex conjugate of $\hat{\epsilon}_+$.

Figure 3.3 shows the near-focus dimensionless intensity $|F_+|^2$, obtained for the parameters: $f = 4.5$ mm, $\lambda = 780$ nm and $w_L = 1.1$ mm⁴, using the phase factors φ_{sp} and φ_{pb} . The horizontal axis shows the displacement from the ideal focal position along the lens axis, $\Delta z = z - f$. It is clear from the figure that adopting a parabolic wave front significantly reduces the maximum intensity after the lens. Unlike $\varphi_{\text{sp}}(\rho)$ which concentrates the energy of the field in a small region, $\varphi_{\text{pb}}(\rho)$ spreads the energy of the focused field over a region closer to the lens, and thus results in a reduced intensity in the focus, similar to spherical aberration in classical optics. This problem becomes more serious for a larger incident waist w_L (or stronger focusing) because a parabolic wave front deviates more from a spherical wave front for larger ρ .

The numerical result for $|F_+|^2$ allows now the calculation of the scattering

⁴These parameters correspond to the values used in the experiment.

probability (Eqn. 3.10). With

$$\left(\frac{E_A}{E_L}\right)^2 = |F_+|^2 \quad (3.30)$$

we obtain a scattering probability p_{sc} of 14.8% for a spherical phase factor φ_{sp} , whereas the parabolic phase factor adopted in [1] only leads to a scattering probability of 2.6%.

3.3.3 Focusing field compatible with Maxwell equations

In the last section, we showed that adoption of the spherical phase factor $\varphi_{sp}(\rho)$ predicts a higher intensity at the focus. However, an initial outgoing field modeled with the help of Eqn. 3.21 is not compatible with Maxwell equations since the reconstructed outgoing field $\vec{F}_{out}(\vec{r})$ obtained through Eqns. 3.22 and 3.23 has non-vanishing \hat{z} and \hat{e}_- components at $z = 0^+$ even though the initial outgoing field we start with only has the \hat{e}_+ component. Such discrepancies are negligible for small w_L , but become very large for large incident beam waist w_L .

To be more precise, the reconstructed field (Eqn. 3.22) must satisfy Maxwell equations since it is a linear combination of \vec{F}_ν , which themselves are the solutions of source-free Maxwell equations. If the reconstructed field is not identical to the initial field, then the initial field cannot satisfy Maxwell equation, and vice versa. Therefore, Eqn. 3.21 cannot be physical.

In view of this, we model the field right after the lens by considering changes in local polarization of the field on top of using the spherical phase factor with three requirements in mind. The requirements are:

1. A rotationally symmetric lens does not alter the local azimuthal field component, and only tilts the local radial polarization component of the incoming field towards the axis;
2. The polarization at point P (see Fig. 3.2) after transformation by the lens should be orthogonal to the line FP to form a spherical wave front;

3. The power flowing into and out of an arbitrarily small area on the thin ideal lens is the same.

These requirements are identical to the assumptions made by Richards and Wolf on the transformation of polarization of optical rays by optical elements [104]. With these requirements, we model the field right after the lens as ⁵

$$\begin{aligned} \vec{F}_{\text{out}}(\rho, \phi, 0) &= \frac{1}{\sqrt{\cos \theta}} \left(\frac{1 + \cos \theta}{2} \hat{e}_+ + \frac{\sin \theta e^{i\phi}}{\sqrt{2}} \hat{z} + \frac{\cos \theta - 1}{2} e^{2i\phi} \hat{e}_- \right) \times \\ &\times \exp(-\rho^2/w_L^2) \exp \left[-ik(\sqrt{\rho^2 + f^2} - f) \right], \end{aligned} \quad (3.34)$$

where the $\frac{1}{\sqrt{\cos \theta}}$ term is due to the third criterion, and can be understood by noting the difference in the Poynting vectors of local fields before ($z = 0^-$) and after ($z = 0^+$) the lens. The expansion coefficient κ_μ becomes

$$\begin{aligned} \kappa_\mu &= \delta_{m1} \pi k_t \int_0^\infty d\rho \rho \frac{1}{\sqrt{\cos \theta}} \left\{ \frac{sk + k_z}{k} \left(\frac{1 + \cos \theta}{2} \right) J_0(k_t \rho) + i \frac{\sqrt{2} k_t}{k} \left(\frac{\sin \theta}{\sqrt{2}} \right) J_1(k_t \rho) \right. \\ &\quad \left. + \frac{sk - k_z}{k} \left(\frac{\cos \theta - 1}{2} \right) J_2(k_t \rho) \right\} \exp \left[-ik(\sqrt{\rho^2 + f^2} - f) - \frac{\rho^2}{w_L^2} \right], \end{aligned} \quad (3.35)$$

⁵**Transformation of local polarization:** To obtain the local polarization of the focusing field in Eqn. 3.34, we consider an arbitrary point P($\rho, \phi, 0$) before the lens and an incident light field with polarization

$$\hat{e}_{\text{in}} = \hat{e}_+ = \frac{\hat{x} + i\hat{y}}{\sqrt{2}}, \quad (3.31)$$

or in the cylindrical basis,

$$\hat{e}_{\text{in}} = \frac{e^{i\phi}}{\sqrt{2}} \hat{\rho} + \frac{ie^{i\phi}}{\sqrt{2}} \hat{\phi}, \quad (3.32)$$

where $\hat{\rho} = \cos \phi \hat{x} + \sin \phi \hat{y}$ and $\hat{\phi} = -\sin \phi \hat{x} + \cos \phi \hat{y}$ are two unit vectors along the radial and azimuthal directions respectively. The ideal lens leaves the azimuthal component unchanged but tilts the radial component such that the local polarization of the field right after the lens is perpendicular to the line FP in Fig. 3.2 (F is the focus point), that is:

$$\begin{aligned} \hat{e}_{\text{out}} &= \left(\frac{\cos \theta e^{i\phi}}{\sqrt{2}} \hat{\rho} + \frac{\sin \theta e^{i\phi}}{\sqrt{2}} \hat{z} \right) + \frac{ie^{i\phi}}{\sqrt{2}} \hat{\phi} \\ &= \frac{1 + \cos \theta}{2} \hat{e}_+ + \frac{\sin \theta e^{i\phi}}{\sqrt{2}} \hat{z} + \frac{\cos \theta - 1}{2} e^{2i\phi} \hat{e}_-. \end{aligned} \quad (3.33)$$

where $\theta = \tan^{-1}(\rho/f)$. The Kronecker symbol δ_{m1} indicates that the angular momentum of the incident light beam is conserved under the new transformation we use [105, 106]. Finally, we determine the complete outgoing field with three polarization components defined by $F_+ \equiv \vec{F}_{\text{out}} \cdot \hat{\epsilon}_+^*$, $F_z \equiv \vec{F}_{\text{out}} \cdot \hat{z}$, and $F_- \equiv \vec{F}_{\text{out}} \cdot \hat{\epsilon}_-^*$, where

$$F_+(\rho, \phi, z) = \sum_{s=\pm 1} \int_0^k dk_t \frac{1}{4\pi} \frac{sk + k_z}{k} J_0(k_t \rho) e^{ik_z z} \kappa_{\mu=(k_t, 1, s)}, \quad (3.36)$$

$$F_z(\rho, \phi, z) = \sum_{s=\pm 1} \int_0^k dk_t (-i) \frac{\sqrt{2} k_t}{4\pi k} J_1(k_t \rho) e^{ik_z z} e^{i\phi} \kappa_{\mu=(k_t, 1, s)}, \quad (3.37)$$

$$F_-(\rho, \phi, z) = \sum_{s=\pm 1} \int_0^k dk_t \frac{1}{4\pi} \frac{sk - k_z}{k} J_2(k_t \rho) e^{ik_z z} e^{2i\phi} \kappa_{\mu=(k_t, 1, s)}. \quad (3.38)$$

We now consider a set of parameters, say $f = 4.5$ mm, $\lambda = 780$ nm, and $w_L = 7$ mm, for which the incident beam is strongly focused by the lens. We reconstruct the outgoing field at $z = 0$ using Eqns. 3.36, 3.37, and 3.38 and compare it to the starting output field given by Eqn. 3.34. Figure 3.4a shows (from top to bottom) the reconstructed $|F_+|$, $|F_z|$ and $|F_-|$ at $z = 0$. As the reconstructed fields overlap visually with the polarization corrected field behind the lens, the original field distributions are not shown. Quantitatively, the relative difference between the original and reconstructed field ⁶ is less than 10^{-3} , a bound limited by our numerical accuracy. For comparison, the reconstructed fields obtained using φ_{sp} without polarization correction are shown in Fig. 3.4b. The reconstructed fields at $z = 0$ are not the same as the original fields $|F_0|$ we start with. A successful reconstruction, therefore, shows that our extended model (Eqn. 3.34) is physical (compatible with Maxwell equations) even for very strong focusing.

3.3.4 Field at the focus

Having found a field compatible with Maxwell's equations and with a focusing spherical wave front, we can now examine the field at the focus in more

⁶Here, the relative difference between two field vectors \vec{v}_1 and \vec{v}_2 is defined as $\frac{|\vec{v}_2 - \vec{v}_1|}{|\vec{v}_1|}$.

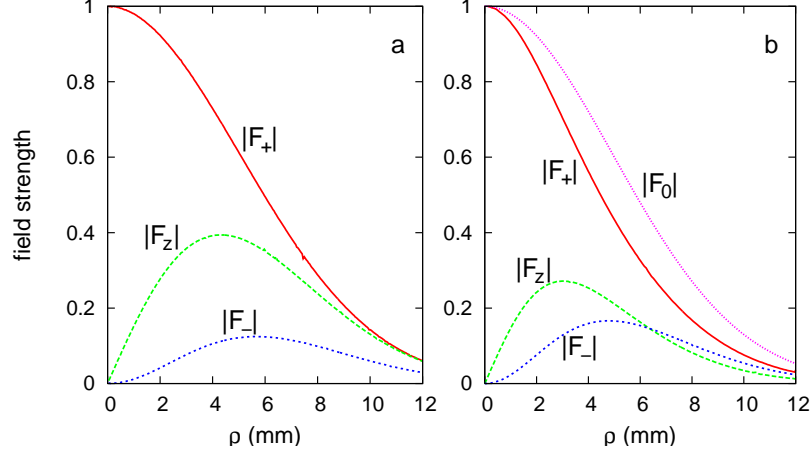


Figure 3.4: Absolute field strengths after the ideal lens reconstructed from the expansion into cylindrical components at $z = 0$ obtained with parameters: $f = 4.5$ mm, $\lambda = 780$ nm, and $w_L = 7$ mm. (a) Polarization-corrected outgoing field given by Eqn. 3.34. (b) Only with spherical wave front phase factor φ_{sp} , no polarization correction. The traces in the figure (b) are: the amplitude of the original \hat{e}_+ -polarized field $|F_0|$, and the reconstructed field strengths $|F_+|$, $|F_z|$ and $|F_-|$.

detail. Figure 3.5 shows the field at the focal plane for different focusing strengths obtained with this model. Every individual plot in the figure assumes the same focal length ($f = 4.5$ mm) and wavelength ($\lambda = 780$ nm), but different incident waists w_L . In each plot, we show the absolute field strengths $|F_+|$, $|F_z|$, and $|F_-|$, together with the field predicted using the paraxial approximation given by

$$\vec{F}_{\text{focus}}^{\text{parax}} = \frac{w_L}{w_f} \exp\left(-\frac{\rho^2}{w_f^2}\right) \hat{e}_+, \quad (3.39)$$

with a paraxial focal waist

$$w_f = f\lambda/\pi w_L. \quad (3.40)$$

For weak focusing, $|F_+|$ overlaps completely with the paraxial prediction with negligible $|F_z|$ and $|F_-|$ (Fig. 3.5a). When $w_f \simeq 3.7 \mu\text{m}$ (about 5λ), discrepancies between paraxial approximation and the extended model start to appear (Fig. 3.5b). The \hat{z} - and \hat{e}_- - polarized fields become stronger as w_L increases. However, they never appear on the lens axis. Therefore, an atom localized on the lens axis would only experience the \hat{e}_+ - polarized field. Figure 3.5d shows the focusing that maximizes $|F_+|$ for these parameters in our model. It is obtained with a incident waist $w_L = 10 \text{ mm}$. Increasing the incident waist further does not make the focal spot smaller due to diffraction limit. Instead, more energy is transferred to the $|F_z|$ and $|F_-|$ side lobes, thus decreasing the magnitude of the $|F_+|$ component again. It is clear that the properties of the field around the focus vary significantly within a wavelength. Nevertheless, a localized single atom would still experience a field with a well defined polarization and amplitude because it is much smaller than the characteristic length scale of such variations.

Bassett [107] has established an upper bound to the field energy density which is attainable by passive concentration at any point G for a given input power [107]. He assumes that the point G is many wavelengths from any object and the light passes only once through the point (as opposed to the case of a cavity). He found that the ratio of the electric energy density at G to the total incident power has a maximum value given by [107, 108] ⁷

$$F_e^{\text{max}} = \frac{k^2}{6\pi c}, \quad (3.41)$$

where $k = 2\pi/\lambda$. In our notations, this ratio becomes

$$F_e = \frac{\epsilon_0 E_A^2 / 4}{P_{\text{in}}} = \frac{1}{\pi c w_L^2} \left(\frac{E_A}{E_L} \right)^2, \quad (3.42)$$

where we have made use of Eqn. 3.6 for the incident power P_{in} . For the strongest focusing we have calculated with this model (Fig. 3.5d), $F_e \simeq 0.727 F_e^{\text{max}}$

⁷The maximum ratio of the total field energy density to the total incident power is $F^{\text{max}} = k^2/3\pi c$. The total field energy density includes the magnetic field and electric field energy densities, each contributing half to the total field energy density on the lens axis due to symmetry of our system [108].

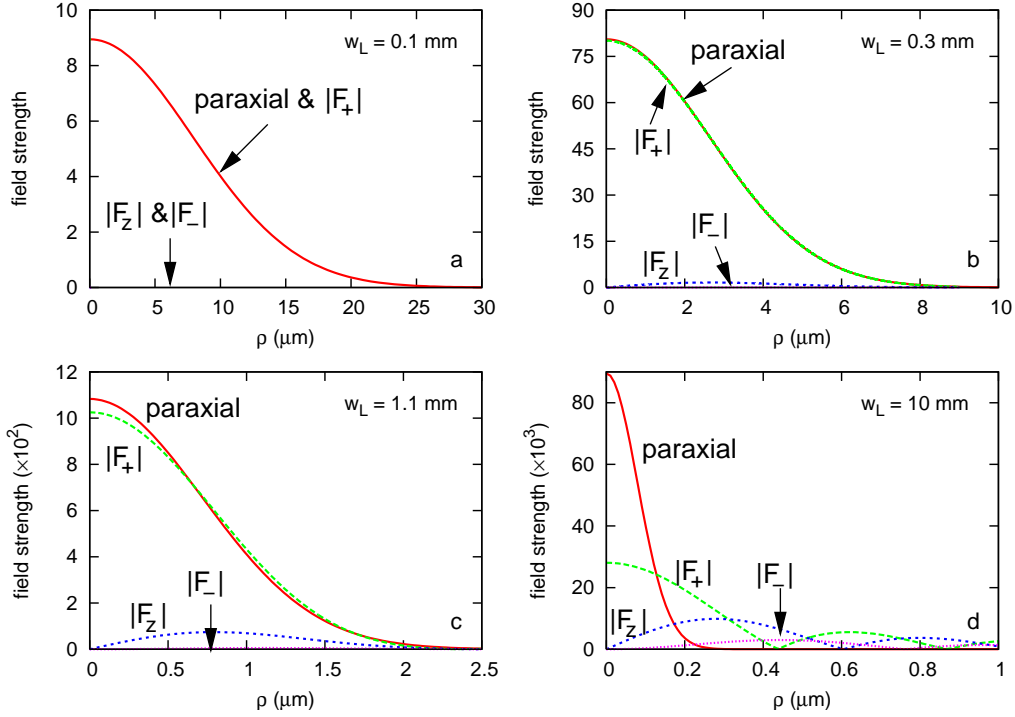


Figure 3.5: Absolute field strengths at the focus for different focusing strengths. Different plots are obtained with the same focal length of 4.5 mm and wavelength of 780 nm, but with different input waists w_L .

at the focus of the lens. This shows that the focusing field modeled by Eqn. 3.34 is able to give rise to a field concentration comparable to the strongest field concentration allowed in a free space operation.

It should also be noted that a strongly focused field does not have a planar wave front at the focus. This can be understood from the fact that

$$F_z(\rho, \phi, z) = F_z(\rho, z)e^{i\phi}, \text{ and } F_-(\rho, \phi, z) = F_-(\rho, z)e^{2i\phi}, \quad (3.43)$$

which means that the phase of the field on the focal plane $z = f$ is not uniform (Eqns. 3.37 and 3.38).

3.3.5 Obtaining the field at the focus using the Green theorem

To verify the validity of the above calculations, we adopt a different method to calculate the field at the focal point. For an aplanatic focusing field, one can conveniently obtain the focal field strength using the Green theorem [109]:

$$\begin{aligned} \vec{E}(\vec{r}) = \oint_{S'} da' & \left\{ ikc \left[\vec{n}' \times \vec{B}(\vec{r}') \right] G + \left[\vec{n}' \times \vec{E}(\vec{r}') \right] \times \nabla' G \right. \\ & \left. + \left[\vec{n}' \cdot \vec{E}(\vec{r}') \right] \nabla' G \right\}, \end{aligned} \quad (3.44)$$

which means that the electric field $\vec{E}(\vec{r})$ at point \vec{r} can be obtained given the electric and magnetic fields ($\vec{E}(\vec{r}')$ and $\vec{B}(\vec{r}')$) on an arbitrary closed surface S' that encloses the point \vec{r} . Here, \vec{n}' is the unit vector normal to a differential surface element da' and points into the volume enclosed by S' , and G is the Green function given by

$$G = \frac{e^{ik|\vec{r}-\vec{r}'|}}{4\pi|\vec{r}-\vec{r}'|}. \quad (3.45)$$

If point \vec{r} is the **focus** of an aplanatic focusing field, then the local field propagation wavevector \vec{k}' at any point \vec{r}' always points towards (away from) point \vec{r} for the incoming (outgoing) field in the far field limit, i.e. when $|\vec{r}-\vec{r}'| \gg \lambda$. In this limit, one has

$$B(\vec{r}') \rightarrow \frac{\vec{k}'}{c|\vec{k}'|} \times E(\vec{r}'), \quad (3.46)$$

$$\nabla' G \rightarrow -i\vec{k}'G \text{ before the focus, } \nabla' G \rightarrow i\vec{k}'G \text{ after the focus.} \quad (3.47)$$

Eqn. 3.44 reduces to

$$\begin{aligned} \vec{E}(\vec{r}_{\text{aplanatic}}^{\text{focus}}) &= -2i \int_{S_{\text{bf}}} da' \left[\vec{n}' \cdot \vec{k}' \right] \vec{E}(\vec{r}') G \\ &+ 2i \int_{S_{\text{af}}} da' \left[\vec{n}' \cdot \vec{E}(\vec{r}') \right] \vec{k}' G. \end{aligned} \quad (3.48)$$

Here the surface S' is divided into two regions. S_{bf} is the region before the

focal plane S_{bf} and S_{af} is the surface after the focal plane. The second term in Eqn. 3.48 is zero if we choose S_{af} to be an infinitely large semisphere centered at the focus, since in this case \vec{n}' is perpendicular to $\vec{E}(\vec{r}')$ at all points on S_{af} for an aplanatic field. If we choose S_{bf} as an infinitely large plane that coincides with the ideal lens and adopt the incident field given by Eqn. 3.34, Eqn. 3.48 becomes

$$\vec{E}(0, 0, z = f) = \frac{-ik\sqrt{f}}{2} \int_0^\infty d\rho \frac{\rho(f + \sqrt{f^2 + \rho^2})}{(f^2 + \rho^2)^{5/4}} \exp\left(-\frac{\rho^2}{w_L^2}\right) \hat{e}_+ \quad (3.49)$$

which has an analytical solution of

$$\vec{E}(0, 0, z = f) = \frac{-ik\sqrt{fw_L}}{4} \exp\left(\frac{f^2}{w_L^2}\right) \left[\frac{f\Gamma\left(-\frac{1}{4}, \frac{f^2}{w_L^2}\right)}{w_L} + \Gamma\left(\frac{1}{4}, \frac{f^2}{w_L^2}\right) \right] \hat{e}_+, \quad (3.50)$$

where $\Gamma(a, b) = \int_b^\infty t^{a-1} e^{-t} dt$. The focal field strengths obtained by Eqn. 3.50 agree fully with the results obtained using the mode-decomposition method, within computational errors of about 0.1%. The $-i$ imaginary number reflects a Gouy phase of $-\pi/2$ [110].

3.4 Scattering Probability

With the knowledge of the field at the focus, we can now calculate the scattering probability of a light beam by a two level system. Figure 3.6 displays the scattering probability as a function of the incident waist w_L , obtained for focusing parameters $f = 4.5$ mm, $\lambda = 780$ nm. The curves in the figure are obtained using (from top to bottom) the paraxial approximation (Eqn. 3.39), spherical wave front with polarization correction (Eqn. 3.34), spherical wave front without polarization correction (Eqns. 3.21 and 3.25), and parabolic wave front without polarization correction (Eqns. 3.21 and 3.24). It is clear that adopting a parabolic wave front after the lens greatly reduces the scattering probability (φ_{pb} curve). With a spherical wave front, the scattering probability increases significantly especially for stronger focusing (φ_{sp} curve). However, as was pointed out in previous sections, modeling the output field

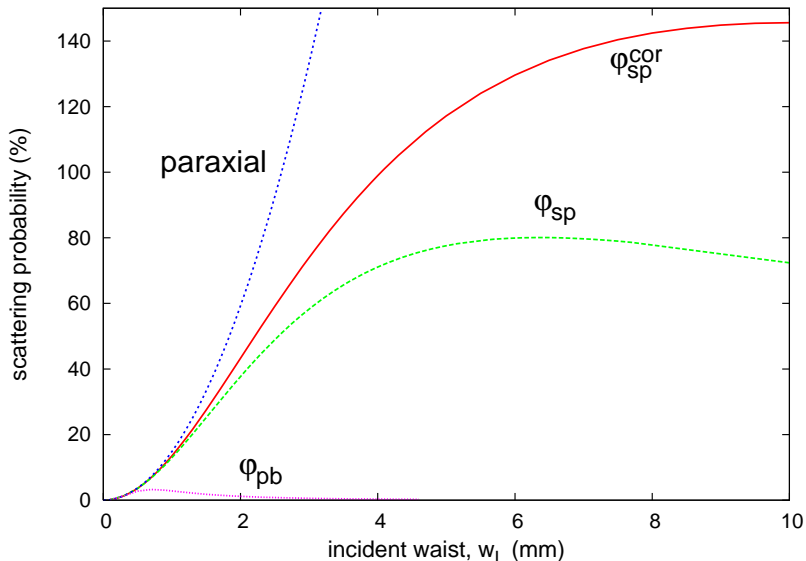


Figure 3.6: Scattering probability as a function of w_L obtained (from top to bottom) by assuming paraxial approximation, spherical wave front with polarization correction, spherical wave front without polarization correction, and parabolic wave front without polarization correction ($f = 4.5$ mm, $\lambda = 780$ nm).

without considering the action of the lens on the polarization of the field gives rise to an unphysical focusing field. Our attempt to construct a physical focusing field predicts even larger scattering probability compared to the previous models with a maximal value of $\simeq 145\%$ ($\varphi_{\text{sp}}^{\text{cor}}$ curve). It should be noted that all of the three models converge to the paraxial model for small w_L , with the parabolic model diverging most quickly and the physical field model diverging last.

Now, a scattering probability of more than 100% seems to suggest a violation of energy conservation (i.e. power scattered by a two-level system is more than that of the incident probe). A simpler explanation is that we have made a mistake in our calculations. However, repeated checks have confirmed our results. Indeed, the scattering probability can be more than 100% if we assume the scattered power is given by Eqn. 3.9. Such results were obtained also in other works [111, 112]. In fact, a number of literatures have shown that there is no violation of energy conservation in this case

since the probe field and the forward scattered field interferes destructively, as was shown in [113, 114, 115] for the case of an incident plane wave, and by Zumofen et al. [111] for arbitrary incident fields with the help of vectorial multipole expansions [116, 117].

To provide more insights, Eqn. 3.9 represents the total power that would be emitted by a two-level atom that experiences an excitation field with an amplitude of E_A . This equation does not consider the origin (source) of the excitation field (which is the incident probe field in our discussion), and the possible interference between the emitted field and the excitation field⁸. By considering the interference between the scattered field and excitation field, the false impression that the power scattered by the atom is more than that of the incident field would not appear (see Appendix A.10). Admittedly, the notion of ‘scattering probability’ is thus not an appropriate one since this quantity can be more than one. One can think of using other notions, for example ‘scattering ratio’, but it would not avoid the energy-conservation paradox. Therefore, we purposely choose the notion of ‘scattering probability’ to highlight this ‘unexpected’ paradox.

From the experimental perspective, the scattering probability is a well defined physical quantity when the focusing strength of the probe is weak. In this regime, the solid angle subtended by the probe is small (say less than a few percents of the full solid angle). In principle, the power scattered by the atom can then be measured quite accurately. As the focusing strength of the probe increases, the scattering probability and the solid angle subtended by the probe beam also increase. In this case, one cannot accurately measure the total scattered power, since it is not possible to distinguish the forward scattered field and the excitation field within the solid angle subtended by the probe. Thus the ‘scattering probability’ becomes a less meaningful physical quantity. In the regime where the scattering probability is more than 1, the solid angle subtended by the probe would almost cover the full solid angle and the ‘scattered power’ cannot be measured. Therefore, the ‘scattering probability’ loses its original simple interpretation in this regime.

⁸Under a weak coherent excitation field, the field scattered by an atom is coherent with the excitation field [94].

Having discussed the shortcomings of physical interpretation of the scattering probability defined in Eqn. 3.2, we think that this quantity is still a useful quantity that reflects the interaction strength between a coherent field and an atom although it cannot be interpreted physically in the strong focusing regime. We note in passing that the largest scattering probability is 200% [111]. This result is determined by the Bassett limit [107]. In this limit, the probe field is completely reflected by the two-level system (see [111] for more details).

Coming back to our results, we emphasize that the maximum scattering probability of 145% is obtained with the focusing field defined by Eqn. 3.34. However, it is not known if one can ever construct a high numerical-aperture lens that gives rise to such focusing field. Therefore, we do not claim that such a high scattering probability can be achieved readily in an experiment. The more important message is that we have shown the possibility of achieving high interaction strength between a light beam and a single atom by focusing.

3.5 Conclusion

In this chapter, we theoretically investigated the interaction strength between a focused light field and a two-level atom. We began by defining the interaction strength as the scattering probability of the light beam by the atom. We then derived an general expression for the scattering probability by assuming a circularly polarized- monochromatic Gaussian light beam and a two-level atom localized on the lens axis. Finally, by constructing a physical focusing field with a spherical wave front and by computing the field at the focus, we show that a focusing light field can interact efficiently with a single atom in free space.

Chapter 4

Strong interaction of light with a single trapped atom

In this chapter, we present an experiment which demonstrates substantial extinction of a light beam by a single ^{87}Rb atom in free space. The strong extinction (up to 10%) allows us to measure the absorption spectra of the atom directly without using modulation amplification techniques. The absorption spectra measured clearly reveal the energy shifts in the ^{87}Rb atom caused by the trapping light, and have spectra widths limited by the lifetime of the atomic transition. The results of this work are published in [27].

Background

Since advent of lasers, the resolution and sensitivity of spectroscopic measurements have improved to the extent that the spectrum of a single quantum system can be measured. When it comes to spectroscopic measurements of single quantum systems, most experiments rely on fluorescence spectroscopy techniques [118]. However, direct absorption measurements would be desirable because they allow one to quantitatively access the optical polarizability. Earlier absorption spectroscopy experiments on single ions [119], molecules [120, 121], and quantum dots (nanocrystals) [122, 123] showed differential extinctions on the order of 10^{-5} to 10^{-4} , and made use of modulation ampli-

fication techniques. More recent experiments performed on single molecules and semiconductor quantum dots [124, 125, 126, 127] already saw a signal contrast from a few percent to 13%. The high signal contrast was made possible either by strongly confining the light field using small aperture [124, 125] or by tightly focusing the light field using solid immersion lenses [126, 127]. However, the results of these experiments do not show the actual extinction¹ of the excitation beam by the quantum systems. In usual extinction measurements, e.g. as implemented in a commercial spectrophotometer, the probe beam is fully collected by the power measuring device. However, this is not the case in previous extinction measurements performed on single quantum systems. The reason is that substantial extinction of a probe beam by a single quantum system generally requires strong focusing. It is, nevertheless, difficult if not impossible in most experiments to collect the strongly diverging probe fully after the focus. As such, the ‘extinction’ measured in these experiments is not the extinction in the usual sense and cannot be used in a straightforward way to quantify the actual scattering probability of the probe by the quantum system. In fact, the signals observed in these experiments [124, 125, 126, 127] were optimized using the interference between the light scattered by the quantum systems and **part** of the excitation light beam (See Section 4.7). The signature of such interference is revealed, for example, in [121, 123, 125, 126] as a ‘transmission’ of more than 100%, obviously violating energy conservation.

As our main task is to quantify the scattering probability of a light beam by a single atom, we design our setup to ensure that the extinction we measure is not enhanced by such interference effect. The main idea of our setup is to focus a weak and narrow bandwidth Gaussian light beam (probe) onto

¹There are different definitions of the extinction ϵ . In transmission spectroscopy, extinction is sometimes defined as $\epsilon = \log(1/T)$ or $\epsilon = 1 - T$, where $0 < T \leq 1$ is the transmission. In the scattering theory of light by small particles [78], extinction is equivalent to the sum of optical powers scattered and absorbed by the particle. In such a context, absorption refers to optical energy absorbed and transferred into heat by the particles. In recent single particle experiments [125, 126, 127], extinction is defined as $\epsilon = 1 - T$. We adopt this definition in this dissertation but we emphasize that T should be measured by fully collecting the probe. Only in this case, the measured extinction is a well defined quantity and can be used to quantify the scattering probability.

an optically-trapped single ^{87}Rb atom using a lens. The atom scatters part of the probe. The remaining part that is not scattered is fully collected by a second lens in the downstream direction, and delivered to a single photon detector. The fact that we measure the extinction by collecting all of the diverging probe after the focus allow us to set a lower bound to the scattering probability of the probe by the atom (see Section 3.1).

4.1 Setup for extinction measurement

Figure 4.1 shows the schematic diagram of our experiment. The heart of the setup consists of two identical aspheric lenses (full NA = 0.55, $f = 4.5$ mm), mounted in a confocal arrangement inside an ultra high vacuum chamber. The collimated Gaussian probe beam is first delivered from a single mode fiber, focused by the first lens, fully collected by the second lens, and finally coupled again into a single mode fiber connected to a Si-avalanche photodiode. A ^{87}Rb atom is trapped at the focus between the two lenses by means of a far-off-resonant optical dipole trap (FORT) formed by a light beam ($\lambda = 980$ nm) passing through the same lenses ². Cold atoms are loaded into the FORT from a magneto-optical trap (MOT) surrounding the FORT. The Si-avalanche photodiode D2 detects the fluorescence of the trapped atom exposed to the MOT beams (Fig. 4.1). It triggers the transmission measurement when an atom is loaded into the FORT. The Si-avalanche photodiode D1, on the other hand, measures the photon flux of the transmitted probe. We obtain the extinction of the probe beam by the atom through comparing the photocounts at D1 with and without the atom in the FORT.

²Using a tight FORT to trap a single atom was first demonstrated by Philippe Grangier's group at the Institut d'Optique in France. The main difference between our setup and theirs is the wavelength of the FORT. They adopted a 810 nm FORT [128]. The advantage of such a choice is that a smaller FORT power is needed to trap the atom since 810 nm is closer to the D2 transition of the ^{87}Rb atom. We chose a 980 nm FORT because it reduces the scattering of the FORT light by the atom, and thus reducing the disturbance on the atomic state. Our setup resembles closely that of Harald Weinfurter's group at LMU Munich. They adopt a 856 nm FORT light, and use a microscope objective (MO) located outside the vacuum chamber for fluorescence collection [129]. As there is a thick window (2.5 mm) between the trapped atom and the MO, the fluorescence collection efficiency of their setup is affected by aberrations.

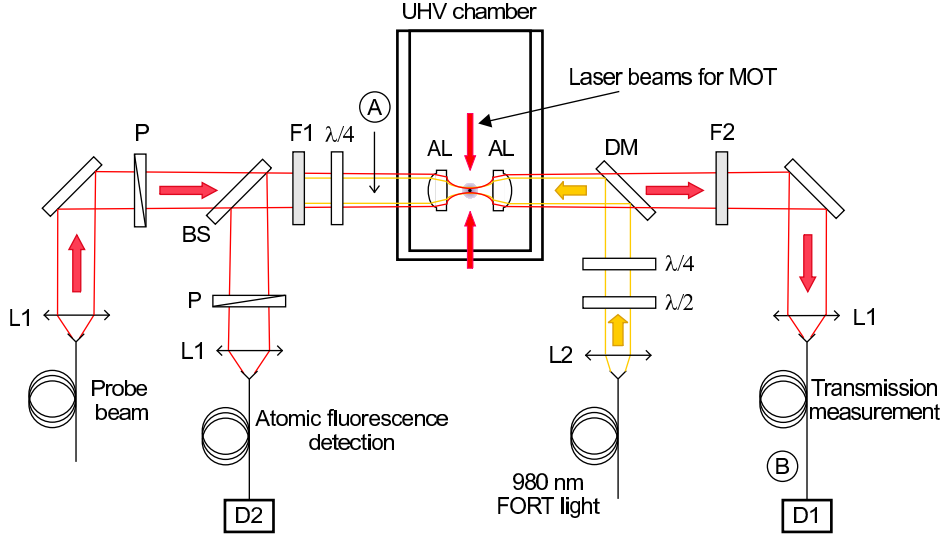


Figure 4.1: Experimental setup for measuring the extinction of a light beam by a single atom. AL: aspheric lens ($f = 4.5$ mm, full NA = 0.55), P: polarizer, DM: dichroic mirror, BS: beam splitter with 99% reflectivity, $\lambda/4$, $\lambda/2$: quarter and half wave plates, F1: filters for blocking the 980 nm FORT light, F2: interference filter centered at 780 nm, D1 and D2: Si-avalanche photodiodes. Four more laser beams forming the MOT lie in an orthogonal plane and are not shown explicitly (see Fig. 4.2).

As one would expect to observe maximum extinction for a clean two-level system with no other decay channels, we use a circularly polarized probe beam to optically pump the ^{87}Rb atom to a closed-cycling transition either between $|g+\rangle = |5S_{1/2}, F = 2, m_F = +2\rangle$ and $|e+\rangle = |5P_{3/2}, F' = 3, m_{F'} = +3\rangle$, or between $|g-\rangle = |F = 2, m_F = -2\rangle$ and $|e-\rangle = |F' = 3, m_{F'} = -3\rangle$ (Fig. 4.6). During the transmission measurement process, the atom may fall into the $(5S_{1/2}, F = 1)$ metastable ground states, which are off resonant to the probe. To bring it back to the pumping cycle, circularly polarized light resonant with the D1 transition is mixed into the probe beam, and later removed with an interference filter F2 (Fig. 4.1). We also use a circularly polarized FORT beam coaxial with the probe because this minimizes population leakage out of the two-level system (Section 4.4).

To facilitate further discussions on the extinction measurement, we will focus on some important properties of our system in the next few sections.

Section 4.2 provides more technical details of our setup. Section 4.3 presents the evidences showing that there is no more than one atom trapped in our FORT at any time. The effects of the FORT light and external magnetic field on the atom and their influence on the extinction measurement are discussed in Section 4.4. Section 4.5 explains how we measure the extinction of the probe caused by the atom in the FORT. Finally, we present and discuss our experimental results in Section 4.6, 4.7, and 4.8.

4.2 Technical details of the setup

This section provides a detailed technical description of our setup.

Aspheric lenses

An aspheric lens is a simple single element replacement for multi-element microscope objectives. It is normally designed to focus a colimated beam into a diffraction limited spot. Thus, a collimated light beam focused by an aspheric lens should have a spherical wave front after the lens, thereby creating a focusing field closer to that described by Eqn. 3.34. Besides, an aspheric lens has a much lower reflection loss than a microscope objective. It is also more suitable for an ultra-high vacuum system than a microscope objective, since trapped air pockets and glue used in the commercial microscope objectives might cause problems during pumping down of the vacuum chamber.

The two identical aspheric lenses used to focus and recollect the probe beam in our experiment are manufactured by LightPath Technologies, Inc. (catalogue number 350230). They are designed to colimate a 780 nm diode laser. The lenses have a back focal length (working distance) of 2.91 mm. To arrange the lenses confocally, the distance between the two lenses is fixed at 5.82 ± 0.02 mm (the uncertainty is due to the machining accuracy of the lens holder). The lenses are near infrared anti-reflection coated and have a clear aperture of 4.95 mm.

Magneto-optical trap

We use a three-dimensional magneto-optical trap (MOT) [130, 131, 132] to cool and gather a cloud of ^{87}Rb atoms around the FORT. The MOT consists of (i) three pairs of light beams (MOT beams) for cooling and exerting a scattering force on the ^{87}Rb atoms, (ii) two square anti-Helmholtz coils for generating a magnetic quadrupole field at the center of the trap, and (iii) three pairs of Helmholtz coils for adjusting the magnetic field in the trap (Fig. 4.2). One pair of MOT beams lie horizontally along the X-axis. The other two pairs lie in the YZ-plane, both at an angle of 20° from the vertical Y-axis due to the space constraint imposed by the lenses. The anti-Helmholtz coils are placed coaxially along the X axis. They provide magnetic field gradients of $\simeq 7 \text{ Gauss cm}^{-1}$ along the X axis, and $\simeq 3.5 \text{ Gauss cm}^{-1}$ along both the Y and Z axes at the center of the trap. The other three pairs of Helmholtz coils are placed along the X, Y and Z axis respectively. They are used to zero the magnetic field at the center of the MOT before an atom is loaded into the FORT, and to apply a $\simeq 2 \text{ Gauss}$ magnetic bias field along the Z-axis after an atom is loaded into the FORT during the extinction measurement (Section 4.4).

The MOT beams

Each MOT beam consists of a 780 nm cooling light and a 795 nm repump light, both circularly polarized. The cooling light is 24 MHz red detuned ($\delta = -4\Gamma$) from the $(5\text{S}_{1/2}, F = 2) - (5\text{P}_{3/2}, F' = 3)$ transition of the ^{87}Rb atom (see Appendix A.4 for the energy levels of the ^{87}Rb atom). Its purpose is to Doppler cool and trap the ^{87}Rb atoms [100, 133, 134, 135, 136, 137]. The repump light is resonant with the $(5\text{S}_{1/2}, F = 1) - (5\text{P}_{1/2}, F' = 2)$ transition. Its main purpose is to optically pump the atoms back to the $(5\text{S}_{1/2}, F = 2)$ ground state in case the atoms fall into the inaccessible ground state $(5\text{S}_{1/2}, F = 1)$ [132].

Both the cooling and repump light beams are obtained from grating-stabilized extended-cavity diode lasers [138, 139, 140, 141]. The linewidth of each laser is less than 600 kHz with a long term central-frequency stability

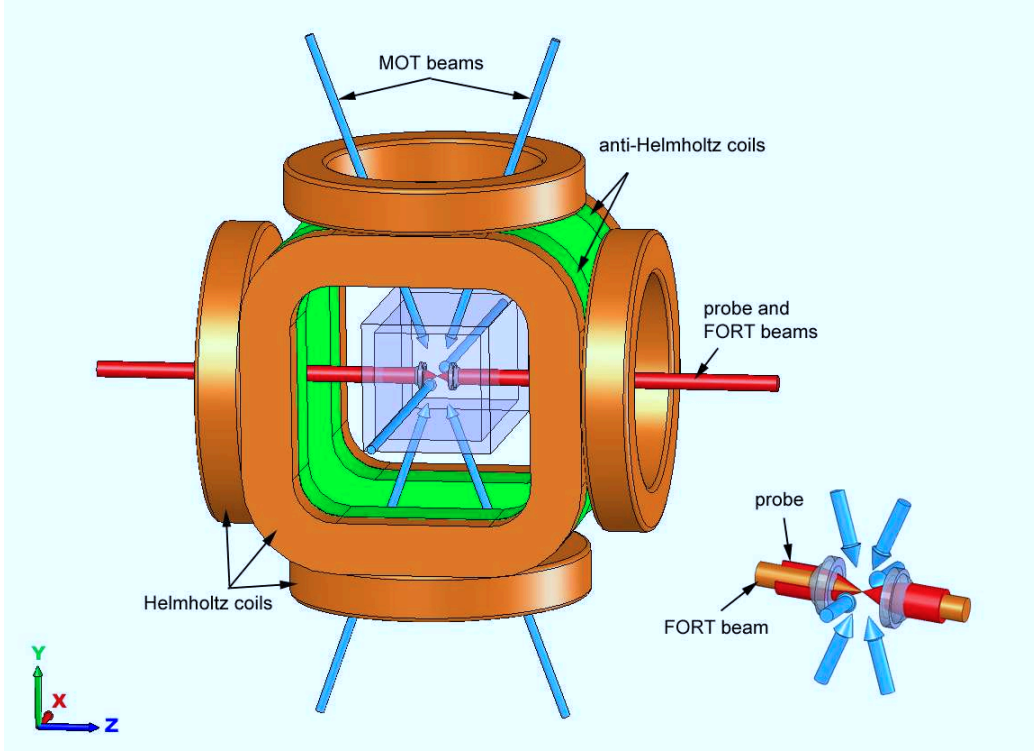


Figure 4.2: The core of the setup including a magneto-optical trap, a cuvette attached to a vacuum chamber, the aspheric lenses, and the relevant light beams used for trapping the atom and performing the extinction experiment (the lens holder in the cuvette is not shown for clarity). The inset is a zoom in near the center of the lens system. The picture is drawn to scale.

of about 1 MHz. The cooling light is initially locked to the $(5S_{1/2}, F = 2) - (5P_{3/2}, F' = 1)$ transition using frequency-modulation (FM) spectroscopy [142, 143], and then up shifted by 400 MHz using an acousto-optic modulator (AOM) in a double pass configuration [144]. The repump light is locked to the crossover [100] between the $(5S_{1/2}, F = 1) - (5P_{1/2}, F' = 1)$ transition and the $(5S_{1/2}, F = 1) - (5P_{1/2}, F' = 2)$ transition, and then up shifted by 408 MHz again using an AOM in a double pass configuration.

In our setup, a circularly polarized MOT beam is first delivered from a single mode fiber, sent through the vacuum chamber, reflected by a mirror with a quarter waveplate in front, and finally coupled back into the single mode fiber to form a pair counterpropagating MOT beams. Owing to reflec-

tion losses caused by the uncoated vacuum chamber, each MOT beam is not collimated but slightly focused in order to give rise to the same intensity at the center of the MOT for both the forward and back-reflected beams. The waists of the beams at the center of the MOT thus range from 0.5 mm to 0.8 mm. We typically use a cooling light power of $\simeq 100 \mu\text{W}$ for each pair of MOT beams. The powers of the repump light in different MOT beams are not equal but this is not crucial. A total power of $\simeq 65 \mu\text{W}$ of repump light is typically used. With such a setup, we obtain a ^{87}Rb -atom cloud with an approximate diameter of 0.4 mm.

Probe beam

The probe for the extinction measurement is derived from the same diode laser setup as the MOT cooling light, and thus has the same linewidth and stability as that of the cooling light. It goes through another double-pass AOM setup, allowing us to tune its frequency independently of the MOT cooling light. The largest incident waist of the probe that we can reliably use for the extinction measurement is about 1.4 mm before we start seeing a large distortion of the probe after the second aspheric lens due to the limited NA of the lenses (see Section 4.7). Such incident waist corresponds to a focal waist of $\simeq 0.80 \mu\text{m}$ ³.

Far-off-resonant optical dipole trap (FORT)

When choosing a FORT wavelength, one needs to estimate (i) the power of the light source needed to create a reasonable trapping depth (typically of a few mK), and (ii) the scattering rate of the FORT light by the atom. The depth of the FORT is approximately proportional to I/δ (Eqn. A.19), where δ is the detuning of the FORT light from the D2 transition of the ^{87}Rb atom, and I is the intensity at the focus. Therefore, using a further detuned FORT light typically requires a FORT laser with a larger power. On the other hand, adopting a far detuned FORT light reduces the scattering rate of the FORT

³All focal waists of the probe here are estimated using the paraxial approximation. (See Section 3.3.4)

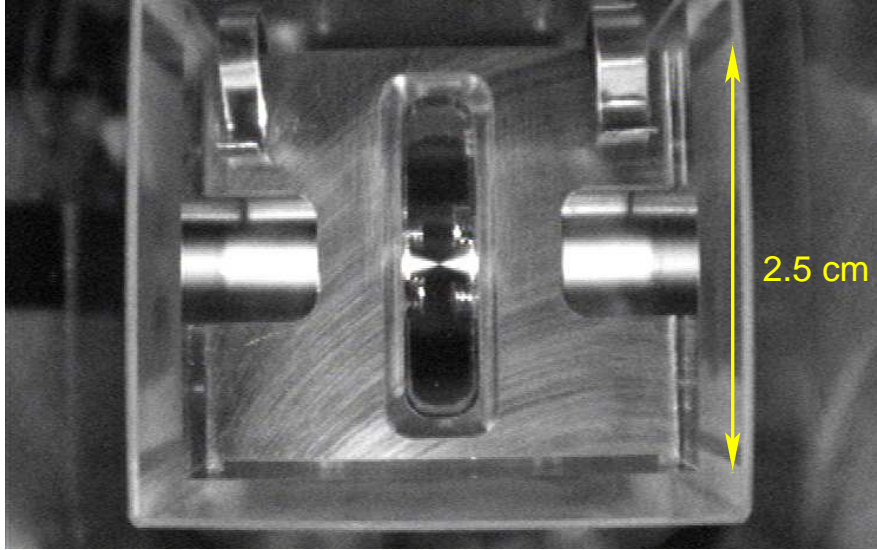


Figure 4.3: Photograph of the probe beam passing through the two aspheric lenses. The bright white beam is due to fluorescence of Rubidium atoms.

light by the atom which is roughly proportional to I/δ^2 (Eqns. A.11 and A.13). This is useful if we want to reduce the influence of the FORT on the atomic state. We have chosen a FORT wavelength of 980 nm because of the low scattering rate it introduces and the availability of 980 nm single-mode diode lasers that can supply a power up to 300 mW.

In our setup, the 980 nm diode laser is temperature stabilized without an external cavity. The FORT light decreases the ground state energy of the ^{87}Rb atom, forming a trap for the atoms at its focus. However, the FORT cannot trap an atom by itself because it is a conservative potential well. An atom that falls into a FORT experiences a decrease in potential energy but an increase in kinetic energy. The atom is trapped if the surrounding MOT cooling molasses ⁴ manages to remove the extra kinetic energy from the atom before it escapes from the FORT [100, 136, 145, 146].

A very tight FORT is important for our experiment because we need to localize the atom to a region much smaller than the wavelength of the probe

⁴The FORT has a size smaller than a few microns. The atom does not experience noticeable variation in the Zeeman shift within such a small region. In this case, the MOT essentially acts as molasses to the atoms.

in order to achieve maximum scattering (Section 3.3.4). The largest FORT focal waist we used in the experiment is $\simeq 2 \mu\text{m}$ ⁵. For this waist, the power of the FORT light is stabilized to $\simeq 33 \text{ mW}$, creating a trapping potential depth of approximately $h \cdot 27 \text{ MHz}$ (equivalent to $k_B \cdot 1.3 \text{ mK}$) at the center of the FORT. With such an intensity, we expect the off-resonant scattering rate of the FORT light by the atom to be about $10 \text{ photons s}^{-1}$ [145]. When adopting a smaller FORT focal waist of $\simeq 1.4 \mu\text{m}$, we reduced the power of the FORT beam such that the intensity at the location of the atom is approximately the same as in the previous case, thereby keeping the trap depth and off-resonant scattering rate unchanged.

Using the paraxial approximation, we can describe the spatial distribution of the FORT potential by

$$U(\rho, z) = -\frac{U_0}{(1 + z^2/z_R^2)} \exp\left[-\frac{2\rho^2}{w_D^2(1 + z^2/z_R^2)}\right], \quad (4.1)$$

where w_D is the waist of the FORT, and $z_R = \pi w_D^2/\lambda$ denotes the Rayleigh length. If the mean kinetic energy $k_B T$ of an atom⁶ is much smaller than the potential depth U_0 , the atom oscillates near the bottom of the potential. In this case, the FORT potential can be approximated by

$$U(\rho, z) = -U_0 \left[1 - 2 \left(\frac{\rho}{w_D} \right)^2 - \left(\frac{z}{z_R} \right)^2 \right]. \quad (4.2)$$

The oscillation frequencies of a trapped atom are given by $\omega_\rho = (4U_0/mw_D^2)^{1/2}$ in the radial direction, and $\omega_z = (2U_0/mz_R^2)^{1/2}$ in the axial direction, where m is the mass of the ^{87}Rb atom. For a trap depth $U_0 = k_B \cdot 1.3 \text{ mK}$ and a beam waist of $w_D = 1.4 \mu\text{m}$, the oscillation frequencies are approximately $\omega_\rho/2\pi = 80 \text{ kHz}$ and $\omega_z/2\pi = 13 \text{ kHz}$.

⁵The reported focal waists of the FORT are estimated using the paraxial approximation. More accurate measurements of the trap size and depth, not performed here, are possible [147].

⁶There is only one atom in our FORT. The temperature here reflects the statistical average of the atomic kinetic energy in the FORT.

Overlapping the foci of the probe and the FORT

The fact that the FORT light and the probe pass through the same set of identical lenses allows convenient overlapping of the foci of the two light fields. To overlap the foci longitudinally (along the lens axis), we first adjust the divergence of the probe such that the probe waists, before and after the vacuum chamber, are the same at an equal distance from the center of the lenses. We then repeat the same procedure for the FORT beam. We estimate the longitudinal overlap of the foci to be better than $\simeq 1.3 \mu\text{m}$ ⁷. To overlap the foci transversely, we make sure that the axis of the probe beam and that of the FORT beam coincide transversely better than $15 \mu\text{m}$ at a point about 10 cm from the vacuum chamber, and better than 0.15 mm at 7.5 meters away from the setup with the help of a CCD camera. Such requirements translate into a focal transverse coincidence of better than 90 nm for the two light fields. The fact that the longitudinal overlap is much worse than the transverse overlap does not significantly affect our experiment because the focal field varies less quickly along the longitudinal direction than along the transverse direction (See Figs. 3.3 and 3.5c). More precise alignment would be needed if one focuses the probe more strongly.

The vacuum system

An uncoated cuvette⁸ that contains an aluminum lens holder is glued to a vacuum chamber using low vapor-pressure epoxy (Torr Seal resin sealant, Variance, Inc.). The vacuum chamber, which is pumped solely with an 24 l/s ion getter pump, has a residue pressure of $\simeq 2.5 \times 10^{-9}$ Torr⁹ after bake-out. As the temperature of the residue gases in the chamber (higher than 300 K) is much larger than the depth of the FORT (1.3 mK), any collision between the trapped atom and a background atom kicks to the trapped atom out of

⁷The accuracy is limited by the sensitivity of our collimating lens-system in controlling the divergence of the beams.

⁸The cuvette was obtained from the Hellma GmbH & Co. It has outer dimensions of $3 \times 3 \times 7$ cm with a wall thickness of 2.5 mm.

⁹This pressure was measured with the Rb dispenser turned off.

the FORT. This loss mechanism limits the $1/e$ trapping time of the atom to about 2 seconds.

4.3 Trapping a single atom

Besides tightly confining the trapped atom, a small FORT ensures a single atom occupancy of the FORT at any time due to the collisional blockade mechanism [128, 148]. Such a blockade mechanism comes from the fact that two atoms in a very tiny trap can undergo light-assisted inelastic collisions efficiently, leading to the immediate loss of both atoms from the trap [146, 149]. Three main exoergic collisional processes in MOTs have been identified [149]: the fine-structure-changing collision (FCC) is represented by $A + A + \hbar\omega \rightarrow A_2^*(P_{3/2}) \rightarrow A^*(P_{1/2}) + A + \Delta E_{FCC}$ with the energy ΔE_{FCC} transferred to each atom. Here A and A^* refer to an atom in the ground state and in the excited state respectively. For Rb atoms, $\Delta E_{FCC}/k_B \approx 350$ K, thus FCC collisions cause an escape of both atoms from the FORT normally of a few mK deep. For radiative escape (RE), spontaneous emission of a photon redshifted from the atomic resonance takes place during the collision. The process is described by $A + A + \hbar\omega \rightarrow A_2^* \rightarrow A + A + \hbar\omega'$ with an energy of $\hbar(\omega - \omega')$ transferred to the two atoms. The resulting kinetic energy is continuously distributed and the corresponding loss rate is sensitive to the trap depth. Exoergic hyperfine-changing collisions (HCCs) on the molecular ground state can also lead to losses. For ^{87}Rb , a change from $(5S_{1/2}, F = 2)$ to $(5S_{1/2}, F = 1)$ in one of the colliding atoms transfers about $\Delta E_{HCC}/2k_B \simeq 0.16$ K to each atom.

A typical way of determining the number of atoms in a trap is to observe the amount of atomic fluorescence from the trap. When the number of atoms N in the trap is small, the amount of detected fluorescence f shows clear discrete behaviour represented by $f = Nr + b$, where r is the amount of detected fluorescence from one atom, and b the background noise. Such multiple-step fluorescence signal has been observed, for example, in a MOT with very a high magnetic field gradient of 375 G/cm [150] and a FORT with a focal waist of 5 μm [149, 151]. For a much tighter FORT, the fluorescence

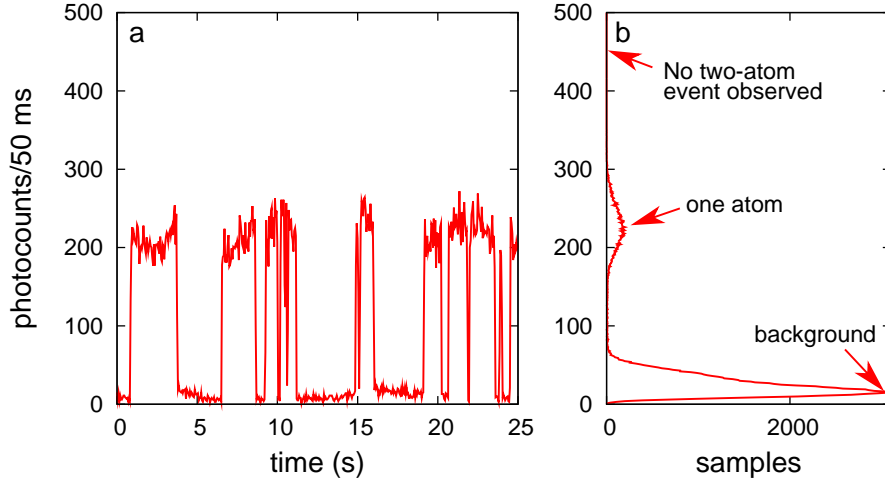


Figure 4.4: (a) Typical photocounts of fluorescence from the FORT observed with the avalanche photodiode D2. The photocounts hop between two levels, signifying an atom entering and leaving the FORT. (b) The histogram of the photocounts over a data taking period of 5000 s. The absence of the two-atom peak provides evidence that there is at most one atom in the FORT at all time.

signal jumps only between the background noise level and a higher level (Fig. 4.4), hinting that there can only be one or no atom in the FORT at any time [128, 129].

However, the observation of a binary on/off fluorescence signal does not rule out the possibility that two atoms always enter and leave the trap simultaneously. A more conclusive method to show the single atom occupancy of the trap is measure the second-order correlation in the fluorescence from the trapped atoms. The second-order correlation function [99] defined classically in terms of the fluorescence intensity $I(t)$ is given by

$$g^{(2)}(\tau) = \frac{\langle I(t)I(t+\tau) \rangle}{\langle I(t) \rangle^2}, \quad (4.3)$$

where the angle brackets denote averaging over time t . For any real light

source correlations always vanish at very long delay $\tau \rightarrow \infty$ and hence we have $\langle I(t)(t + \tau) \rangle \rightarrow \langle I(t) \rangle \langle I(t) \rangle$ and $g^{(2)} \rightarrow 1$. At time scales τ of characteristic intensity fluctuations, $g^{(2)}(\tau)$ shows deviations from unity. For any classical light field, $g^{(2)}(\tau)$ obeys the inequality [152]

$$g^{(2)}(0) \geq 1 \quad (4.4)$$

and

$$g^{(2)}(\tau) \leq g^{(2)}(0). \quad (4.5)$$

In terms of photon language $g^{(2)}(\tau)$ describes the conditional probability of detecting a second photon at a time τ after a first one was detected at $t = 0$ [153, 154]. The resonance fluorescence of a single atom is not classical because its $g^{(2)}(\tau)$ violates both Eqns. 4.4 and 4.5. After the emission of the first photon, the atom is in its ground state and cannot emit a second photon immediately, i.e. $g^{(2)}(0) = 0$. The fluorescence from more than one atom does not show complete antibunching because the emission of the first photon from an atom does not prevent the emission of a second photon from a different atom. When the fluorescence is collected from a large solid angle, the correlation function $g_N^{(2)}$ from N atoms is related to the single-atom $g^{(2)}$ by [99, 150]

$$g_N^{(2)}(\tau) = \frac{1}{N} [g^{(2)}(\tau) + (N - 1)]. \quad (4.6)$$

If there are $N > 1$ atom in the trap, $g_N^{(2)}(0) = \frac{N-1}{N} \geq 0.5$.

We extract the second order correlation function $g^{(2)}(\tau)$ from the fluorescence of the trapped atom exposed to the MOT beams with the help of detectors D1 and D2 that couple to the atom from opposite directions through the same Gaussian mode (Fig. 4.1). Figure 4.5 shows the histogram of the time delays between photodetection events at detectors D1 and D2. It reveals a Rabi oscillation with ≈ 63 MHz and a damping time compatible with the spontaneous decay lifetime of the 5P state in ^{87}Rb (27 ns). An almost vanishing $g^{(2)}(\tau = 0)$ that is clearly smaller than 0.5 provides further evidence that we only have a single atom in the trap [86, 129, 150].

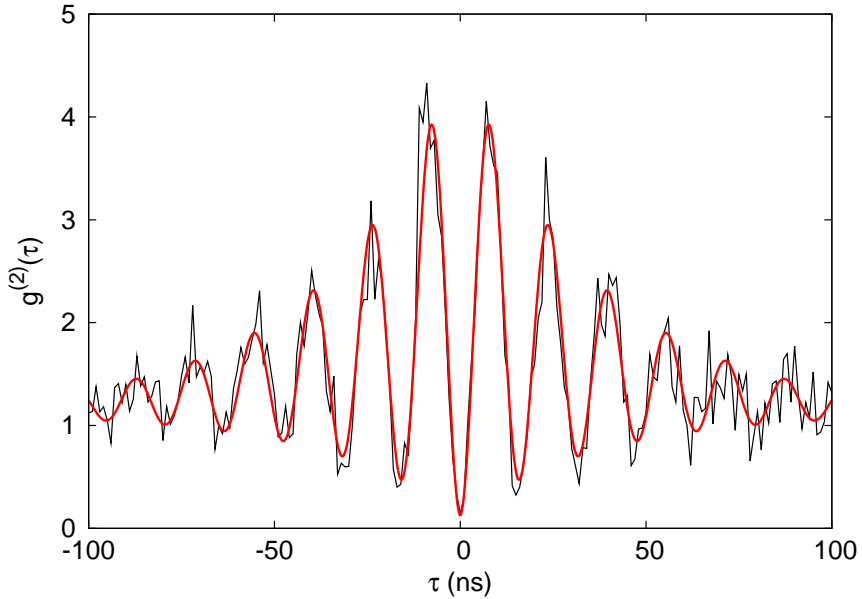


Figure 4.5: Normalized second-order correlation function versus time delay τ between two photodetection events at detectors D1 and D2 (not corrected for background counts) with clear anti-bunching at $\tau = 0$. The smooth red line is a fit to the data points using a sinusoidal term with a delay-dependent envelope.

4.4 Influence of external fields on the trapped atom

Two major sources of external fields experienced by the trapped ^{87}Rb atom are the magnetic field and the FORT light. The magnetic field comes mostly from the earth's field and stray fields from the ion-getter pump. The magnetic field at the center of the MOT is zeroed with three pairs of Helmholtz coils to an uncertainty of ± 10 mGauss in all directions. The FORT light has a larger effect on the atom than the magnetic field. It causes AC Stark shifts to the energy levels of the ^{87}Rb atom, and breaks the degeneracy of the hyperfine states.

In order to achieve maximum scattering, it is necessary to keep the ^{87}Rb atom in a two-level ($|g_{\pm}\rangle$ and $|e_{\pm}\rangle$) cycling transition. However, uncompensated magnetic fields orthogonal to the quantization axis can cause the atom to undergo Larmor precession, leading to population transfer from the

$|g\pm\rangle$ and $|e\pm\rangle$ states to other $|m_F\rangle$, $|m_{F'}\rangle$ states. Similarly, if $|g\pm\rangle$ and $|e\pm\rangle$ (defined through optical pumping by the probe) are not quasi-energy eigenstates of the atom in the FORT, the population also leaks out of the two-level system. Such population leakage is detrimental especially when the optical pumping rate by the probe is low.

To minimize the depopulation effect caused by the external field, we carefully zero the magnetic field at the location of the trapped atom, and then apply a magnetic bias field along the quantization axis during the measurement. We also adopt a right-hand circularly polarized FORT beam along the quantization axis¹⁰. In this case, the Zeeman and AC Stark shifts (see Fig. 4.6) have the same sign on individual $(5S_{1/2}, F = 2)$ hyperfine substates, breaking the degeneracy of the $(5S_{1/2}, F = 2)$ hyperfine states. This in turn reduces the depopulation effect caused by any uncompensated external fields perpendicular to the quantization axis.

AC Stark shift

Figure 4.6 shows the calculated AC Stark shift of the $(5S_{1/2}, F = 2)$ and $(5P_{3/2}, F' = 3)$ hyperfine states of the ^{87}Rb atom under the influence of a circularly polarized FORT light of 980 nm wavelength with a trapping potential depth of $h \cdot 27$ MHz (see Appendix A.5 for the calculation of AC Stark shift). The quantization axis of our system is chosen parallel to the main propagation axes of the probe/FORT beams such that the polarization of the FORT field is right-hand circular. A σ^+ probe refers to a circular polarization that drives the atom from $|g+\rangle$ to $|e+\rangle$, and a σ^- probe to one driving a $|g-\rangle$ to $|e-\rangle$ transition. At the center of the FORT, the energies of $5S_{1/2}$ states are lowered by an average of $h \cdot 27$ MHz (defining the trapping potential) with a small sublevel energy splitting of ≈ 1 MHz. The $5P_{3/2}$ levels shift upwards and are strongly split, forming a repulsive potential. The resulting shifts of the resonance frequency for different transitions can be observed directly in

¹⁰We observed that the extinction of the probe drops by a factor of two when using a linearly polarized FORT field rather than a circularly polarized FORT field.

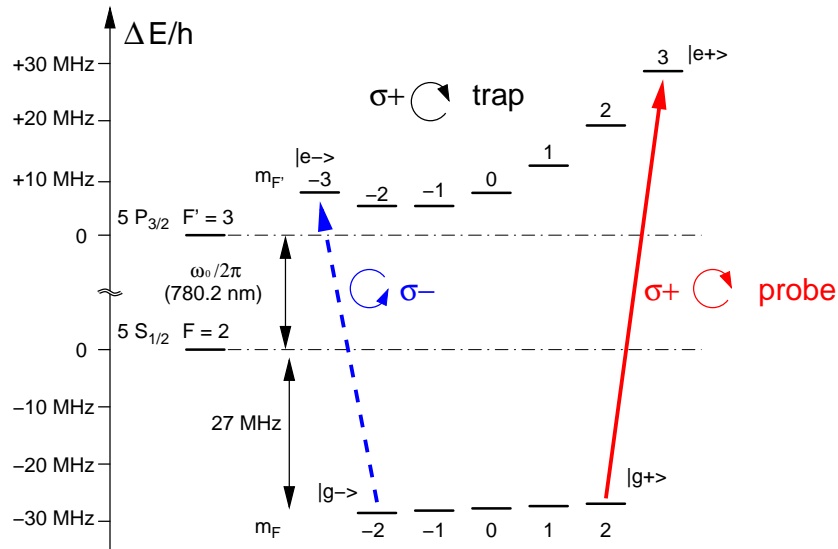


Figure 4.6: Predicted AC Stark shift of a ^{87}Rb atom in a circularly polarized FORT for the parameters mentioned in the text.

a transmission spectrum of a single ^{87}Rb atom in which the frequency of the probe is scanned over the resonance frequency of the trapped atom.

4.5 Measuring the transmission

Once an atom is loaded into the FORT, its fluorescence due to the MOT beams is detected by detector D2. This triggers the transmission measurement sequence, in which the main steps include:

1. Switching off the MOT beams and the MOT quadrupole coil current ¹¹.
2. Application of a magnetic bias field of $\approx 2\text{ G}$ along the quantization axis.
3. Waiting for 20 ms so that current in the coils stabilizes and optically pumping the atom into either $|g+\rangle$ or $|g-\rangle$ at the same time.

¹¹The quadrupole magnetic field is switched off to prevent the formation of an atom cloud in the MOT during the checking process in step 5, thereby avoiding the loading of a second atom that would result in an immediate loss of both atoms.

4. Recording the photo counts n_m of the transmitted probe beam for τ_m ranging from 130 to 140 ms with detector D1.
5. Switching on the MOT beams to check whether the atom is still in the FORT by monitoring fluorescence with detector D2. This process takes about 20 ms; if “yes”, turn off the MOT beams and repeat step 3 and 4.
6. Otherwise, recording the photo counts, n_r , of the transmitted probe beam with detector D1 for $\tau_r = 2$ s without an atom in the trap for reference.
7. Turning on the MOT beams and quadrupole coil current, and wait for another atom to be trapped by the FORT.

To avoid the atom being heated up and even kicked out of the FORT by the probe during the extinction measurement, the intensity of the probe is reduced to a level where the actual photon scattering rate was estimated to be around 2500 s^{-1} .

Figure 4.7 shows an excerpt of typical photocounts of detector D2 (green dashed line) and the gated photocounts of detector D1 (red solid line) for an atom trapping event during the transmission measurement. The probe is never switched off to avoid thermal artefacts in the measurement¹². Instead, electronic pulses from detector D1 are gated to only transmit the photo-detection events during step 4 and step 6 in the transmission measurement sequence. The gated photocounts of D1 and photocounts of D2 peak alternately because D1 is gated off when the MOT beams are turned on to check the presence of the trapped atom, and vice versa. When the atom is exposed to the MOT beams, detector D2 fires at a rate of 2000-3000 counts s^{-1} with a background contribution of 200-400 counts s^{-1} ¹³. With such signal

¹²The power of the probe fluctuates greatly (up to a few ten percent) within the first few seconds after it is switched on using an acousto-optic modulator.

¹³A small part of the probe beam is reflected by the fiber before detector D1 into detector D2. Detector D2 has a dark count of about 100 s^{-1} .

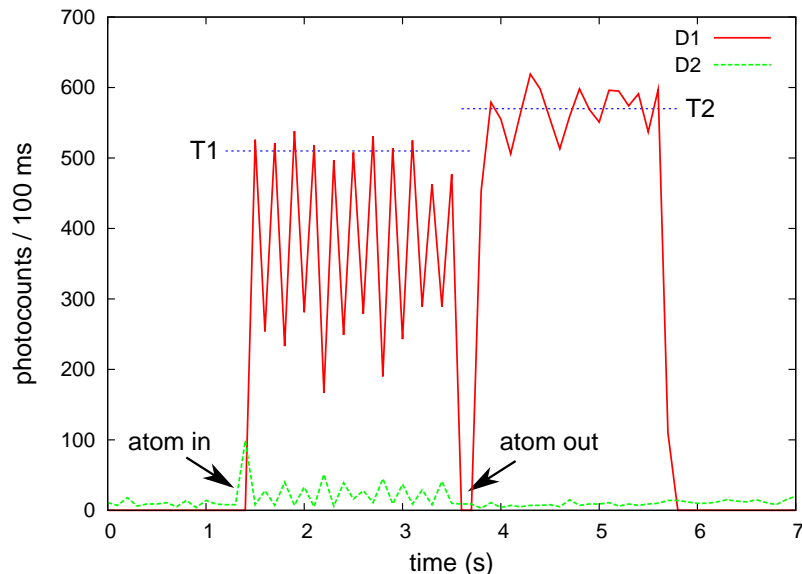


Figure 4.7: An excerpt of real time photocounts of detector D2 (dashed green line) and gated photocounts of detector D1 (solid red line) for an atom trapping event. Difference in the probe photocounts with (T1) and without (T2) a ^{87}Rb atom in the FORT is clearly observed.

and noise levels, it takes about 10 to 30 ms to reliably determine the presence of a trapped atom. The count rates of D2 thus appear to be smaller in Fig. 4.7 than $2000\text{--}3000\text{ counts s}^{-1}$ because the time bin in the figure is 100 ms whereas the atom checking time is only about 20 ms. The average probe transmission $T1$ when the atom is in the FORT is clearly lower than the transmission $T2$ when the atom is not in the FORT.

For every atom trapping event, we obtain a transmission value T by

$$T = \frac{\sum n_m \tau_r}{\sum \tau_m n_r}, \quad (4.7)$$

where the summation is carried over all contiguous measurement intervals m for which an atom was found in the trap. The accuracy of each transmission value T is shot noise limited. We typically obtain an mean transmission value \bar{T} by averaging over about 100 of such transmission values, each weighted

by ¹⁴

$$w = \frac{\tau_r \sum \tau_m}{\tau_r + \sum \tau_m}. \quad (4.8)$$

4.6 Results

We obtain the transmission spectrum of a trapped ^{87}Rb atom by scanning the frequency of the probe over its resonant frequency. Figure 4.8 shows the transmission \bar{T} of the probe as a function of detuning from the natural resonant frequency $\omega_0/2\pi$ of the $|g\rangle$ to $|e\rangle$ transition. The two spectra of a single ^{87}Rb atom were obtained for the σ^+ and σ^- probes, while keeping the handedness of the FORT beam fixed. In this experiment, we use a probe with incident waist w_L of 1.3 mm and a FORT focal waist of $\simeq 1.4\ \mu\text{m}$. As expected, the atomic resonance frequency is different for the two probe polarizations. The shifted frequencies agree quite well with the predictions shown in Fig. 4.6. The Lorentzian fit to the transmission spectrum for the σ^- probe shows a maximum extinction of $9.8 \pm 0.2\%$ with a full-width-half-maximum (FWHM) of $7.5 \pm 0.2\ \text{MHz}$. The σ^+ probe gives a maximum extinction of $7.4 \pm 0.1\%$ with a FWHM of $9.1 \pm 0.3\ \text{MHz}$. From the fact that the D2 transition of ^{87}Rb has a natural linewidth of 6.0 MHz and that the linewidth of the probe laser is about 1 MHz, we conclude that an atom exposed to the σ^- probe has been successfully kept in a two-level cycling transition, and it experiences very small spectral broadening caused by position dependent AC Stark shift in the FORT. However, the same conclusion cannot be made for an atom exposed to a σ^+ probe. A possible explanation is that optical pumping by the σ^+ probe is less effective because the probe frequency resonant to the $|g+\rangle$ to $|e+\rangle$ transition is further detuned from the resonant frequencies of other $|F = 2, m_F\rangle$ to $|F' = 3, m_{F'}\rangle$ transitions, whereas the resonance frequency of $|g-\rangle$ to $|e-\rangle$ is less detuned from other transitions (Fig. 4.6). Furthermore, a FORT wavelength of 980 nm forms a repulsive potential for the $5\text{P}_{3/2}$ levels of the ^{87}Rb atom. As the energy of $|e+\rangle$ is higher than that

¹⁴The amount of time an atom stays in the FORT varies. Thus the transmission value T obtained for every trapping event has a different uncertainty. We choose a weighting factor that minimizes the error of \bar{T} for a fixed number of trapping events.

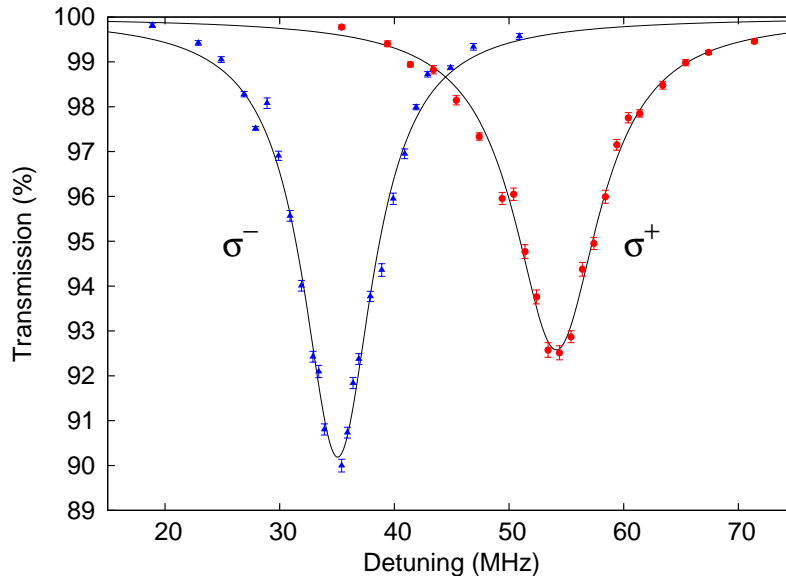


Figure 4.8: Transmission of the probe beam versus detuning from the natural resonant frequency $\omega_0/2\pi$ of the $|g\rangle$ to $|e\rangle$ transition. The absolute photon scattering rate is kept at $\approx 2500\text{s}^{-1}$ for every point by adjusting the probe intensity according to the measured extinction. The solid lines are Lorentzian fits.

of the $|e-\rangle$, an atom in $|e+\rangle$ experiences a stronger repulsive force from the FORT on average. As a result, a trapped ^{87}Rb atom might be more susceptible to increase of kinetic energy under the σ^+ probe, and thus oscillates more strongly around the focus.

Table 4.1 summarizes the main properties of the measured transmission spectra for different probe incident waists w_L . Our experiment started initially with a FORT focal waist w_D of $\simeq 2\mu\text{m}$. When we focused the probe tighter, we also reduced the FORT focal waist to $\simeq 1.4\mu\text{m}$ to confine the atom more tightly. At the same time, the power of the FORT light was reduced accordingly to keep the depth of the FORT constant. For the same w_L , the maximum extinction ϵ of the σ^- probe is always larger than that of the σ^+ probe. Concurrently, the spectral width measured with of the σ^- probe is always smaller than that measured with the σ^+ probe. When we focus the probe more strongly, the maximum extinction of the probe increases. However, the FWHM of the transmission spectrum also becomes larger for

some unknown reasons. We observe a maximum extinction of 10.4% for a probe incident waist w_L of 1.4 mm. Although a higher extinction is to be expected for a larger w_L , we did not attempt such a measurement for reasons that would be stated in the next section.

Table 4.1: Summary of transmission spectra of the probe for different focusing strengths. w_L : incident waist of the probe; w_F and w_D : estimated focal waists of the probe and of the FORT respectively using the paraxial approximation (Section 3.3.4.); ϵ and W : maximum extinction value and FWHM of the transmission spectrum respectively.

			σ^- probe		σ^+ probe	
w_L (mm)	w_F (μm)	w_D (μm)	ϵ (%)	W (MHz)	ϵ (%)	W (MHz)
0.5	2.23	2.0	2.38 ± 0.03	7.1 ± 0.2	N.A.	N.A.
1.1	1.01	2.0	7.2 ± 0.1	7.4 ± 0.2	5.8 ± 0.1	8.8 ± 0.2
1.3	0.86	1.4	9.8 ± 0.2	7.5 ± 0.2	7.4 ± 0.1	9.1 ± 0.3
1.4	0.80	1.4	10.4 ± 0.1	7.7 ± 0.2	7.6 ± 0.1	9.8 ± 0.3

4.7 Losses and interference artefacts

In this section, we discuss the reliability and the limitation of the results we have obtained. We have previously emphasized the importance of collecting all of the probe in an extinction experiment performed on a single quantum system because this allows us to directly quantify the scattering probability with the measured extinction value. However, collecting all of the probe does not necessarily imply that there is no loss in the transmission path. For example, introducing a grey filter in front of the power detector does not change the measured extinction. However, placing a pin hole or a polarizer before the power detector to select a certain component of the probe can change the outcome of the measurement completely. For example, if an atom scatters 1/1000 of a vertically polarized probe, a correctly performed transmission measurement would reveal a drop of 0.1% in the transmitted power when there is an atom in the path of the probe (with or without a grey

filter in front of the power detector). However, if a polarizer is placed before the power detector such that only a very small portion of the probe is transmitted, then what the power detector measures is the result of interference between the filtered scattered light and the filtered probe. Furthermore, if the field strengths of the filtered scattered light and probe are comparable, one would expect to observe a large ‘extinction’ (not 0.1% as it should be) when the two fields interfere destructively, and observe a ‘transmission’ more than 100% when the fields interfere constructively¹⁵. Consequently, it is important to ensure that the design of the transmission measurement setup does not preferentially filter more probe than scattered light if one wants to measure the extinction of a single quantum system without such interference effects.

We carefully quantified the losses of the probe in its optical path to ensure that our results are free from such interference artefacts. Table 4.2 shows the losses of the probe in the transmission channel for different incident waists w_L we used in the experiment. T_{AB} is the total transmission from point A (before the vacuum chamber) to point B (after the single-mode fiber and just before the detector D1) in Fig. 4.1. It ranges from 53% to 62%. For more detailed characterization, we group the transmission losses into three parts:

1. the loss across the vacuum chamber which includes four uncoated cuvette surfaces and the two AR-coated aspheric lenses, L_{vac} ;
2. the loss from after the vacuum chamber to before the receiving optical fiber which contains two dichroic mirrors, an interference filter (peak transmission $T=96\%$ at 780 nm) and a mirror, L_{optics} ;
3. the coupling loss into the uncoated single mode fiber before detector D1, L_{fiber} ¹⁶.

The losses L_{vac} and L_{optics} are due to reflection except the extra 0.5% loss of L_{vac} for larger incident waists, which is due to cutting of the larger

¹⁵Such phenomena have been observed in a number of absorption spectroscopy experiments performed on single molecules and quantum dots [121, 123, 125, 126].

¹⁶Note: $T_{AB} = (1 - L_{vac}) \times (1 - L_{optics}) \times (1 - L_{fiber})$. All reported losses have a uncertainty of $\pm 0.1\%$.

probe beam by the aspheric lenses. For the fiber coupling loss, about 8% is caused by reflection, and the remaining 10-20% loss is due to imperfect mode matching. Therefore, a major part of the transmission losses in our system are due to reflection. Since the scattered field and the probe field should experience the same reflection loss at each surface, we are reasonably confident that our results are free from interference artefacts.

Table 4.2: Transmission losses of the probes of different incident waists.

w_L (mm)	L_{vac} (%)	L_{optics} (%)	L_{fiber} (%)	T_{AB} (%)
0.5	21.0	5.4	17.3	62
1.1	21.0	5.3	18.2	61
1.3	21.5	5.4	27.0	54
1.4	21.6	5.3	28.4	53

On the other hand, since we collimate the incident probe with an aspheric lens after the output fiber, the diameter of the probe is limited by the clear aperture size of the lens (4.95 mm). The incident probe thus resembles a Gaussian beam whose outer portion has been cut off. As our theoretical model assumes a Gaussian probe, one would expect a certain degree of discrepancy between experimental results and theoretical predictions. Furthermore, when the coupling loss into the fiber becomes larger due to such mode mismatch, our results would become more susceptible to interference artefacts.

4.8 Comparison with theoretical models

We emphasize that the highest extinction of 10.4% observed for a probe with an ≈ 800 nm waist at the focus is large when compared to results reported from experiments performed on single molecules and quantum dots [124, 125, 126, 127]. There, the excitation light field was either confined by a small aperture of ≈ 100 nm [124, 125], or focused using solid immersion lenses [126, 127] that provide much tighter focusing than our case. In all

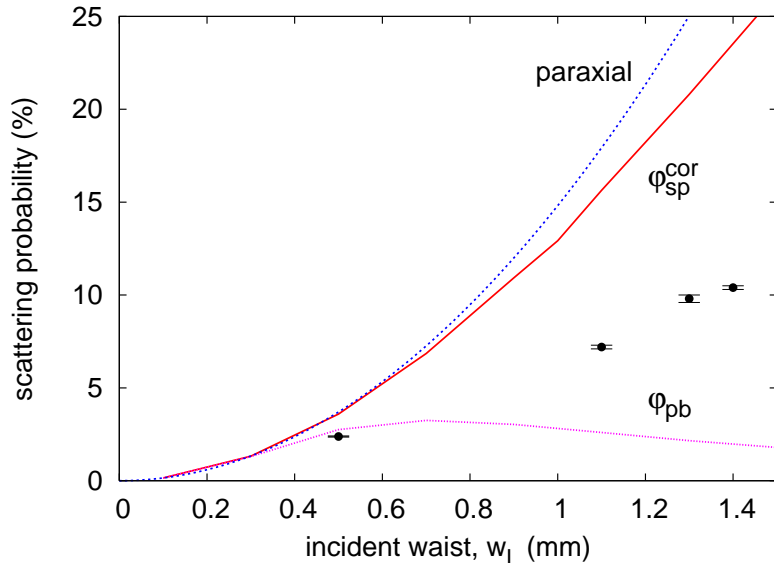


Figure 4.9: Comparison of measured extinctions to scattering probabilities predicted by paraxial approximation (Eqn. 3.39), spherical wave front with polarization correction (Eqn. 3.34), and parabolic wave front (Eqn. 3.24).

these experiments the quantum systems were embedded into complex solid state host environments which complicates the theoretical treatment of light scattering. In contrast, the conceptual simplicity of our system and the fact that we directly measure the extinction of the probe beam allows a clean comparison with existing photon-atom coupling models [1, 85, 112].

One of the models that closely describes our experiment was presented by van Enk and Kimble [1]. It considers a monochromatic and circularly polarized Gaussian beam focused by a thin ideal lens onto a two-level atomic system. Estimations based on that model gave a very dim outlook on the effectiveness of coupling light to an atom using a lens. Our experimental results clearly falsify their predictions. As it turns out, two approximations used in their model (parabolic wave front after the lens, and no change to the polarization of a light beam passing through the lens) has greatly underestimated scattering probability for stronger focusing. Dropping these approximations, we find (with otherwise the same methods) that a much higher scattering probability can be achieved using this coupling scheme.

Figure 4.9 shows the maximum extinctions of the σ^- probe for various incident waists together with the scattering probabilities predicted by various models discussed in Chapter 3. Note that the measured extinction is not identical to the scattering probability. For our experimental parameters, the extinction is typically a few percent smaller than the actual scattering probability (See Section 3.1). Except for the data point at $w_L = 0.5$ mm which can be well explained by both models, the other data points lie well above the prediction using van Enk’s model, but below the prediction of our extended model (Section 3.3.3). It is reasonable that the measured extinction is lower than the predicted values using our extended model ($\varphi_{\text{sp}}^{\text{cor}}$) since the aspheric lens is not ideal, and the atom is not completely stationary at the focus. The deviation of the experimental results from theoretical predictions gets larger as the incident waist increases. We conjecture a few possible explanations for this phenomenon:

1. Our model assumes a Gaussian probe that is focused by an ideal lens such that the field after the lens has a spherical wave front. However, as the incident waist of the probe increases, two deviations from our theoretical model occur: (i) A larger portion of the probe is cut by the aperture of the collimating lens (Section 4.7), causing the probe to further deviate from the Gaussian; (ii) A real lens typically introduces a larger aberration to a focusing field at positions further away from the lens axis. This effect translates into a larger deviation from a spherical wave front for a larger incident waist, and therefore a smaller field amplitude at the focus compared to that when using an ideal lens.
2. Increasing the incident waist makes the probe focus tighter, thereby stronger confinement of the atom is required. Inadequate confinement of the atom is one reason why extinction values smaller than predicted are obtained. However, the motion of the atom alone cannot explain the 50% reduction in the observed scattering probability. For the tightest probe focusing we used ($w_L = 1.4$ mm), we estimated that the motion of the atom reduces the scattering probability by less than 20% (Appendix A.7).

3. Another possible reason is that the model we used is incomplete. One assumption in our model is that the presence of the atom does not alter the properties of the field at the focus ¹⁷. This assumption should work well when the photon flux of the incident probe is large [101]. However, when the photon flux (or field intensity ¹⁸) of the probe is very low ¹⁹ and when the focal waist is small, the presence of the atom might have a significant influence on the focal field. To make the points clearer, let us consider a small spherical glass bead with a refractive index n , and a diameter of $1\ \mu\text{m}$. If we place the glass bead in a $780\ \text{nm}$ light beam with a focal waist of $100\ \mu\text{m}$, the propagation of the light beam can be described well without considering the effects of the glass bead. Now, if the light beam is focused down to a focal waist of $1\ \mu\text{m}$, and the glass bead is placed at the focus of the light, the propagation of the light beam through the focus can no longer be described using source-free Maxwell equations. Under this situation, the glass bead would act as a lens, and it would reflect or scatter part of the incident beam. The overall effect is that the field seen by the glass bead must be different from that at the focus when there is no glass bead. Coming back to the atom, it is true that a single atom does not have a refractive index and its size is much smaller than $1\ \mu\text{m}$. Nevertheless, when the atom is exposed to a resonance light field that is weak compared to its transition saturation intensity, it has a scattering cross section on the order λ^2 . The fact that a single atom can scatter 10% of the incident light suggests that a single atom acts like a $1\ \mu\text{m}$ glass bead when the field frequency is close to the resonance. As such, there is a strong reason to believe that the field experienced by the atom under a

¹⁷We calculate the field at the location of the focus using a set of field modes that satisfies the *source-free* Maxwell equations.

¹⁸We do not know for sure which quantity matters most for the following problem.

¹⁹In our experiments, the photon flux of the probe ranges from 20k to 80k photons s^{-1} , much smaller than the spontaneous decay rate Γ of the Rb atom. The intensity of the probe at the FORT is on the order of 0.1% of the saturation intensity.

strongly focused but weak field ²⁰ cannot be described using source-free Maxwell equations. Instead, mutual influence between the field and the atom must be considered to correctly quantify the scattering of the light field by the atom. Having said that, we note in passing that solving the field and atomic evolution without neglecting the mutual effects on both the atom and the field is a mathematically intractable problem for an atom in free space [101]. In any case, it would be interesting to see how our predictions is changed by considering the mutual influence between the atom and the field.

4.9 Conclusion

In conclusion, we experimentally observed a substantial extinction (up to 10.4%) of a weak coherent light field by a single ⁸⁷Rb atom through focusing the light beam using a lens. As our measurements is free from interference artefacts, the measured extinction values set a lower bound to the scattering probability of the probe by an atom in free space. We therefore conclusively show that substantial interaction between a light beam and a single atom is possible without a cavity. The strong interaction of the atom with a ‘flying’ qubit suggests using the atom as a mediator for photon-photon interactions, thus pointing in a new direction for implementing photonic quantum gates.

²⁰‘Strongly focused’ and ‘weak’ are not contradicting each other. ‘Strongly focused’ refers to a tight focal spot. A strongly focused weak field can be created by reducing the incident power of the probe.

Chapter 5

Outlook and open questions

We have shown experimentally and theoretically that strong interaction between light and a single quantum system can be achieved by focusing light with a lens. In particular, we have observed a 10.4% extinction of light by a single ^{87}Rb atom by focusing the light beam using an aspheric lens of 0.55 NA. We believe that a much higher extinction/scattering probability will be observed by focusing the probe more tightly using a lens with a larger NA.

We now consider the implications of our results for quantum information transfer. Is the 10.4% scattering probability we measured equivalent to 10.4% of the photons transferring quantum information to the atom in our experiment?

Unfortunately, the answer is no. First, to complete meaningful information transfer, the information receiver should be able to store the quantum information for a period of time, whilst allowing during this time for the information to be measured or retrieved. Since we are pumping the ^{87}Rb atom using continuous-wave coherent light, there is no way to know when the atom is in the excited state due to the randomness introduced by spontaneous emission. In this case, one cannot know when the information is accessible even if quantum information in a photon is transferred to the atom before every scattering event. Second, meaningful information should consist at least of two different results. Information that has only one outcome has

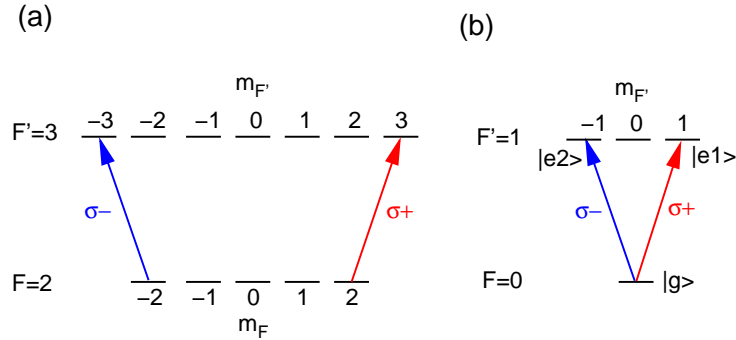


Figure 5.1: (a) Energy structure of the ^{87}Rb atom used in our light extinction experiment, not suitable for encoding the polarization state of the probe photons. (b) Ideal level scheme for encoding polarization state of photons.

no information value. In our experiment, the polarization of the probe is either right-hand or left-hand circular, and not an arbitrary superposition of both handedness. As a result, the ^{87}Rb atom is always excited to the same state in any set of the experiment. As such, no meaningful information has been transferred to the atom in the experiment.

To make our system more applicable to quantum information transfer, we can choose a quantum system that has a more suitable energy structure for quantum information transfer. For example, if we want to encode the polarization state of a photon, we require a quantum system with a level scheme shown in Fig. 5.1(b). In this level scheme, the ground state $|g\rangle$ is non-degenerate, and there are no other relaxation channels for the excited states ($|e1\rangle$ and $|e2\rangle$) except dipole transitions to $|g\rangle$. In this case, the atom can be excited to a superposition of $|e1\rangle$ and $|e2\rangle$ states depending on the polarization of the incoming photon. This quantum system can thus be used to store quantum information from a photon.

Another obvious improvement is to replace the weak coherent probe with real single photon pulses, ideally single photons that can be created on-demand [91, 92, 93]. By adopting such light sources, one can measure deterministically the atomic state after the pulse excitation. Ideally, one should create a single photon pulse whose spatial and temporal profiles match the respective atomic dipole emission in order to achieve a high absorption proba-

bility. This idea is motivated by considering photon absorption as the reverse process of spontaneous emission [85] (Section 3.2.1).

However, there is no consensus on whether spontaneous emission is a reversible process. Sondermann et al. [85] argued that the reversibility of the spontaneous emission process can be inferred from the fact that the Schrödinger equation is invariant under time reversal for a closed system with a Hamiltonian without any explicit time dependence. However, it is not clear if the ‘closed system’ can include the infinitely many vacuum modes which causes spontaneous emission of an atom in free space. Recently, Robert Alicki [155] claimed that by using an exactly solvable model of the Wigner-Weisskopf atom, an unstable quantum state cannot be completely recovered by the creation of the time reversed decay product state.

Let us consider a Gedanken experiment in which one creates a time reversed replica of a spontaneously emitted photon, and focuses this single photon wave packet onto an atom in the ground state. If spontaneous emission is reversible, the atom is in its excited state with absolute certainty after the wave packet fully ‘passes’ the atom. In this sense, the wave packet is a single photon π -pulse. As a rule, if a π -pulse transfers an atom from the ground state to an excited state with a spontaneous decay lifetime of τ , it should have a pulse length much shorter than τ . This requirement is to avoid spontaneous emissions during the application of the pulse on the atom since spontaneous decay events reduce the fidelity of the π -pulse. On the other hand, the spontaneously emitted photon wave packet has a pulse length on the order of τ [98]. Therefore, **if** spontaneous emission is reversible, one has a π -pulse with a pulse length of τ and a fidelity of unity. Is this possible? What prevents spontaneous emission from occurring during the application of the single photon π -pulse?

Is spontaneous emission really reversible? If it is not, what is the maximum absorption probability of a single photon pulse by a single atom in free space? By achieving stronger atom-light interaction using a lens with a larger NA, we may be able to quantitatively disprove certain atom-light interaction models with our current setup.

Appendix A

A.1 A two-level system in monochromatic radiation

A two level system under the influence of monochromatic radiation has been discussed in great detail in many textbooks [95, 99, 100]. Here, we consider circularly polarized radiation which corresponds to our experimental setup.

We start with a single-electron spherically symmetric two-level atom with an unperturbed Hamiltonian H_0 and energy eigenstates $|\phi_1\rangle$ and $|\phi_2\rangle$ that satisfy

$$H_0|\phi_i\rangle = \hbar\omega_i|\phi_i\rangle. \quad (\text{A.1})$$

Neglecting spontaneous decay, the interaction between the atom and incident monochromatic radiation can be modeled by an interaction Hamiltonian (under the dipole approximation)

$$H_I = e\vec{r} \cdot \vec{E}(t), \quad (\text{A.2})$$

where \vec{r} is the position operator, $\vec{E}(t)$ is the time-dependent electric field strength at the location of the atom, and $e = 1.6 \times 10^{-19}$ C. In particular, if the external radiation is of the form

$$\vec{E}(t) = \frac{E_0}{\sqrt{2}} [\cos(\omega t)\hat{x} + \sin(\omega t)\hat{y}], \quad (\text{A.3})$$

the interaction Hamiltonian becomes

$$H_I = \frac{eE_0}{2}r_-e^{+i\omega t} - \frac{eE_0}{2}r_+e^{-i\omega t} \quad (\text{A.4})$$

where $r_{\pm} = \mp(x \pm iy)/\sqrt{2}$. Note that by writing the interaction Hamiltonian as a product of the dipole operator and the external field, we implicitly neglect any modification of the incident radiation due to its interaction with the atom [95].

The atomic state $|\Psi\rangle$ satisfies the Schrödinger equation:

$$i\hbar\frac{\partial|\Psi\rangle}{\partial t} = (H_0 + H_I)|\Psi\rangle. \quad (\text{A.5})$$

Expanding the atomic state as

$$|\Psi\rangle = c_1(t)|\phi_1\rangle e^{-i\omega_1 t} + c_2(t)|\phi_2\rangle e^{-i\omega_2 t}, \quad (\text{A.6})$$

we obtain ¹

$$i\dot{c}_1 = \frac{c_2}{\hbar} \left\{ e^{i(\omega-\omega_0)t} \frac{\langle 1|eE_0r_-|2\rangle}{2} + e^{-i(\omega+\omega_0)t} \frac{\langle 1|-eE_0r_+|2\rangle}{2} \right\}, \quad (\text{A.7})$$

$$i\dot{c}_2 = \frac{c_1}{\hbar} \left\{ e^{i(\omega+\omega_0)t} \frac{\langle 2|eE_0r_-|1\rangle}{2} + e^{-i(\omega-\omega_0)t} \frac{\langle 2|-eE_0r_+|1\rangle}{2} \right\}, \quad (\text{A.8})$$

where $\omega_0 = \omega_2 - \omega_1$, and $|\phi_j\rangle$ is written as $|j\rangle$ for simplicity. In the case where the radiation has frequency close to the resonance at ω_0 such that $|\omega_0 - \omega| \ll \omega_0$, the terms with $(\omega + \omega_0)t$ oscillate very fast compared to the terms $(\omega - \omega_0)t$ and therefore average to zero over any reasonable interaction time (rotating wave approximation), leading to

$$\begin{aligned} i\dot{c}_1 &= c_2 e^{i(\omega-\omega_0)t} \frac{\Omega}{2}, \\ i\dot{c}_2 &= c_1 e^{-i(\omega-\omega_0)t} \frac{\Omega^*}{2}, \end{aligned} \quad (\text{A.9})$$

¹ $\langle \phi_j|r_{\pm}|\phi_j\rangle = 0$ because of symmetry.

where the Rabi frequency Ω is defined by

$$\Omega = \frac{E_0 \langle 1|er_-|2\rangle}{\hbar}. \quad (\text{A.10})$$

The solution of Eqn. A.9 basically shows that the atomic state oscillates between the ground state and the excited state with the effective Rabi frequency $\Omega' = \sqrt{\Omega^2 + (\omega - \omega_0)^2}$.

By incorporating spontaneous decay into the system [95, 99, 100], it can be shown that the upper state has a steady-state population (the probability that the atom is in the excited state)

$$\rho_{22} = \frac{|\Omega|^2/4}{\delta^2 + |\Omega|^2/2 + \Gamma^2/4}, \quad (\text{A.11})$$

where $\delta = \omega - \omega_0$ is the detuning of the radiation from the resonance. Γ is the spontaneous decay rate of the upper state such that $\dot{\rho}_{22} = -\Gamma\rho_{22}$ in the absence of external radiation. The rate of spontaneous decay from the excited state $|2\rangle$ to the ground state $|1\rangle$ is determined by the electronic wavefunctions of the two relevant states by ²

$$\Gamma = \frac{\omega^3 |\langle 1|er_-|2\rangle|^2}{3\pi\epsilon_0\hbar c^3}, \quad (\text{A.12})$$

where ϵ_0 is the permittivity of vacuum. The average optical power scattered by the atom is given by

$$P_{sc} = \rho_{22}\Gamma\hbar\omega. \quad (\text{A.13})$$

If the frequency of the external radiation is resonant with the transition frequency, and is weak compared to the saturation intensity (i.e. $\Omega \ll \Gamma$), the power scattered by the atom becomes (using Eqns. A.13, A.10, A.11 and A.12)

$$P_{sc} = \frac{3\epsilon_0 c \lambda^2 E_0^2}{4\pi}. \quad (\text{A.14})$$

²Eqn. A.12 can predict the decay rates of the hydrogen atom's transitions accurately.

Scattering Cross Section

The scattering cross section, σ of a two-level system exposed to a monochromatic plane wave is defined by [100]

$$\sigma = \frac{P_{sc}}{I}, \quad (\text{A.15})$$

where I is the intensity of the plane wave. For a circularly polarized plane wave described by Eqn. A.3,

$$I = \frac{1}{2}\epsilon_0 c E_0^2. \quad (\text{A.16})$$

As the maximum scattering cross-section is achieved when $\delta \ll \Gamma$ and $|\Omega| \ll \Gamma$, we can use Eqns. A.14, A.15, and A.16 to obtain

$$\sigma_{max} = \frac{3\lambda^2}{2\pi}. \quad (\text{A.17})$$

Although we adopt the semi-classical approach here, Eqns. A.14 and A.17 are identical to that obtained with the quantized-field version [95]. This is because one needs to ignore the influence of the atom on the light field in order to arrive at an analytical description of the atom in free space [95]. This assumption is identical to that adopted intrinsically in the semi-classical approach.

A.2 Numerical Integration of κ_μ

To obtain the expansion coefficient κ_μ in Eqn. 3.35, we need to perform the following integrations numerically:

$$\begin{aligned} I_0 &= \int_0^\infty d\rho \frac{\rho}{\sqrt{\cos\theta}} \left(\frac{1 + \cos\theta}{2} \right) J_0(k_t\rho) \exp \left[-ik(\sqrt{\rho^2 + f^2} - f) - \frac{\rho^2}{w_L^2} \right], \\ I_1 &= \int_0^\infty d\rho \frac{\rho}{\sqrt{\cos\theta}} \left(\frac{\sin\theta}{\sqrt{2}} \right) J_1(k_t\rho) \exp \left[-ik(\sqrt{\rho^2 + f^2} - f) - \frac{\rho^2}{w_L^2} \right], \\ I_2 &= \int_0^\infty d\rho \frac{\rho}{\sqrt{\cos\theta}} \left(\frac{\cos\theta - 1}{2} \right) J_2(k_t\rho) \exp \left[-ik(\sqrt{\rho^2 + f^2} - f) - \frac{\rho^2}{w_L^2} \right], \end{aligned}$$

where $\cos\theta = f/\sqrt{f^2 + \rho^2}$ and $\sin\theta = \rho/\sqrt{f^2 + \rho^2}$.

The integration consists of two oscillating parts: the Bessel term and the exponential term. Integrating such a fast oscillating function is non-trivial. For example, Mathematica 5 was not able to handle the above integration efficiently and reliably for our experimental parameters. We eventually adopted a fortran subroutine package ‘quadpack.f90’ (subroutine name: qage) [156] to perform such integrations.

Owing to the damping term $\exp(-\rho^2/w_L^2)$ in the integrand, we only integrate from $\rho = 0$ to $5w_L$ to achieve a small residual error. The results are required to have a relative error of less than 10^{-6} in the program.

Figures A.1, A.2 and A.3 show the real part of I_0 , I_1 , and I_2 respectively as a function of k_t/k . The values shown were computed with $f = 4.5$ mm, $w_L = 2$ mm, and $\lambda = 780$ nm. I_0 , I_1 , and I_2 exhibit oscillating behaviour (see insets). The oscillation frequencies become larger for larger k_t . One has to make sure that sufficient number of points are computed in each oscillation in order to interpolate κ_μ correctly. To do this, we typically performed 2×80 k numerical integrations for each I_n (real and imaginary parts computed separately). The computations were done in parallel on a computer farm with 32 CPUs (Intel(R) Xeon(TM) CPU 2.80 GHz). Each data point in Fig. 3.6 takes a few ten minutes to half a day to compute, with a longer

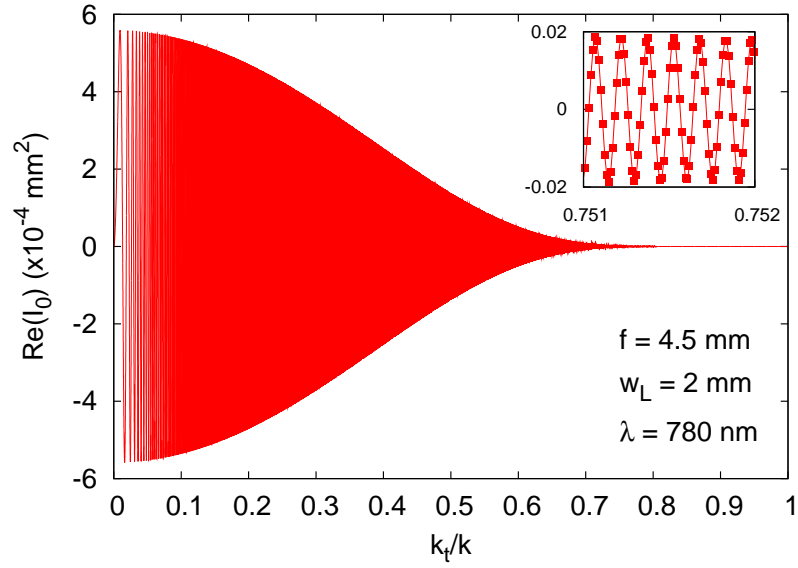


Figure A.1: The real part of I_0 as a function of k_t/k for the parameters stated. There are 80000 points in this graph. The inset is a zoom-in of the graph near $k_t/k = 0.75$, showing the fast oscillating nature of I_0 . The scales of the x- and y-axis of the inset are identical to those of the main graph.

computation time for larger w_L ³.

³The author gratefully acknowledges the assistance from Florian Huber for optimizing the integrating algorithm and writing the codes for multi-processor computing. Without his help, such beautiful results would not be possible.

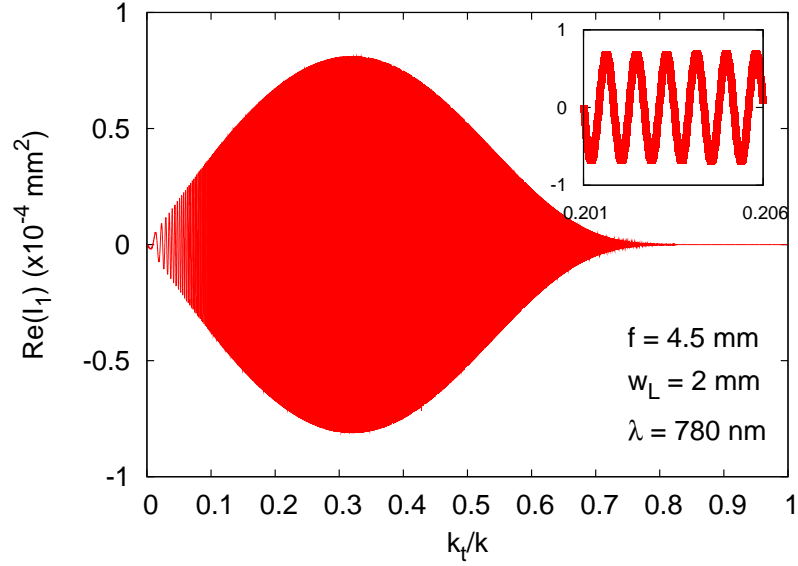


Figure A.2: The real part of I_1 as a function of k_t/k for the parameters stated. The inset is a zoom-in of the graph near $k_t/k = 0.2$. The scales of the x- and y-axis of the inset are identical to those of the main graph.

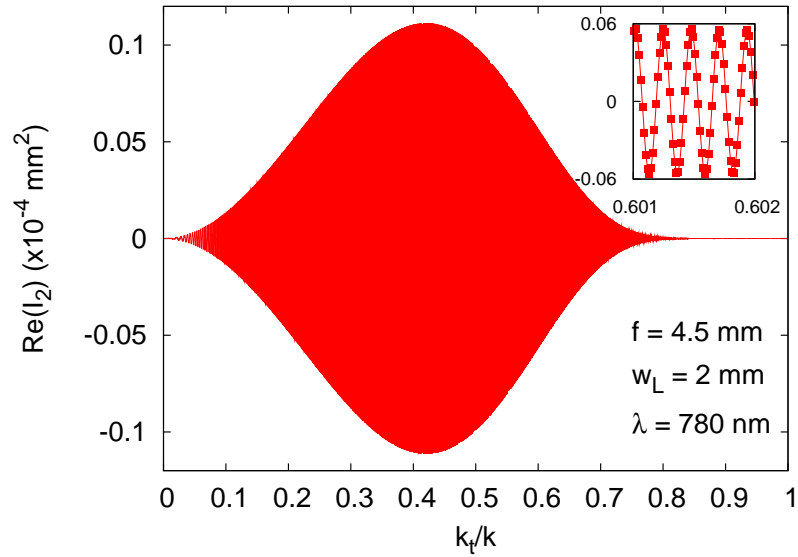


Figure A.3: The real part of I_2 as a function of k_t/k for the parameters stated. The inset is a zoom-in of the graph near $k_t/k = 0.6$. The scales of the x- and y-axis of the inset are identical to those of the main graph.

A.3 Energy levels of the ^{87}Rb atom

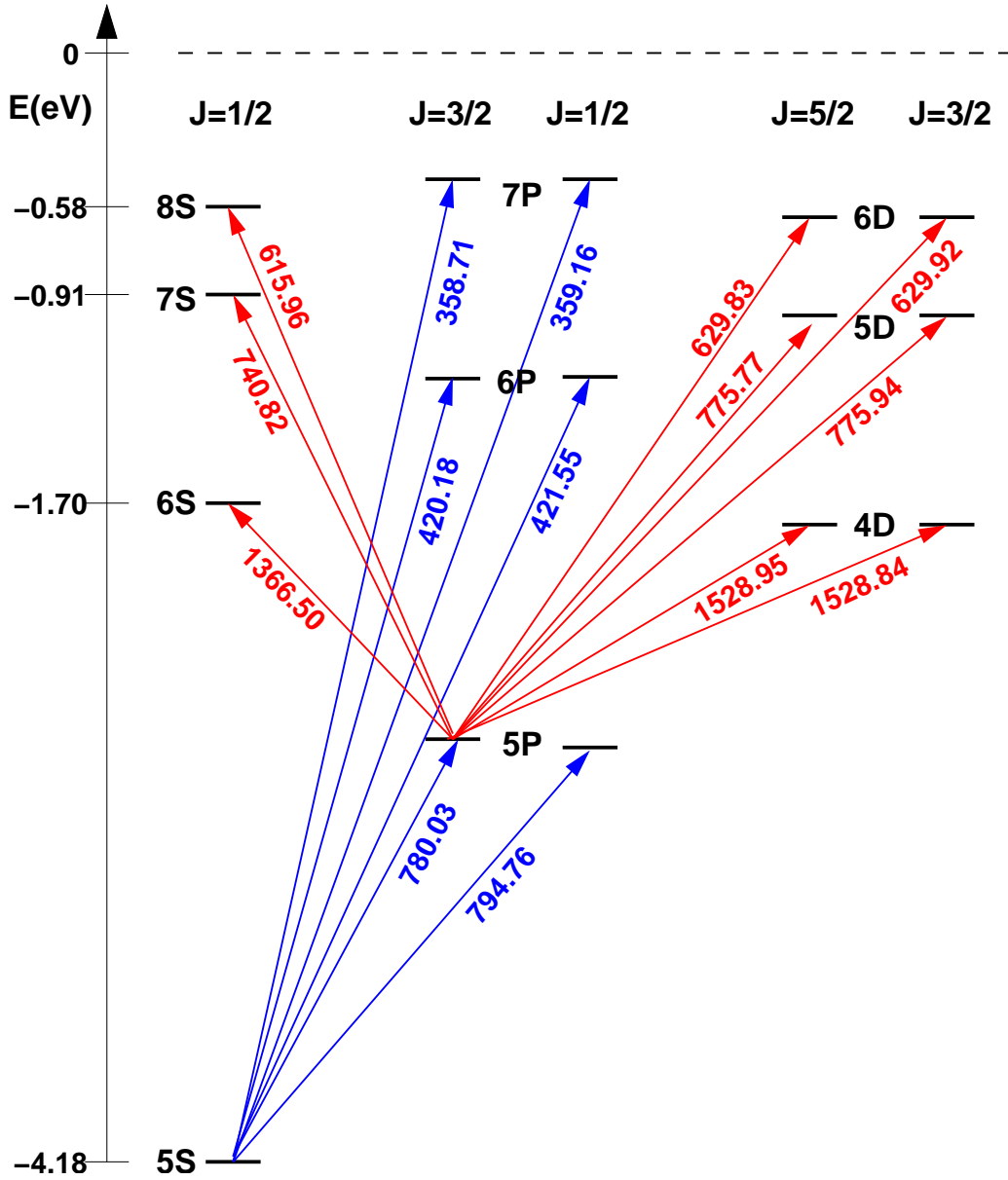


Figure A.4: Partial Grotrian diagram for Rb atom with dipole-allowed transitions to the $5S_{1/2}$ and $5P_{3/2}$ states. The wavelengths of the transitions are shown in nanometers.

A.4 The D1 and D2 transition hyperfine structure of the ^{87}Rb atom

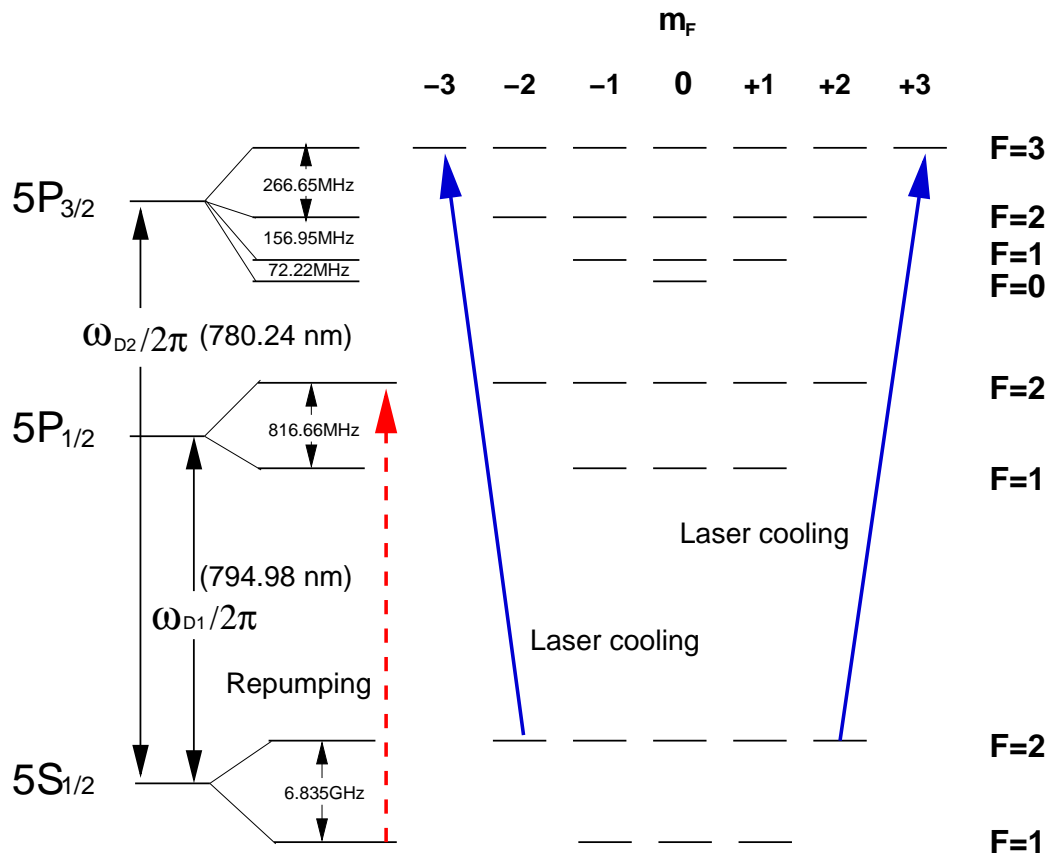


Figure A.5: Hyperfine structure of the D1 and D2 transition for the ^{87}Rb atom, with frequency splittings between the hyperfine levels. The transitions we used for the MOT are shown.

A.5 AC Stark shift

General discussion on time-dependent perturbation theory and AC Stark shift can be found in [157, 158]. Here we consolidate the formula and assumptions we used to predict the AC stark shift of a ^{87}Rb atom exposed a circularly polarized light. Starting from Eqn. A.2, the interaction Hamiltonian describing the interaction between a monochromatic light and an alkali atom can be written as

$$H_I(t) = V_+(\vec{r})e^{-i\omega t} + V_-(\vec{r})e^{i\omega t}, \quad (\text{A.18})$$

where the actual form of $V_{\pm}(\vec{r})$ depends on the polarization of the field. Using second-order time dependent perturbation theory, the AC-Stark shift of a hyperfine sublevel $|F, m_F\rangle$ is related to other hyperfine sublevels $|F', m_{F'}\rangle$ by

$$\Delta E(F, m_F) \approx \sum_{F', m_{F'}} \left\{ \frac{|\langle F, m_F | V_-(\vec{r}) | F', m_{F'} \rangle|^2}{\hbar(\omega_F - \omega_{F'} + \omega)} + \frac{|\langle F, m_F | V_+(\vec{r}) | F', m_{F'} \rangle|^2}{\hbar(\omega_F - \omega_{F'} - \omega)} \right\}, \quad (\text{A.19})$$

where $\hbar\omega_{F, F'}$ refer to the energies of the unperturbed states.

For a FORT that is circularly polarized along the quantization axis as adopted in our experiment (Chapter 4), we have

$$V_{\pm}(\vec{r}) = \mp \frac{eE_0}{2} r_{\pm 1}, \quad (\text{A.20})$$

according to Eqn. A.4, where $r_{\pm 1} = \mp(x \pm iy)/\sqrt{2}$ and $r_0 = z$. As the energies of various atomic states $\hbar\omega_{F'}$ are typically well-known, the task of calculating the AC-Stark shift reduces to determining the dipole matrix elements

$$\langle F, m_F | e r_q | F', m_{F'} \rangle. \quad (\text{A.21})$$

To calculate these matrix elements, it is useful to factor out the angular dependence and write the matrix element as a product of a Wigner-3j symbol,

a Wigner-6j symbol, and a reduced matrix element

$$\begin{aligned} \langle F, m_F | e r_q | F', m_{F'} \rangle &= \langle J || e \vec{r} || J' \rangle (-1)^{J+I+m_F} \sqrt{(2F+1)(2F'+1)} \\ &\times \begin{pmatrix} F' & 1 & F \\ m_{F'} & q & -m_F \end{pmatrix}_{3j} \begin{pmatrix} J & J' & 1 \\ F' & F & I \end{pmatrix}_{6j}, \end{aligned} \quad (\text{A.22})$$

where J, J' are the fine-structure total angular momentum (spin+orbital) quantum numbers for the $|F', m_{F'}\rangle, |F', m_{F'}\rangle$ states respectively, and I is the nuclear angular momentum quantum number [99, 158]. The reduced dipole matrix element between J and J' states can be obtained from the spontaneous radiative lifetime τ via the expression [99]

$$\frac{1}{\tau} = \frac{\omega_0^3}{3\pi\epsilon_0\hbar c^3} \frac{1}{2J'+1} |\langle J || e \vec{r} || J' \rangle|^2, \quad (\text{A.23})$$

with $\omega_0 = |\omega_{J'} - \omega_J|$. Note that, $|\langle J || e \vec{r} || J' \rangle|^2 = |\langle J' || e \vec{r} || J \rangle|^2$ in the above equations but J' in Eqn. A.23 should be that of the higher energy state.

According to Eqn. A.23, evaluation of the AC-Stark shift requires the knowledge of the radiative lifetimes (or the oscillator strengths) of all allowed dipole transitions to the $|F\rangle$ state. Since the relevant oscillator strengths are fully available for the $5S_{1/2}$ ground state, and not for the $5P_{3/2}$ state of Rb atom [159, 160], the AC Stark shift for the ground states can be determined more accurately than that of the excited states. To obtain the AC-Stark shift of the $5P_{3/2}$ states as shown in Fig. 4.6, we have made use of the known radiative lifetime of the $5P_{3/2}$ to the $5S_{1/2}$ state (26 ns), and assumed that the radiative lifetimes from other higher energy states to the $5P_{3/2}$ state are 10 to 100 times longer than that of the $5P_{3/2}$ to the $5S_{1/2}$ transition. Varying the radiative lifetimes does not change the overall energy structure presented in Fig. 4.6 significantly but it does affect the accuracy of the prediction.

Note, we later found a more complete database that provides most of the significant oscillator strengths for the $5P_{3/2}$ state [161]. However, the results obtained using the oscillator strengths provided therein and Eqn. A.19 were not able to explain our measured resonance frequencies. More explicitly, the ratio of the resonance shifts for the σ^+ to σ^- probe was measured to be $1.56 \pm$

0.05 (see Fig. 4.6), whereas the oscillator strengths given in database [161] predict a ratio of 1.82⁴.

Of course, the discrepancy between the measured resonance shifts and the predictions can possibly be caused by the inaccuracy of the second order perturbation theory since the calculated perturbation can be as large as half of the $5P_{3/2}$ hyperfine splittings for our experimental parameters. In any case, our current setup could provide an alternative for measuring the oscillator strengths of the ^{87}Rb atom (see Appendix A.6).

⁴We have chosen to compare the ratio of the resonance shifts here because we did not measure the dipole trap depth in our setup. Based on the estimation obtained using the waist and optical power of the dipole beam measured outside the vacuum chamber, we expect the dipole trap depth to be around 1 mK to 1.3 mK. The ratio of the resonance shifts is independent of the trap depth according to Eqn. A.19.

A.6 Measuring the oscillator strengths of the Rubidium atom

Our setup has the potential to allow measurement of the unknown oscillator strengths of the atom. First, we note that the AC Stark shift of a particular energy state is mostly determined by the oscillator strengths of a few dipole-allowed transitions. These transitions either have larger oscillator strengths or transition wavelengths close to that of the external field (Eqn. A.19). In principle, if we want to measure N unknown oscillator strengths connected to the $5P_{3/2}$ state, we can repeat our absorption measurements N times using FORT light of different wavelengths. However, practically speaking, one needs to be able to determine the intensity of the light field at the location of the atom accurately. This is only possible if one has full knowledge of the field distribution in the FORT and a very well calibrated power meter. For a tightly focused FORT as in our experiment, determining the field distribution in the FORT can be challenging. Fortunately, this problem can be circumvented by measuring the resonant frequency shifts of two or more different transitions in the atom, since the **ratio** of the resonant-frequency shifts is independent of the intensity.

A detailed proposal for measuring the oscillator strengths of the ^{87}Rb atom using our current setup is as follows:

1. Measure the resonant-frequency shifts of the $|g+\rangle$ to $|e+\rangle$ transition (Δf_+), and of the $|g-\rangle$ to $|e-\rangle$ transition (Δf_-) for a FORT wavelength. The ratio $r = \Delta f_+ / \Delta f_-$ depends only on the known oscillator strengths related to the $5S$ state, and some unknown oscillator strengths related to the $5P_{3/2}$ states (Eqn. A.19).
2. Repeat the previous step N times using FORT of various wavelengths to get N ratios. Solving the N ratio equations gives the N unknown oscillator strengths. Ideally, the more ratios r are measured, the more accurately one can determine the oscillator strengths.

This proposal assumes that the AC-Stark shift of the atom can be predicted by time-dependent perturbation theory to the second order (Eqn. A.19).

If the AC-Stark shifts are comparable to the hyperfine splittings of the atom, Eqn. A.19 may break down and more sophisticated calculations would be required to correctly predict the energy shifts. In any case, the principal idea on how to measure oscillation strengths with our current setup should still work.

A.7 Effects of atomic motion on the scattering probability

The theoretical scattering probabilities shown in Fig. 3.6 and Fig. 4.9 were obtained by assuming that the atom is stationary at the location where the probe field is strongest. In the experiment, however, the atom has a finite temperature and oscillates in the FORT. As the atom wobbles around in the FORT, it experiences a varying probe intensity. Since the scattering probability is proportional to the intensity of the probe seen by the atom, the effective scattering probability should be averaged over the motion of the trapped atom. Nevertheless, tracking the motion of the atom in the FORT is non-trivial for an asymmetrical FORT. Figure A.6 shows the potential of the FORT, and the ‘inverted’ normalized probe intensity in the focal plane (left) and along the lens axis (right). The probe intensity distributions shown in this figure are computed using Eqn. 3.34 for the tightest probe focus used in our experiment ($w_L = 1.4$ mm), whereas the FORT potential is calculated using the paraxial approximation for a focal waist of $1.4 \mu\text{m}$.

To estimate the effective scattering probability, we need to know the temperature of the atom in the FORT. However, we have not yet measured the temperature of the trapped atom. We would assume that the temperature of the atom is about $100 \mu\text{K}$, guided by the measurements of similar setups in other groups [129, 147]. For such temperatures, the atom oscillates near the bottom of the FORT potential, a region where the FORT and probe intensity distributions can be well described by parabolic functions, both along the lens axis and along the radial direction (Fig. A.6).

For simplicity, we now consider the atom as a one-dimensional harmonic oscillator. We would start by considering a scenario where an atom of mass m is oscillating in a harmonic potential described by $U(x) = kx^2/2$, with an oscillation amplitude A and an oscillation frequency $\omega_F = \sqrt{k/m}$. We further express the normalized probe intensity as $I_p(x) = 1 - bx^2$. The average normalized probe intensity I_A experienced by the atom, weighted by the time

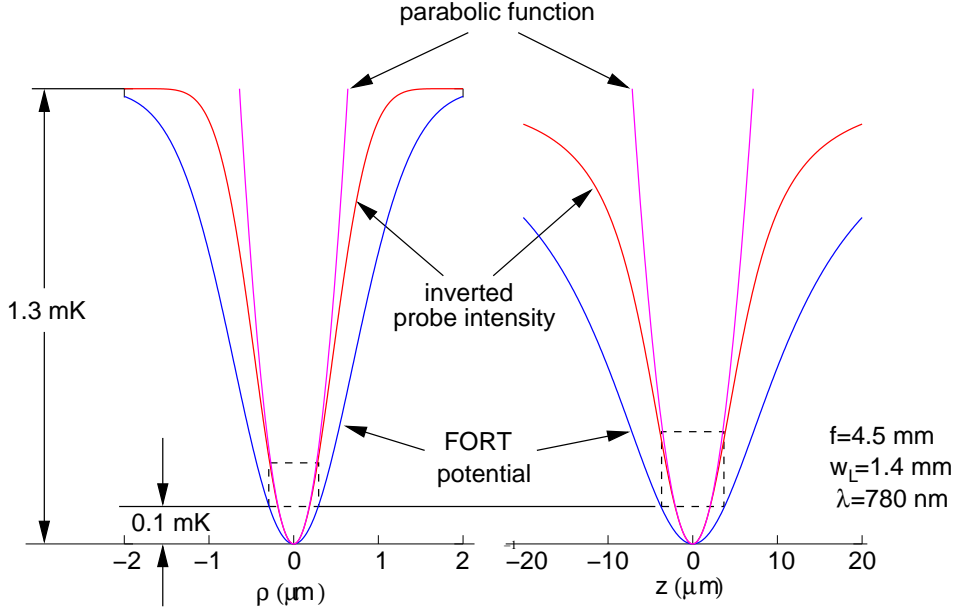


Figure A.6: Potential of the FORT, and the ‘inverted’ normalized probe intensity in the focal plane (left) and along the lens axis (right), computed for the probe parameters stated. The depth of the FORT potential is about $k_B \cdot 1.3$ mK. The temperature of the atom in the FORT is assumed to be around 0.1 mK.

the atom spends in different positions, is given by

$$I_A = \frac{\omega_F}{\pi} \int_{-A}^A dx \frac{I_p(x)}{v} = \int_{-A}^A dx \frac{1 - bx^2}{A\pi\sqrt{1 - (x/A)^2}} = 1 - bA^2/2, \quad (\text{A.24})$$

where $v = dx/dt$ is the velocity. The amplitude A is related to the maximum speed of the atom v' in the harmonic potential by $v' = \omega_F A$. This leads to

$$I_A(v') = 1 - bv'^2/2\omega_F^2. \quad (\text{A.25})$$

Equation A.25 shows the average (normalized) probe intensity experienced by the atom with a total energy of $mv'^2/2$. On the other hand, atoms with a temperature T have a speed distribution governed by the Maxwell-

Boltzmann law ⁵. Therefore, the effective scattering probability is given by ⁶

$$\begin{aligned} p_{\text{sc}}^{\text{eff}} &= p_{\text{sc}} \left[\left(\frac{2}{\pi} \right)^{1/2} \left(\frac{m}{k_B T} \right)^{3/2} \int_0^\infty dv' I_A v'^2 \exp \left(-\frac{mv'^2}{2k_B T} \right) \right] \\ &= p_{\text{sc}} \left(1 - \frac{3bk_B T}{2k} \right). \end{aligned} \quad (\text{A.27})$$

For a FORT depth of $k_B \cdot 1.3$ mK and a FORT beam waist of $w_D = 1.4 \mu\text{m}$, the ‘spring’ constants k are $k_z = 9 \times 10^{-16}$ N/m along the longitudinal direction and $k_\rho = 3.65 \times 10^{-14}$ N/m along the radial direction (Section 4.2 (FORT)). The coefficients for the parabolic functions describing the probe intensity distribution are $b_z = 0.078 \mu\text{m}^{-2}$ and $b_\rho = 2.44 \mu\text{m}^{-2}$, obtained by fitting the probe intensity distribution shown in Fig. A.6. By assuming a temperature of $100 \mu\text{K}$ for the atom in the FORT, we obtain effective scattering probabilities $p_{\text{sc}}^{\text{eff}(z)} = 0.82p_{\text{sc}}$ and $p_{\text{sc}}^{\text{eff}(\rho)} = 0.86p_{\text{sc}}$ for an atom oscillating along the longitudinal and the radial direction respectively.

As a result, we conclude that the reduction of the scattering probability caused by the motion of the atom in the FORT is estimated to be less than 20% for the strongest focusing of the probe beam in our experiment.

⁵The motion of the atom in the FORT is governed by classical mechanics because the average kinetic energy of the atom is much higher than $\hbar\omega_F$ in our case.

⁶Although we consider a 1D-oscillator when deriving Eqn. A.25, we now use a speed distribution for a free atom moving in a three-dimensional space. Should we insist that the atom is only moving in a one-dimensional space, Eqn. A.27 becomes

$$p_{\text{sc}}^{\text{eff}} = p_{\text{sc}}(1 - bk_B T/2k). \quad (\text{A.26})$$

A.8 Setup photos



Figure A.7: Photos of the single atom trap setup.

A.9 Band gaps of various semiconductors

Table A.1: List of band gaps of some semiconductors [48, 162]. The symbols D and I refer to direct or indirect band gap respectively. Quantum dots fabricated using semiconductor with the symbol † have lowest energy transitions falling conveniently within the visible optical regime.

Material	Symbol	Band gap (eV)@300 K	D/I
Silicon	Si	1.11	I
Germanium	Ge	0.67	I
Silicon carbide	SiC	2.86	I
Aluminum phosphide	AlP	2.45	I
Aluminium arsenide	AlAs	2.16	I
Aluminium antimonide	AlSb	1.6	I
Aluminium nitride	AlN	6.3	D
Diamond	C	5.5	I
Gallium(III) phosphide	GaP	2.26	I
Gallium(III) arsenide	GaAs	1.43 [†]	D
Gallium(III) nitride	GaN	3.4	D
Gallium(II) sulfide	GaS	2.5	D
Gallium antimonide	GaSb	0.7	D
Indium(III) phosphide	InP	1.35 [†]	D
Indium(III) arsenide	InAs	0.36	D
Indium antimonide	InSb	0.17	D
Zinc sulfide	ZnS	3.6	D
Zinc selenide	ZnSe	2.7	D
Zinc telluride	ZnTe	2.25	D
Cadmium sulfide	CdS	2.42	D
Cadmium selenide	CdSe	1.73 [†]	D
Cadmium telluride	CdTe	1.49 [†]	D
Lead(II) sulfide	PbS	0.37	D
Lead(II) selenide	PbSe	0.27	D
Lead(II) telluride	PbTe	0.29	D

A.10 Conservation of energy

The total field can be expressed as the superposition of two fields:

$$\vec{E}_t(\vec{r}) = \vec{E}_{\text{in}}(\vec{r}) + \vec{E}_{\text{sc}}(\vec{r}). \quad (\text{A.28})$$

For a weak on-resonant excitation field, the scattered field \vec{E}_{sc} is given by [95]

$$\vec{E}_{\text{sc}}(\vec{r}) = \frac{3E_A e^{i(kr + \pi/2)}}{2kr} \left[\hat{d}_{21} - (\hat{d}_{21} \cdot \hat{r}) \hat{r} \right], \quad (\text{A.29})$$

where \hat{r} is the unit vector along $\vec{r} = r(\sin \theta \cos \phi, \sin \theta \sin \phi, \cos \theta)$, and $\hat{d}_{21} = \frac{\hat{x} + i\hat{y}}{\sqrt{2}}$ for a circular-polarized field. The $\pi/2$ phase reflects the fact that the dipole moment of the atom lags the field experienced by the atom E_A by a phase of $\pi/2$ at resonance. For clarity of the expressions, we now assume that the atom is at the origin O as opposed to that adopted in Chapter 3. We now adopt an incident field \vec{E}_{in} given by

$$\begin{aligned} \vec{E}_{\text{in}}(\rho, \phi, z = \pm f) &= \frac{E_L}{\sqrt{|\cos \theta|}} \left(\frac{1 \pm \cos \theta}{2} \hat{e}_+ \mp \frac{\sin \theta e^{i\phi}}{\sqrt{2}} \hat{z} + \frac{\pm \cos \theta - 1}{2} e^{2i\phi} \hat{e}_- \right) \\ &\times \exp(-\rho^2/w_L^2) \exp\left[\pm i(k\sqrt{\rho^2 + f^2} - \pi/2)\right], \end{aligned} \quad (\text{A.30})$$

which is basically identical to Eqn. 3.34 except that E_L (defined in Eqn. 3.5) is included, and the Gouy phase of $\pi/2$ is shifted from the focus (Eqn. 3.50) to the field at $|z| = f$ so that the electric field amplitude at the focus $E_A = E_{\text{in}}(O)$ is a real number. Note that, in Eqn. 3.34, $0 < \theta < \pi/2$, whereas here θ is the polar angle from the $+\hat{z}$ -direction.

In order to verify that Eqn. A.28 conserves energy despite the fact that no direct ‘depletion’ of the input field E_{in} has been introduced [113, 114, 115, 111], we consider the energy flux crossing the $z = -f$ plane and compare it to the flux crossing the $z = +f$ plane. The time averaged energy flux across a surface S is given by

$$U_S = \frac{\epsilon_0 c^2}{2} \int_S \Re \left\{ \vec{E} \times \vec{B}^* \right\} \cdot d\vec{A} \quad (\text{A.31})$$

where $d\vec{A}$ is a differential area element of the surface S and $\Re(x)$ denotes the real part of x . Inserting Eqn. A.28 into the above equation yields

$$U_S = \frac{\epsilon_0 c^2}{2} \int_S \Re \left\{ \vec{E}_{\text{in}} \times \vec{B}_{\text{in}}^* + \vec{E}_{\text{sc}} \times \vec{B}_{\text{sc}}^* + \vec{E}_{\text{in}} \times \vec{B}_{\text{sc}}^* + \vec{E}_{\text{sc}} \times \vec{B}_{\text{in}}^* \right\} \cdot d\vec{A}$$

Note that in the far field limit, $\vec{B}_{\text{in(sc)}} = \hat{k}_{\text{in(sc)}} \times \vec{E}_{\text{in(sc)}}/c$, where $\hat{k}_{\text{in(sc)}}$ is a dimensionless unit vector parallel to the local field propagation direction, and c the speed of light. Furthermore, before the focus we have $\hat{k}_{\text{sc}} = -\hat{k}_{\text{in}}$, whilst after the focus we have $\hat{k}_{\text{sc}} = \hat{k}_{\text{in}}$. With these field properties, we arrive at

$$U_{z=\pm f} = \frac{\epsilon_0 c}{2} \int_{z=\pm f} \hat{k}_{\text{in}} \cdot \hat{z} \times \Re \left\{ \vec{E}_{\text{in}} \cdot \vec{E}_{\text{in}}^* \pm \vec{E}_{\text{sc}} \cdot \vec{E}_{\text{sc}}^* + \vec{E}_{\text{sc}} \cdot \vec{E}_{\text{in}}^* \pm \vec{E}_{\text{in}} \cdot \vec{E}_{\text{sc}}^* \right\} dA, \quad (\text{A.32})$$

where we have also used the condition that the light fields are transverse, i.e. $\hat{k}_{\text{in}} \cdot \vec{E}_{\text{in}} = 0$ and $\hat{k}_{\text{in}} \cdot \vec{E}_{\text{sc}} = 0$.

Using Eqn. A.30, the first term in Eqn. A.32 gives

$$U_{z=\pm f, \text{in}} \equiv \frac{\epsilon_0 c}{2} \int_{z=\pm f} \Re \left\{ \vec{E}_{\text{in}} \cdot \vec{E}_{\text{in}}^* \right\} \hat{k}_{\text{in}} \cdot \hat{z} dA \quad (\text{A.33})$$

$$= \frac{1}{4} \epsilon_0 \pi c E_L^2 w_L^2 = P_{\text{in}}, \quad (\text{A.34})$$

which agrees with Eqn. 3.6. Using Eqn. A.29, the second term in Eqn. A.32 gives

$$U_{z=\pm f, \text{sc}} \equiv \frac{\epsilon_0 c}{2} \int_{z=\pm f} \Re \left\{ \vec{E}_{\text{sc}} \cdot \vec{E}_{\text{sc}}^* \right\} \hat{k}_{\text{in}} \cdot \hat{z} dA \quad (\text{A.35})$$

$$= \frac{3\epsilon_0 c \lambda^2 E_A^2}{8\pi} = \frac{P_{\text{sc}}}{2}, \quad (\text{A.36})$$

where P_{sc} is defined previously in Eqn. 3.9. On the plane $z = -f$, the last two terms in Eqn. A.32 has no contribution to the integration since $(\vec{E}_{\text{sc}} \cdot \vec{E}_{\text{in}}^* - \vec{E}_{\text{in}} \cdot \vec{E}_{\text{sc}}^*)$ is an imaginary number. On the plane $z = +f$, the

last two terms in Eqn. A.32 give

$$U_{z=+f, \text{int}} \equiv \frac{\epsilon_0 c}{2} \int_{z=\pm f} \Re \left\{ \vec{E}_{\text{sc}} \cdot \vec{E}_{\text{in}}^* + \vec{E}_{\text{in}} \cdot \vec{E}_{\text{sc}}^* \right\} \hat{k}_{\text{in}} \cdot \hat{z} dA \quad (\text{A.37})$$

$$= -\frac{3\pi\epsilon_0 c E_A E_L \sqrt{f}}{2k} \int_0^\infty \frac{\rho(f + \sqrt{f^2 + \rho^2})}{(f^2 + \rho^2)^{5/4}} \exp\left(-\frac{\rho^2}{w_L^2}\right) d\rho. \quad (\text{A.38})$$

The negative sign, which comes from both the Gouy phase in the incident field (Eqn. A.30) and the phase difference between the dipole and local field (Eqn. A.29), reveals that the scattered light and the incident light interfere destructively after the focus [111]. This integral is of the same form as that of Eqn. 3.49 and can be evaluated in the same way as Eqn. 3.50, leading to

$$U_{z=+f, \text{int}} = -\frac{3\epsilon_0 c \lambda^2 E_A^2}{4\pi} = -P_{\text{sc}}. \quad (\text{A.39})$$

As a result of Equations (A.34), (A.36), and (A.39), the total energy flux flowing across the $z = -f$ and $z = +f$ surfaces are both

$$U_{z=\pm f} = P_{\text{in}} - \frac{P_{\text{sc}}}{2}. \quad (\text{A.40})$$

This confirms that no extra energy is generated by directly adding the the scattered field to the unattenuated incident field (Eqn. A.28), even when the scattering probability is great than 1. Note that at the limit, $P_{\text{sc}} = 2P_{\text{in}}$, $U_{z=\pm f} = 0$. This means that all incident power is reflected back by the two-level system [111].

Bibliography

- [1] van Enk, S. J. & Kimble, H. J. Strongly focused light beams interacting with single atoms in free space. *Physical Review A: Atomic, Molecular, and Optical Physics* **63**, 023809 (2001).
- [2] M. A. Nielsen, I. L. C. *Quantum computation and quantum information* (Cambridge University, 2000).
- [3] Quantum information science—report of the nsf workshop, october 28-29, 1999 (1999). URL <http://www.nsf.gov/pubs/2000/nsf00101/nsf00101.htm>.
- [4] Cirac, J. I., Duan, L. M. & Zoller, P. Quantum optical implementation of quantum information processing (2004). URL <http://www.citebase.org/abstract?id=oai:arXiv.org:quant-ph/0405030>.
- [5] Zoller, P., Cirac, J. I., Duan, L. & Garcia-Ripoll, J. J. Implementing quantum information processing with atoms, ions and photons (2004). URL <http://www.citebase.org/abstract?id=oai:arXiv.org:quant-ph/0405025>.
- [6] Shor, P. W. Polynomial-time algorithms for prime factorization and discrete logarithms on a quantum computer. *SIAM Journal on Computing* **26**, 1484–1509 (1997).
- [7] Cirac, J. I. & Zoller, P. Quantum computations with cold trapped ions. *Phys. Rev. Lett.* **74**, 4091–4094 (1995).
- [8] Monroe, C., Meekhof, D. M., King, B. E., Itano, W. M. & Wineland, D. J. Demonstration of a fundamental quantum logic gate. *Phys. Rev. Lett.* **75**, 4714–4717 (1995).
- [9] Brennen, G. K., Caves, C. M., Jessen, P. S. & Deutsch, I. H. Quantum logic gates in optical lattices. *Phys. Rev. Lett.* **82**, 1060–1063 (1999).

- [10] Knill, E., Laflamme, R. & Milburn, G. J. A scheme for efficient quantum computation with linear optics. *Nature* **409**, 46–52 (2001).
- [11] O’Brien, J. L., Pryde, G. J., White, A. G., Ralph, T. C. & Branning, D. Demonstration of an all-optical quantum controlled-not gate. *Nature* **426**, 264–267 (2003).
- [12] Turchette, Q. A., Hood, C. J., Lange, W., Mabuchi, H. & Kimble, H. J. Measurement of conditional phase shifts for quantum logic. *Phys. Rev. Lett.* **75**, 4710–4713 (1995).
- [13] Clarke, J. & Wilhelm, F. K. Superconducting quantum bits. *Nature* **453**, 1031–1042 (2008).
- [14] Neumann, P. *et al.* Multipartite Entanglement Among Single Spins in Diamond. *Science* **320**, 1326–1329 (2008).
- [15] Loss, D. & DiVincenzo, D. P. Quantum computation with quantum dots. *Phys. Rev. A* **57**, 120–126 (1998).
- [16] Li, X. *et al.* An All-Optical Quantum Gate in a Semiconductor Quantum Dot. *Science* **301**, 809–811 (2003).
- [17] DiVincenzo, D. P. The physical implementation of quantum computation. *Fortschritte der Physik* **48**, 771–783 (2000).
- [18] Cirac, J. I., Zoller, P., Kimble, H. J. & Mabuchi, H. Quantum state transfer and entanglement distribution among distant nodes in a quantum network. *Physical Review Letters* **78**, 3221–3224 (1997).
- [19] Duan, L. M., Lukin, M. D., Cirac, J. I. & Zoller, P. Long-distance quantum communication with atomic ensembles and linear optics. *Nature* **414**, 413–418 (2001).
- [20] Kimble, H. J. The quantum internet. *Nature* **453**, 1023–1030 (2008).
- [21] Wootters, W. K. & Zurek, W. H. A single quantum cannot be cloned. *Nature* **299**, 802–803 (1982).
- [22] Meschede, D., Walther, H. & Müller, G. One-atom maser. *Physical Review Letters* **54**, 551–554 (1985).
- [23] Pinkse, P. W. H., Fischer, T., Maunz, P. & Rempe, G. Trapping an atom with single photons. *Nature* **404**, 365–368 (2000). 10.1038/35006006.

- [24] Boozer, A. D., Boca, A., Miller, R., Northup, T. E. & Kimble, H. J. Reversible state transfer between light and a single trapped atom. *Physical Review Letters* **98**, 193601 (2007).
- [25] Gleyzes, S. *et al.* Quantum jumps of light recording the birth and death of a photon in a cavity. *Nature* **446**, 297–300 (2007). 10.1038/nature05589.
- [26] Tey, M. K. *et al.* Interfacing light and single atoms with a lens (2008). URL <http://www.citebase.org/abstract?id=oai:arXiv.org:0804.4861>.
- [27] Tey, M. K. *et al.* Strong interaction between light and a single trapped atom without a cavity (2008). URL <http://www.citebase.org/abstract?id=oai:arXiv.org:0802.3005>.
- [28] Chuang, I. L., Gershenfeld, N. & Kubinec, M. Experimental implementation of fast quantum searching. *Phys. Rev. Lett.* **80**, 3408–3411 (1998).
- [29] Plantenberg, J. H., de Groot, P. C., Harmans, C. J. P. M. & Mooij, J. E. Demonstration of controlled-not quantum gates on a pair of superconducting quantum bits. *Nature* **447**, 836–839 (2007).
- [30] Murray, C. B., Norris, D. J. & Bawendi, M. G. Synthesis and characterization of nearly monodisperse cde (e = sulfur, selenium, tellurium) semiconductor nanocrystallites. *Journal of the American Chemical Society* **115**, 8706–8715 (1993).
- [31] Hines, M. & Guyot-Sionnest, P. Synthesis and characterization of strongly luminescing zns-capped cdse nanocrystals. *Journal of Physical Chemistry* **100**, 468–471 (1996).
- [32] Peng, X., Schlamp, M., Kadavanich, A. & Alivisatos, A. Epitaxial growth of highly luminescent cdse/cds core/shell nanocrystals with photostability and electronic accessibility. *Journal of the American Chemical Society* **119**, 7019–7029 (1997).
- [33] Manna, L., Scher, E. & Alivisatos, A. Synthesis of soluble and processable rod-, arrow-, teardrop-, and tetrapod-shaped cdse nanocrystals. *Journal of the American Chemical Society* **122**, 12700–12706 (2000).
- [34] Qu, L. & Peng, X. Control of photoluminescence properties of cdse nanocrystals in growth. *Journal of the American Chemical Society* **124**, 2049–2055 (2002).

- [35] Dabbousi, B. *et al.* (cdse)zns core-shell quantum dots: Synthesis and characterization of a size series of highly luminescent nanocrystallites. *Journal of Physical Chemistry B* **101**, 9463–9475 (1997).
- [36] Spanhel, L., Haase, M., Weller, H. & Henglein, A. Photochemistry of colloidal semiconductors. 20. surface modification and stability of strong luminescing cds particles. *Journal of the American Chemical Society* **109**, 5649–5655 (1987).
- [37] Kortan, A. R. *et al.* Nucleation and growth of cadmium selenide on zinc sulfide quantum crystallite seeds, and vice versa, in inverse micelle media. *Journal of the American Chemical Society* **112**, 1327–1332 (1990).
- [38] Duggan, G. & Ralph, H. I. Exciton binding energy in type-ii gaas-(al,ga)as quantum-well heterostructures. *Phys. Rev. B* **35**, 4152–4154 (1987).
- [39] Branis, S. V. & Bajaj, K. K. Calculation of the exciton binding energies in type-ii gaas/alas quantum-well structures: Application of the perturbation-variational expansion method. *Phys. Rev. B* **45**, 6271–6274 (1992).
- [40] Laheld, U. E. H., Pedersen, F. B. & Hemmer, P. C. Excitons in type-ii quantum dots: Finite offsets. *Phys. Rev. B* **52**, 2697–2703 (1995).
- [41] Zheng, Y., Gau, S. & Ying, J. Synthesis and cell-imaging applications of glutathione-capped cdte quantum dots. *Advanced Materials* **19**, 376–380 (2007).
- [42] D.J. Norris, L. B., M.G. Bawendi. *Molecular Electronics: A 'Chemistry for 21st Century' Monograph* (Blackwell Science, Cambridge, Mass, 1997).
- [43] Klimov, V. I. Spectral and dynamical properties of multiexcitons in semiconductor nanocrystals. *Annual Review of Physical Chemistry* **58**, 635–673 (2007).
- [44] Ekimov, A. I. *et al.* Absorption and intensity-dependent photoluminescence measurements on cdse quantum dots: assignment of the first electronic transitions. *J. Opt. Soc. Am. B* **10**, 100 (1993).
- [45] Afros, A. & Efros, A. L. Interband absorption of light in a semiconductor sphere. *Soviet Physics - Semiconductors* **16**, 772–775 (1982).

- [46] Brus, L. E. A simple model for the ionization potential, electron affinity, and aqueous redox potentials of small semiconductor crystallites. *The Journal of Chemical Physics* **79**, 5566–5571 (1983).
- [47] Brus, L. E. Electron–electron and electron-hole interactions in small semiconductor crystallites: The size dependence of the lowest excited electronic state. *The Journal of Chemical Physics* **80**, 4403–4409 (1984).
- [48] Kittel, C. *Introduction to solid state physics* (Wiley, New York, 1986).
- [49] Xia, J.-B. Electronic structures of zero-dimensional quantum wells. *Phys. Rev. B* **40**, 8500–8507 (1989).
- [50] Chepic, D. I. *et al.* Auger ionization of semiconductor quantum drops in a glass matrix. *Journal of Luminescence* **47**, 113–127 (1990).
- [51] Norris, D. J. & Bawendi, M. G. Measurement and assignment of the size-dependent optical spectrum in cdse quantum dots. *Phys. Rev. B* **53**, 16338–16346 (1996).
- [52] Bastard, G. *Wave Mechanics Applied to Semiconductor Heterostructures* (Wiley, New York, 1988).
- [53] Thoai, D. B. T., Hu, Y. Z. & Koch, S. W. Influence of the confinement potential on the electron-hole-pair states in semiconductor microcrystallites. *Phys. Rev. B* **42**, 11261–11266 (1990).
- [54] Luttinger, J. M. & Kohn, W. Motion of electrons and holes in perturbed periodic fields. *Phys. Rev.* **97**, 869–883 (1955).
- [55] Luttinger, J. M. Quantum theory of cyclotron resonance in semiconductors: General theory. *Phys. Rev.* **102**, 1030–1041 (1956).
- [56] G.L. Bir, G. P. *Symmetry and Strain-Induced Effects in Semiconductors* (Wiley, New York, 1974).
- [57] Lipari, N. O. & Baldereschi, A. Angular momentum theory and localized states in solids. investigation of shallow acceptor states in semiconductors. *Phys. Rev. Lett.* **25**, 1660–1664 (1970).
- [58] Baldereschi, A. & Lipari, N. O. Spherical model of shallow acceptor states in semiconductors. *Phys. Rev. B* **8**, 2697–2709 (1973).

- [59] Bawendi, M. G. *et al.* Electronic structure and photoexcited-carrier dynamics in nanometer-size cdse clusters. *Phys. Rev. Lett.* **65**, 1623–1626 (1990).
- [60] Bawendi, M. G., Carroll, P. J., Wilson, W. L. & Brus, L. E. Luminescence properties of cdse quantum crystallites: Resonance between interior and surface localized states. *The Journal of Chemical Physics* **96**, 946–954 (1992).
- [61] Efros, A. L., Kharchenko, V. A. & Rosen, M. Breaking the phonon bottleneck in nanometer quantum dots: Role of auger-like processes. *Solid State Communications* **93**, 301–305 (1995).
- [62] Klimov, V. I. & McBranch, D. W. Femtosecond $1p$ -to- $1s$ electron relaxation in strongly confined semiconductor nanocrystals. *Phys. Rev. Lett.* **80**, 4028–4031 (1998).
- [63] Guyot-Sionnest, P., Shim, M., Matranga, C. & Hines, M. Intraband relaxation in cdse quantum dots. *Phys. Rev. B* **60**, R2181–R2184 (1999).
- [64] Darugar, Q., Landes, C., Link, S., Schill, A. & El-Sayed, M. A. Why is the thermalization of excited electrons in semiconductor nanoparticles so rapid?: Studies on cdse nanoparticles. *Chemical Physics Letters* **373**, 284–291 (2003).
- [65] O’Neil, M., Marohn, J. & McLendon, G. Dynamics of electron-hole pair recombination in semiconductor clusters. *Journal of Physical Chemistry* **94**, 4356–4363 (1990).
- [66] Hässelbarth, A., Eychmüller, A. & Weller, H. Detection of shallow electron traps in quantum sized cds by fluorescence quenching experiments. *Chemical Physics Letters* **203**, 271–276 (1993).
- [67] Empedocles, S. A., Norris, D. J. & Bawendi, M. G. Photoluminescence spectroscopy of single cdse nanocrystallite quantum dots. *Phys. Rev. Lett.* **77**, 3873–3876 (1996).
- [68] Empedocles, S. & Bawendi, M. Influence of spectral diffusion on the line shapes of single cdse nanocrystallite quantum dots. *Journal of Physical Chemistry B* **103**, 1826–1830 (1999).
- [69] Nirmal, M. *et al.* Observation of the ”dark exciton” in cdse quantum dots. *Phys. Rev. Lett.* **75**, 3728–3731 (1995).

- [70] Labeau, O., Tamarat, P. & Lounis, B. Temperature dependence of the luminescence lifetime of single *cdse/zns* quantum dots. *Phys. Rev. Lett.* **90**, 257404 (2003).
- [71] Crooker, S. A., Barrick, T., Hollingsworth, J. A. & Klimov, V. I. Multiple temperature regimes of radiative decay in *cdse* nanocrystal quantum dots: Intrinsic limits to the dark-exciton lifetime. *Applied Physics Letters* **82**, 2793–2795 (2003).
- [72] Efros, A. L. *et al.* Band-edge exciton in quantum dots of semiconductors with a degenerate valence band: Dark and bright exciton states. *Phys. Rev. B* **54**, 4843–4856 (1996).
- [73] Norris, D. J., Efros, A. L., Rosen, M. & Bawendi, M. G. Size dependence of exciton fine structure in *cdse* quantum dots. *Phys. Rev. B* **53**, 16347–16354 (1996).
- [74] Kuno, M., Lee, J. K., Dabbousi, B. O., Mikulec, F. V. & Bawendi, M. G. The band edge luminescence of surface modified *cdse* nanocrystallites: Probing the luminescing state. *The Journal of Chemical Physics* **106**, 9869–9882 (1997).
- [75] Klimov, V. I., Mikhailovsky, A. A., McBranch, D. W., Leatherdale, C. A. & Bawendi, M. G. Quantization of Multiparticle Auger Rates in Semiconductor Quantum Dots. *Science* **287**, 1011–1013 (2000).
- [76] Htoon, H., Hollingsworth, J. A., Dickerson, R. & Klimov, V. I. Effect of zero- to one-dimensional transformation on multiparticle auger recombination in semiconductor quantum rods. *Phys. Rev. Lett.* **91**, 227401 (2003).
- [77] Efros, A. L. & Rosen, M. Random telegraph signal in the photoluminescence intensity of a single quantum dot. *Phys. Rev. Lett.* **78**, 1110–1113 (1997).
- [78] van de Hulst, H. C. *Light scattering by small particles* (Dover Publications, New York, 1981), second edn.
- [79] Leatherdale, C., Woo, W.-K., Mikulec, F. & Bawendi, M. On the absorption cross section of *cdse* nanocrystal quantum dots. *Journal of Physical Chemistry B* **106**, 7619–7622 (2002).
- [80] Empedocles, S. A. & Bawendi, M. G. Quantum-confined stark effect in single *cdse* nanocrystallite quantum dots. *Science* **278**, 2114–2117 (1997).

- [81] Kurtsiefer, C., Zarda, P., Mayer, S. & Weinfurter, H. The breakdown flash of silicon avalanche photodiodes—back door for eavesdropper attacks? *Journal of Modern Optics* **48**, 2039–2047 (2001).
- [82] Lounis, B., Bechtel, H. A., Gerion, D., Alivisatos, P. & Moerner, W. E. Photon antibunching in single cdse/zns quantum dot fluorescence. *Chemical Physics Letters* **329**, 399–404 (2000).
- [83] Savage, C. M., Braunstein, S. L. & Walls, D. F. Macroscopic quantum superpositions by means of single-atom dispersion. *Opt. Lett.* **15**, 628 (1990).
- [84] Rosenfeld, W., Berner, S., Volz, J., Weber, M. & Weinfurter, H. Remote preparation of an atomic quantum memory. *Physical Review Letters* **98**, 050504 (2007).
- [85] Sondermann, M. *et al.* Design of a mode converter for efficient light-atom coupling in free space. *Applied Physics B: Lasers and Optics* **89**, 489–492 (2007).
- [86] Diedrich, F. & Walther, H. Nonclassical radiation of a single stored ion. *Physical Review Letters* **58**, 203–206 (1987).
- [87] Lounis, B. & Moerner, W. E. Single photons on demand from a single molecule at room temperature. *Nature* **407**, 491–493 (2000).
- [88] Michler, P. *et al.* Quantum correlation among photons from a single quantum dot at room temperature. *Nature* **406**, 968–970 (2000).
- [89] Santori, C., Pelton, M., Solomon, G., Dale, Y. & Yamamoto, Y. Triggered single photons from a quantum dot. *Phys. Rev. Lett.* **86**, 1502–1505 (2001).
- [90] Kurtsiefer, C., Mayer, S., Zarda, P. & Weinfurter, H. Stable solid-state source of single photons. *Phys. Rev. Lett.* **85**, 290–293 (2000).
- [91] Keller, M., Lange, B., Hayasaka, K., Lange, W. & Walther, H. Continuous generation of single photons with controlled waveform in an ion-trap cavity system. *Nature* **431**, 1075–1078 (2004).
- [92] McKeever, J. *et al.* Deterministic Generation of Single Photons from One Atom Trapped in a Cavity. *Science* **303**, 1992–1994 (2004).
- [93] Hijlkema, M. *et al.* A single-photon server with just one atom. *Nat Phys* **3**, 253–255 (2007).

- [94] Mollow, B. R. Power spectrum of light scattered by two-level systems. *Phys. Rev.* **188**, 1969–1975 (1969).
- [95] C. Cohen-Tannoudji, G. G., J. Dupont-Roc. *Atom-photon interactions: basic processes and application* (Wiley, New York, 1992).
- [96] Weisskopf, V. & Wigner, E. *Z. Phys.* **63**, 54 (1930).
- [97] Knight, P. L. Dynamics of spontaneous emission. *Physica Scripta* **T70**, 94–100 (1997).
- [98] Scully, M. O. & Zubairy, S. *Quantum Optics* (Cambridge University Press, Cambridge, 1997).
- [99] Loudon, R. *The Quantum Theory of Light* (Oxford University Press, Oxford, 1973), third edn.
- [100] Foot, C. J. *Atomic physics* (Oxford University Press, Oxford, 2005).
- [101] C. Cohen-Tannoudji, G. G., J. Dupont-Roc. *Photons and atoms: Introduction to Quantum Electrodynamics* (Wiley, New York, 1989).
- [102] T. A. Nieminen, H. R.-D. & Heckenberg, N. R. Multipole expansion of strongly focussed laser beams. *Journal of Quantitative Spectroscopy and Radiative Transfer* **79**, 1005–1017 (Jul 2002).
- [103] S. J. Van Enk, G. N. Commutation rules and eigenvalues of spin and orbital angular momentum of radiation fields. *Journal of Modern Optics* **41**, 963–977(15) (May 1994).
- [104] Richards, B. & Wolf, E. Electromagnetic diffraction in optical systems II. Structure of the image field in an aplanatic system. *Proceedings of the Royal Society of London - A* **253**, 358–379 (1959).
- [105] S. J. van Enk, G. N. Eigenfunction description of laser beams and orbital angular momentum of light. *Optics Communications* **93**, 147–158 (Nov 1992).
- [106] Beijersbergen, M. W., Allen, L., "van der Veen", H. E. L. O. & Woerdman, J. P. Astigmatic laser mode converters and transfer of orbital angular momentum. *Optics Communications* **96**, 123–132 (Feb 1993).
- [107] Bassett, I. M. Limit to concentration by focusing. *Journal of Modern Optics* **33**, 279–286 (1986).

- [108] Sheppard, C. & Larkin, K. Optimal concentration of electromagnetic radiation. *Journal of Modern Optics* **41**, 1495–1505 (1994).
- [109] Jackson, J. D. *Classical Electrodynamics* (Wiley, New York, 1975), 2nd edn.
- [110] Born, M. & Wolf, E. *Principles of Optics* (Pergamon, New York, 1975).
- [111] Zumofen, G., Mojarad, N. M., Sandoghdar, V. & Agio, M. Perfect reflection of light by an oscillating dipole. *Physical Review Letters* **101**, 180404 (2008).
- [112] van Enk, S. J. Atoms, dipole waves, and strongly focused light beams. *Phys. Rev. A* **69**, 043813 (2004).
- [113] Bohren, C. F. How can a particle absorb more than the light incident on it? *American Journal of Physics* **51**, 323–327 (1983).
- [114] Paul, H. & Fisher, R. Light absorption by a dipole. *Soviet Physics Uspekhi* **26**, 923–926 (1983).
- [115] Davis, R. C. & Williams, C. C. Optical dipole model for photodetection in the near field. *J. Opt. Soc. Am. A* **18**, 1543–1551 (2001).
- [116] Bohren, C. F. & Huffman, D. R. *Absorption and Scattering of Light by Small Particles* (Wiley, New York, 1983).
- [117] Sheppard, C. & Torok, P. Efficient calculation of electromagnetic diffraction in optical systems using multipole expansion. *Journal of Modern Optics* **44**, 803–818 (1997).
- [118] Tamarat, P., Maali, A., Lounis, B. & Orrit, M. Ten years of single molecule spectroscopy. *The Journal of Physical Chemistry A* **104**, 1–16 (2000).
- [119] Wineland, D. J., Itano, W. M. & Bergquist, J. C. Absorption spectroscopy at the limit: detection of a single atom. *Opt. Lett.* **12**, 389 (1987).
- [120] Moerner, W. E. & Kador, L. Optical detection and spectroscopy of single molecules in a solid. *Phys. Rev. Lett.* **62**, 2535–2538 (1989).
- [121] L. Kador, D. E. H. & Moerner, W. E. Optical detection and probing of single dopant molecules of pentacene in a p-terphenyl host crystal by means of absorption spectroscopy. *Journal of Physical Chemistry* **94**, 1237–1248 (1990).

- [122] Stievater, T. H. *et al.* Wavelength modulation spectroscopy of single quantum dots. *Applied Physics Letters* **80**, 1876–1878 (2002).
- [123] Alen, B., Bickel, F., Karrai, K., Warburton, R. J. & Petroff, P. M. Stark-shift modulation absorption spectroscopy of single quantum dots. *Applied Physics Letters* **83**, 2235–2237 (2003).
- [124] Guest, J. R. *et al.* Measurement of optical absorption by a single quantum dot exciton. *Phys. Rev. B* **65**, 241310 (2002).
- [125] Gerhardt, I. *et al.* Strong extinction of a laser beam by a single molecule. *Physical Review Letters* **98**, 033601 (2007).
- [126] Wrigge, G., Gerhardt, I., Hwang, J., Zumofen, G. & Sandoghdar, V. Efficient coupling of photons to a single molecule and the observation of its resonance fluorescence (2007).
- [127] Vamivakas, A. *et al.* Strong extinction of a far-field laser beam by a single quantum dot. *Nano Letters* **7**, 2892–2896 (2007).
- [128] Schlosser, N., Reymond, G., Protsenko, I. & Grangier, P. Subpoissonian loading of single atoms in a microscopic dipole trap. *Nature* **411**, 1024–1027 (2001). 10.1038/35082512.
- [129] Weber, M., Volz, J., Saucke, K., Kurtsiefer, C. & Weinfurter, H. Analysis of a single-atom dipole trap. *Physical Review A (Atomic, Molecular, and Optical Physics)* **73**, 043406 (2006).
- [130] Chu, S., Hollberg, L., Bjorkholm, J. E., Cable, A. & Ashkin, A. Three-dimensional viscous confinement and cooling of atoms by resonance radiation pressure. *Phys. Rev. Lett.* **55**, 48–51 (1985).
- [131] Chu, S., Bjorkholm, J. E., Ashkin, A. & Cable, A. Experimental observation of optically trapped atoms. *Phys. Rev. Lett.* **57**, 314–317 (1986).
- [132] Raab, E. L., Prentiss, M., Cable, A., Chu, S. & Pritchard, D. E. Trapping of neutral sodium atoms with radiation pressure. *Phys. Rev. Lett.* **59**, 2631–2634 (1987).
- [133] Wineland, D. J. & Itano, W. M. Laser cooling of atoms. *Phys. Rev. A* **20**, 1521–1540 (1979).
- [134] Lett, P. D. *et al.* Observation of atoms laser cooled below the doppler limit. *Phys. Rev. Lett.* **61**, 169–172 (1988).

- [135] Aspect, A., Arimondo, E., Kaiser, R., Vansteenkiste, N. & Tannoudji, C. C. Laser cooling below the one-photon recoil energy by velocity-selective coherent population trapping. *Phys. Rev. Lett* **61** (1988).
- [136] Dalibard, J. & Cohen-Tannoudji, C. Laser cooling below the doppler limit by polarization gradients: simple theoretical models. *J. Opt. Soc. Am. B* **6**, 2023+ (1989).
- [137] Adams, C. S. & Riis, E. Laser cooling and trapping of neutral atoms. *Progress in Quantum Electronics* **21**, 1–79 (1997).
- [138] De Labachellerie, M. & Cerez, P. An 850 nm semiconductor laser tunable over a 300 a range. *Optics Communications* **55**, 174–178 (1985).
- [139] Wieman, C. E. & Hollberg, L. Using diode lasers for atomic physics. *Review of Scientific Instruments* **62**, 1–20 (1991).
- [140] Arnold, A. S., Wilson, J. S. & Boshier, M. G. A simple extended-cavity diode laser. *Rev. Sci. Instrum.* **69**, 1236–1239 (1998).
- [141] Andalkar, A., Lamoreaux, S. K. & Warrington, R. B. Improved external cavity design for cesium d1 (894 nm) diode laser. *Review of Scientific Instruments* **71**, 4029–4031 (2000).
- [142] Bjorklund, G. C., Levenson, M. D., Lenth, W. & Ortiz, C. Frequency modulation (fm) spectroscopy. *Applied Physics B: Lasers and Optics* **32**, 145–152 (1983).
- [143] Supplee, J. M., Whittaker, E. A. & Lenth, W. Theoretical description of frequency modulation and wavelength modulation spectroscopy. *Appl. Opt.* **33**, 6294 (1994).
- [144] Donley, E. A., Heavner, T. P., Levi, F., Tataw, M. O. & Jefferts, S. R. Double-pass acousto-optic modulator system. *Review of Scientific Instruments* **76**, 063112 (2005).
- [145] Grimm, R., Weidemuller, M. & Ovchinnikov, Y. B. Optical dipole traps for neutral atoms. *MOLECULAR AND OPTICAL PHYSICS* **42**, 95 (2000).
- [146] Kuppens, S. J. M., Corwin, K. L., Miller, K. W., Chupp, T. E. & Wieman, C. E. Loading an optical dipole trap. *Phys. Rev. A* **62**, 013406 (2000).

- [147] Sortais, Y. R. P. *et al.* Diffraction-limited optics for single-atom manipulation. *Physical Review A (Atomic, Molecular, and Optical Physics)* **75**, 013406 (2007).
- [148] Schlosser, N., Reymond, G. & Grangier, P. Collisional blockade in microscopic optical dipole traps. *Phys. Rev. Lett.* **89**, 023005 (2002).
- [149] Ueberholz, B., Kuhr, S., Frese, D., Meschede, D. & Gomer, V. Counting cold collisions. *Journal of Physics B: Atomic, Molecular and Optical Physics* **33**, L135–L142 (2000).
- [150] Gomer, V. *et al.* Decoding the dynamics of a single trapped atom from photon correlations. *Applied Physics B: Lasers and Optics* **67**, 689–697 (1998). 10.1007/s003400050567.
- [151] Frese, D. *et al.* Single atoms in an optical dipole trap: Towards a deterministic source of cold atoms. *Phys. Rev. Lett.* **85**, 3777–3780 (2000).
- [152] Titulaer, U. M. & Glauber, R. J. Correlation functions for coherent fields. *Phys. Rev.* **140**, B676–B682 (1965).
- [153] Glauber, R. J. The quantum theory of optical coherence. *Phys. Rev.* **130**, 2529–2539 (1963).
- [154] Glauber, R. J. Coherent and incoherent states of the radiation field. *Phys. Rev.* **131**, 2766–2788 (1963).
- [155] Alicki, R. Quantum decay cannot be completely reversed. the 5% rule (2008). URL <http://www.citebase.org/abstract?id=oai:arXiv.org:0807.2609>.
- [156] Piessens, R., de Doncker-Kapenger, E., Ueberhuber, C. & Kahaner, D. *Quadpack: A subroutine package for automatic integration* (Springer, Verlag, 1983).
- [157] Sakurai, J. J. *Modern Quantum Mechanics* (Addison-Wesley, 1994), revised edn.
- [158] Steck, D. Rubidium 87 d line data. URL <http://steck.us/alkalidata>. Accessed on Nov 2007.
- [159] NIST. National institute of standards and technology physical reference data. URL <http://physics.nist.gov/PhysRefData/ASD/index.html>. Accessed on Jun 2007.

- [160] Arora, B., Safronova, M. S. & Clark, C. W. Accurate determination of electric-dipole matrix elements in k and rb from stark shift measurements (2007). URL <http://www.citebase.org/abstract?id=oai:arXiv.org:0709.0014>.
- [161] Smith, P. L., Heise, C., Esmond, J. R. & Kurucz, R. L. Amp tools: Databases: Kurucz atomic line database. URL <http://www.cfa.harvard.edu/amp/ampdata/kurucz23/sekur.html>. Accessed on Mar 2009.
- [162] Ben G. Streetman, S. B. *Solid State Electronic Devices* (Prentice Hall, New Jersey, 2000), 5th edn.